Doctoral dissertation

Material Design and Engineering of Zn–air Batteries

Joohyuk Park

Department of Energy Engineering

(Battery Science and Technology)

Graduate School of UNIST

2017

Material Design and Engineering of Zn–air Batteries

Joohyuk Park

Department of Energy Engineering

(Battery Science and Technology)

Graduate School of UNIST

2017

Material Design and Engineering of Zn–air Batteries

Joohyuk Park

Department of Energy Engineering

(Battery Science and Technology)

Graduate School of UNIST

Material Design and Engineering of Zn–air Batteries

A dissertation
submitted to the Graduate School of UNIST
in partial fulfillment of the requirements
for the degree of Doctor of Philosophy in Energy Engineering

Joohyuk Park

06. 09. 2017
Approved by

조 재필

Advisor
Jaephil Cho

Material Design and Engineering of Zn–air Batteries

Joohyuk Park

This certifies that the dissertation of Joohyuk Park is approved.

06. 09. 2017

Advisor: Jaephil Cho

Youngsik Kim

Sung You Hong

Seok Ju Kang

Hyun-Wook Lee

Abstract

The growing environmental deterioration and rapid depletion of fossil fuels, such as coal, oil and natural gas, have led to urgent needs of the electrochemical energy devices. With demands for alternatives to petroleum fuels, the energy conversion and storage system have been developed. Among them, Zn–air batteries are receiving intense interest as the most promising electrical energy storage (EES) systems because of its high specific energy density (ca. 1,084 Wh kg^{-1}), high safety with aqueous electrolytes and low cost of zinc metal anode. However, there are limitations arising from the slow kinetics of oxygen reduction reaction (ORR) and oxygen evolution reaction (OER). To date, pyrochlore oxides ($A_2[B_{2-x}A_x]O_{7-y}$) have been intensively studied as bi-functional oxygen electrocatalysts among a variety of metal oxides for achieving both high ORR and OER activities. However, the origin of outstanding catalytic activities and structural stabilities of pyrochlore oxides in aqueous Zn–air batteries are not clearly revealed, in part due to the difficulty in identification during electrocatalysis. Herein, we present the highly pure single crystalline pyrochlore nanoparticles including lead ruthenate ($Pb_2Ru_2O_{6.5}$) and yttrium ruthenate ($Y_2[Ru_{2-x}Y_x]O_{7-y}$) as efficient electrocatalysts for rechargeable Zn–air batteries.

In addition, recent developments in the field of wearable and portable electronic devices have received the spotlight for practical applications such as smart electronics and flexible devices. With demands for flexible design of Zn–air batteries, we first developed the cable-type flexible Zn–air batteries with high electrochemical performance. In order to achieve the flexible system, we fabricated a freestanding gelatin based gel polymer electrolyte based upon 0.1 M KOH, showing highly improved ionic conductivity. Notably, the cable-type Zn–air batteries are fabricated for outstanding flexible and bendable properties with highly stable operating potential, of which value is identical to that of non-bending condition.

Contents

List of Figures

Figure 15. (a) Chronoamperometric response of Fe/N/C-900 and 20 % Pt/C in O_2-saturated 0.1 M KOH solution at −0.2 V (vs. Hg/HgO) at 1600 rpm each.

Figure 16. Tafel plots of log I_k (A) vs. E (V) for the ORR on Fe/N/Cs electrodes in an O_2-saturated 0.1 M KOH solution at a rotation rate of 1600 rpm. Limiting current density obtained at potential −0.5 V vs. Hg/HgO was used to calculate I_k using the equations, $i_k = i_L \cdot i/(i_L - i)$.

Figure 17. (a) Digital photograph of freestanding 0.1M KOH-based GGPE. (b) AC impedance spectra of the GGPE in the frequency ranged from 10 kHz to 0.01 Hz. (c) AC impedance spectra of stack-type ZAB based on GGPE in the frequency ranged from 10 kHz to 0.01 Hz. (d) Discharge curves of stack-type ZAB with the GGPE electrolyte at various current density of 0.1, 0.5 and 1 mA cm^{-2}.

Figure 18. (a) Photograph of the prototype cable-type flexible ZAB. (b) Optical microscopy (OM) for cross-sectional image of the cable-type flexible ZAB. (c) Discharge curves of stack-type and cable-type ZAB with and without Fe/N/C electrocatalysts, respectively. The discharge current density was 0.1 mA cm^{-2}. (d) Discharge curves of cable-type ZAB by applying bending strain every 20 min at discharge current density was 0.1 mA cm^{-2} (Discharge tests of the battery were carried out using ambient static air at 24 °C).

Figure 19. Electrochemical characterizations for stack-type Zn−air battery. (a) Schematic diagram of stack-type ZAB. (b) Power-current curves of stack-type ZABs with Fe/N/C-900 and 20% Pt/C electrocatalysts. (c) Discharge curves of stack-type ZABs for current density at 50 mA cm^{-2} and (d) at 25 mA cm^{-2} by using zinc granular and 6 M KOH liquid electrolyte.

Figure 20. (a) Current-voltage of stack-type Zn–air batteries with Fe/N/C-900 (with zinc granular) and (b) discharge curve for discharge current density at 100 mA cm^{-2}.

Figure 21. The magnified data of discharge curves of stack-type and cable-type ZAB with and without Fe/N/C electrocatalysts.

Figure 22. Digital photograph and schematic diagram of stack-type Zn–air battery.

Figure 23. Real image of connected cable-type flexible Zn–air battery in series (a) with LED and (b) its open circuit voltage (OCV).

Figure 24. Preparation, morphology and structural characterization of the highly pure single crystalline pyrochlore oxide nanoparticles ($A_2B_2O_{7-x}$, A = Pb and Sm, B = Ru). (a) Schematic representation of the preparation process for the highly pure single crystalline pyrochlore oxide nanoparticles. During sol-gel process, A-site cations (blue spheres) are crosslinked with B-site cations (green spheres) by citric acid (black lines). After heat-treated at the different temperature (650 °C for $Pb_2Ru_2O_{6.5}$ and 1,050 °C for $Sm_2Ru_2O_7$), the powdered pyrochlore member (red brown solid figures) are synthesized. (b) XRD patterns of $Pb_2Ru_2O_{6.5}$ and $Sm_2Ru_2O_7$. (c) SEM image, (d) FFT image of HR-TEM along the [110] zone axis and (e) STEM-HAADF image of $Pb_2Ru_2O_{6.5}$. In (d), the indexed points refer to the lattice planes of (–11–1), (–220), (–111) and (002) in clockwise order. In (e), 0.304 and 0.510 nm denote the lattice spacing on the (111) and (002) planes, respectively.

Figure 25. (a) SEM image of $Sm_2Ru_2O_7$. The primary particles of the pyrochlore catalyst showed angular shapes with average sizes of ≈200 nm. (b) HR-TEM FFT image along the [110] zone axis with indexed unit spots of $Sm_2Ru_2O_7$. The indexed points refer to the lattice planes of (–11–1), (–220), (–111) and (002) in clockwise order. (c) Lattice scale STEM-HAADF image with d-spacing of $Sm_2Ru_2O_7$. 0.306 nm and 0.511 nm denote the lattice spacing indicated by yellow arrows and lines, on the (111) and (002) planes, respectively.

Figure 26. STEM-HAADF-EDS images of $Pb_2Ru_2O_{6.5}$ and elemental maps of (a) all elements, (b) Pb, (c) Ru and (d) O.

Figure 27. (a) STEM and (b) EDS of $Pb_2Ru_2O_{6.5}$ at different point.

Figure 28. STEM–HAADF–EDS images of $Sm_2Ru_2O_7$ and element maps of (a) all elements, (b) Sm, (c) Ru and (d) O.

Figure 29. (a) STEM and (b) EDS of $Sm_2Ru_2O_7$ at different points.

Figure 30. Electrocatalytic activities for ORR and OER on the highly pure single crystalline pyrochlore oxide nanoparticles ($A_2B_2O_{7-x}$, A = Pb and Sm, B = Ru). (a) Linear scan voltammogram (LSV) curves and (b) the number of transferred electrons in O_2-saturated 0.1 M KOH at a rotation speed of 1,600 rpm and scan rate of 10 mV s^{-1} for $Pb_2Ru_2O_{6.5}$, $Sm_2Ru_2O_7$ and Pt/C at a rotating ring-disk electrode (RRDE). (c) Tafel plots of log I_k (A) vs. E (V vs. reversible hydrogen electrode (RHE)) for the pyrochlore catalysts and Pt/C at the potential range for the ORR. In (c), the limiting current density obtained at potential = 0.35 V was used to calculate i_k using the equation, $i_k = i_L \bullet i/(i_L - i)$. (d), Kinetic current density of the pyrochlore oxides and Pt/C at 0.85 V. (e) LSV curves of the pyrochlore oxides and RuO_2. (f) Tafel plots of log J_k (mA cm^{-2}) vs. E (V vs. RHE) for the pyrochlore oxides and RuO_2 at the potential range for the OER.

Figure 31. *Ex situ* XANES and *in situ* XAS analyses of the highly pure single crystalline pyrochlore oxide nanoparticles ($A_2Ru_2O_{7-x}$, A = Pb and Sm). (a) Schematic representation of *in situ* XAS design combined with XAS and a three-electrode half-cell. The half-cell consists of the pyrochlore oxide-based air electrode as the working electrode, Hg/HgO reference electrode and Pt wire as the counter electrode in 0.1 M KOH electrolyte. Incident X-rays (I_o) are absorbed by the pyrochlore oxide-based air electrode and emit photons towards the fluorescence detector during the ORR and OER. (b) Normalized ruthenium K-edge XANES spectra for Ru metal, RuO_2, $Pb_2Ru_2O_{6.5}$ and $Sm_2Ru_2O_7$. (c) Normalized oxygen K-edge XANES total electron yield mode spectra for the pyrochlore catalysts. (d) Potentials at –25 and 25 μA cm^{-2} as a function of the Ru-O bonding covalency in the pyrochlore oxides for ORR and OER, respectively. (e) The corresponding interatomic distances for the reduced distances of the pyrochlore oxides at various applied potentials during electrocatalysis.

Figure 32. Photograph of three electrodes half-cell for *in situ* XAS analysis. The half-cell consists of the pyrochlore oxides based air electrode as working electrode, Hg/HgO reference electrode and Pt wire as counter electrode in 0.1 M KOH electrolyte.

Figure 33. Chronoamperometric tests of (a) $Pb_2Ru_2O_{6.5}$ and (b) $Sm_2Ru_2O_7$ in 0.1 M KOH at 0.7 V, 0.5 V and 0.3 V (vs. RHE) for *in situ* XAS analysis during the ORR. Chronoamperometric tests of (c) $Pb_2Ru_2O_{6.5}$ and (d) $Sm_2Ru_2O_7$ in 0.1 M KOH at 1.3 V, 1.5 V and 1.7 V (vs. RHE) for *in situ* XAS analysis during the OER.

Figure 34. Performance of primary and rechargeable Zn–air batteries based on the highly pure single crystalline pyrochlore oxide nanoparticles ($A_2Ru_2O_{7-x}$, A = Pb and Sm). (a) Current density–voltage curves, (b) power–current density curves and (c) discharge curves at a current density of 20 mA cm^{-2} of primary Zn–air batteries using $Pb_2Ru_2O_{6.5}$, $Sm_2Ru_2O_7$ and Pt/C-based air electrodes as ORR catalysts. (d) Anodic and cathodic polarization curves of rechargeable Zn–air batteries with the pyrochlore oxide catalysts and mixture of Pt/C and IrO_2 catalyst. (e) Discharge and charge cycling curves of rechargeable Zn–air batteries based on $Pb_2Ru_2O_{6.5}$ and the mixture of Pt/C and IrO_2 at a current density of 10 mA cm^{-2} in short cycle periods (600 s per cycle) and (f) long cycle periods (2 h per cycle) with ambient air.

Figure 35. Discharge and charge cycling curves of rechargeable Zn–air batteries at the current density of 10 mA cm^{-2} in short cycle periods (600 sec per cycle) with ambient air based on (a) $Pb_2Ru_2O_{6.5}$ and (b) $Sm_2Ru_2O_7$. Discharge and charge cycling curves of rechargeable Zn–air batteries at the current density of 10 mA cm^{-2} in long cycle periods (2 h per cycle) with ambient air based on (c) $Pb_2Ru_2O_{6.5}$ and (d) $Sm_2Ru_2O_7$.

Figure 36. Durability tests of pyrochlore oxide catalysts. (a) Normalized ruthenium K-edge XANES for pristine (solid line) and 100^{th} cycled (dashed line) pyrochlore catalysts. (b) Fourier-transformed radial distribution function of ruthenium K-edge EXAFS for pristine and 100^{th} cycled pyrochlore catalysts. (c) XRD patterns for 100^{th} cycled pyrochlore catalysts.

Figure 37. Preparation, morphology and structural characterization of nanocrystalline pyrochlore oxides ($A_2[B_{2-x}A_x]O_{7-y}$). (a) Schematic of the synthesis process of yttrium ruthenate nanoparticles ($Y_2[Ru_{2-x}Y_x]O_{7-y}$), hereafter referred to as a YRO, with pyrochlore structure by sol-gel method. They consist of trivalent yttrium (red sphere), tetravalent ruthenium (blue sphere), and divalent oxygen ions (green sphere) that bonds them together. (b) Powder XRD patterns of YRO nanoparticles. (c) SEM image of YRO, and inset showing the magnified image. (d) STEM-HAADF-EDS images of the YRO with elemental maps of yttrium and ruthenium. (e,f) The HR-TEM images of the YRO nanoparticles at (e) low and (f) high magnifications. The inset of (f) indicates the FFT pattern of HR-TEM for YRO along the [110] main zone axis. The indexed spots refer to the lattice planes of (–111), (–11–1), (002) and (–220) in the pyrochlore structure. (g,h) The corresponding STEM-HAADF images of YRO with d-spacing values of (g) 0.30 nm and (h) 0.51 nm correspond to (111) and (002) crystal planes, respectively.

Figure 38. (a) STEM-HAADF-EDS images of the YRO and (b) elemental maps of oxygen.

Figure 39. STEM-EDS of the YRO at different point.

Figure 40. Electrocatalytic activities of the nanocrystalline YRO with pyrochlore structure. (a) Linear

scan voltammogram (LSV) curves of the YRO and Pt/C during ORR, and inset showing the number of transferred electrons of the YRO and Pt/C. The electrochemical characterizations were performed using a rotation ring-disk electrode (RRDE) in O_2-saturated 0.1 M KOH at a rotation speed of 1600 rpm and scan rate of 10 mV s^{-1}. The ORR potential ranged from 1.13 to 0.26 V vs. RHE. (b) LSV curves of the YRO and IrO_2 during OER, and inset indicates the current density of the YRO and IrO_2 at a potential of 1.7 V. The OER potential ranged from 1.23 to 1.82 V. (c) The current density–voltage curves and (d) discharge curves at a current density of 20 mA cm^{-2} of the primary Zn–air batteries using the YRO and Pt/C. (e) Anodic and cathodic polarization curves of the rechargeable Zn–air batteries using the YRO and the mixture of Pt/C and IrO_2. (f) The battery cycling curves of the rechargeable Zn–air batteries using the YRO and the mixture of Pt/C and IrO_2 during charging and discharging processes at a current density of 10 mA cm^{-2} in short cycle periods (10 min per cycle) with ambient air.

Figure 41. The number of transferred electrons (n) of the YRO and Pt/C during ORR.

Figure 42. The nitrogen adsorption-desorption isotherm. The YRO showed a BET surface area of 4.2634 m^2 g^{-1}.

Figure 43. The normalized LSV curve of the YRO during ORR based upon the real surface area.

Figure 44. Tafel plots of log I_k (A) vs. E (V vs. RHE) for the YRO and Pt/C.

Figure 45. The LSV curves of the YRO and RuO_2 during OER.

Figure 46. The normalized LSV curve of the YRO during OER based upon the real surface area.

Figure 47. Tafel plots of log J_k (mA cm^{-2}) vs. E (V vs. RHE) for the YRO and IrO_2.

Figure 48. Power–current density of the primary Zn–air batteries using the YRO and Pt/C.

Figure 49. The battery cycling curves of the rechargeable Zn–air batteries using the YRO and the mixture of Pt/C and IrO_2 during charging and discharging processes at a current density of 10 mA cm^{-2} in long cycle periods (2 h per cycle) with ambient air.

Figure 50. The X-ray absorption near edge structure (XANES) spectra of the nanocrystalline YRO with pyrochlore structure by *in situ* XAS analysis. (a) Cyclic voltammogram of the air electrode containing the YRO simultaneously with XAS analysis for yttrium and ruthenium cations. The scan rate of CV was 0.085 mV s^{-1}. The CV during the ORR and OER was recorded between 0.23 and 1.43 V vs. RHE. The corresponding ORR and OER potentials ranged from 0.93 to 0.23 and 1.43 V, respectively. The scan number of XAS analysis for ORR ranged from 1^{st} to 11^{th}, and OER ranged from 1^{st} to 7^{th}. (b,c) Normalized ruthenium K-edge XANES spectra of the YRO simultaneously with CV test during (b) ORR and (c) OER, and insets showing the magnified data. (d,e) Normalized yttrium K-edge XANES spectra of the YRO during (d) ORR and (e) OER, and the insets indicate the magnified data.

Figure 51. (a) Photograph of *in situ* XAS electrochemical cell consisting of three-electrode electrochemical cell and XAS instrument. (b) Photograph of the three-electrode electrochemical cell consisting of working electrode (air electrode), reference electrode (Hg/HgO electrode) and counter electrode (Pt wire).

Figure 52. The extended X-ray absorption fine structure (EXAFS) spectra of the nanocrystalline YRO with pyrochlore structure by *in situ* XAS analysis. (a,b) Normalized radial distribution function (RDF) of Fourier-transformed k^3-weighted EXAFS spectra for ruthenium ions of the YRO during (a) ORR and (b) OER, and insets showing the magnified data. The ORR and OER potentials ranged from 0.93 to 0.23 and 1.43 V vs. RHE, respectively. The scan number of XAS analysis for ORR ranged from 1st to 11th, and OER ranged from 1st to 7th. (c,d) Normalized RDF of Fourier-transformed k^3-weighted EXAFS spectra for yttrium ions of the YRO during (c) ORR and (d) OER, and insets indicate the magnified data.

Figure 53. The catalytic origin of the nanocrystalline YRO with pyrochlore structure during electrocatalysis. (a) Schematic representations of the *in situ* XAS results for the YRO, showing the oxidations of yttrium and ruthenium ions and highly stable RuO_6 structure during ORR and OER. (b,c) The oxidation states of ruthenium and yttrium ions of the YRO during (b) ORR and (c) OER upon CV test simultaneously with XAS analysis. The relative oxidation states correspond to the photon energies at the highest peaks of XANES spectra. The CV during the ORR and OER was recorded between 0.23 and 1.43 V vs. RHE. The corresponding ORR and OER potentials ranged from 0.93 to 0.23 and 1.43 V, respectively. The scan number of XAS analysis for ORR ranged from 1st to 11th, and OER ranged from 1st to 7th. (d,e) The reduced distances of Y-O bonds at A-sites, B-sites, and Ru-O bonds at B-sites of the YRO during (d) ORR and (e) OER upon CV test simultaneously with XAS analysis. The reduced distances were obtained by the experimental EXAFS spectra.

Figure 54. Preparation, morphology and structural characterization of polyhedral pyrochlore oxides ($A_2B_2O_7$). (a) Schematic of the synthesis process of polyhedral bismuth ruthenate pyrochlore ($Bi_2Ru_2O_7$), hereafter referred to as a BRO, with pyrochlore structure by sol-gel method. They consist of trivalent bismuth (blue sphere), tetravalent ruthenium (green sphere), and divalent oxygen ions that bonds them together. (b) Powder XRD patterns of BRO nanoparticles. (c) SEM image of BRO. (d,e) STEM-HAADF-EDS images of the BRO with elemental maps of (d) bismuth and (e) ruthenium. (f,g) The HR-TEM images of the BRO at (f) low and (g) high magnifications. The inset of (g) indicates the FFT pattern of HR-TEM for BRO along the [110] main zone axis. The indexed spots refer to the lattice planes of (–111), (–11–1), (002) and (–220) in the pyrochlore structure. (h) The corresponding STEM-HAADF images of BRO with d-spacing values of 0.30 nm and 0.51 nm correspond to (111) and (002) crystal planes, respectively.

Figure 55. *In situ* TEM analysis. (a,b) Time-lapse sequence of STEM images for the polyhedral bismuth ruthenate pyrochlore oxide during crystallization at an elevated temperature of 1,050 °C, showing structural determination processes including (a) Ostwald ripening- and (b) facets evolution-stages. (c) Time-lapse sequence of the schematic representation of the structural determination processes.

Figure 56. Electrocatalytic activities of the polyhedral BRO with pyrochlore structure. (a) Linear scan voltammogram (LSV) curves of the BRO and Pt/C during ORR. The electrochemical characterization

were performed using a rotation ring-disk electrode (RRDE) in O_2-saturated 0.1 M KOH at a rotation speed of 1600 rpm and scan rate of 10 mV s^{-1}. The ORR potential ranged from 1.13 to 0.26 V vs. RHE. (b) LSV curves of the BRO and IrO_2 during OER, and inset indicates the current density of the BRO and IrO_2 at a potential of 1.7 V. The OER potential ranged from 1.23 to 1.82 V. (c) Discharge curves of stack- and flow-type Zn–air batteries at a current density of 20 mA cm^{-2}. (d,e) Discharge curves of the flow-type Zn–air batteries using the BRO and Pt/C at a current density of 20 mA cm^{-2}. (f) The battery cycling curves of the rechargeable Zn–air flow batteries using the BRO and the mixture of Pt/C and IrO_2 during charging and discharging processes at a current density of 10 mA cm^{-2} in short cycle periods (10 min per cycle) with ambient air.

List of Tables

List of publications

I contributed to the following publications during my PhD course.

Peer-reviewed publications

1. **Park J.**, Park M., Nam G., Kim M. G.*, Cho J.* "Unveiling the catalytic origin of nanocrystalline yttrium ruthenate pyrochlore as a bi-functional electrocatalyst for Zn–air batteries", *Nano Lett.*, 17, 3974-3981 (**2017**).
2. **Park J.**, Risch M., Nam G., Park M., Shin T. J., Park S., Kim M. G.*, Shao-horn Y.*, Cho J.* "Single crystalline pyrochlore nanoparticles with metallic conduction as efficient bi-functional oxygen electrocatalysts for Zn–air batteries", *Energy Environ. Sci.*, 10, 129-136 (**2017**).
3. Nam G., **Park J.**, Choi M., Oh P., Park S., Kim M., Park N., Cho J.*, Lee J.* "Carbon-Coated Core-Shell Fe-Cu Nanoparticles as Highly Active and Durable Electrocatalysts for a Zn–Air Battery", *ACS Nano*, 9, 6493-6501 (**2015**).
4. **Park J.**, Park M., Nam G., Lee J., Cho J.* "All-Solid-State Cable-Type Flexible Zinc-Air Battery", *Adv. Mater.*, 27, 1396-1401 (**2015**).
5. Jung J., Jeong H., Kim M., Nam G., **Park J.**, Cho J.* "Fabrication of $Ba_{0.5}Sr_{0.5}Co_{0.8}Fe_{0.2}O_{3-\delta}$ Catalysts with Enhanced Electrochemical Performance by Removing an Inherent Heterogeneous Surface Film Layer", *Adv. Mater.*, 27, 266-271 (**2015**).
6. Nam G.†, **Park J.†**, Kim S., Shin D., Park N., Kim Y., Lee J.*, Cho J.* "Metal-Free Ketjenblack incorporated Nitrogen-Doped Carbon Sheets Derived from Gelatin as Oxygen Reduction Catalysts", *Nano Lett.*, 14, 1870-1876 (**2014**).

Conference contributions

1. *2016 MRS Fall Meeting*, Boston, MA, U.S., November **2016**, "Polyhedral Shaped Pyrochlore Oxides as Bi-functional Electrocatalysts for Zinc-air Flow Batteries", Oral presentation
2. *4th Nano today Conference*, Dubai, December **2015**, "Pyrochlore Oxides as Oxygen Reduction and Evolution Electrocatalyst for Rechargeable Zn–air Battery", Oral presentation
3. *248th ACS Fall Meeting*, San Francisco, CA, U.S., August **2014**, "All-Solid-State Cable-Type Flexible Zinc-Air Battery", Oral presentation

Chapter 1

Introduction of electrocatalysts for Zn–air batteries

1.1 Introduction

The growing environmental deterioration and rapid depletion of fossil fuels, such as coal, oil and natural gas, have led to urgent needs of the electrochemical energy devices.[1] With demands for alternatives to petroleum fuels, the energy conversion and storage system have been developed. Moreover, as the needs of portable electronic devices with high power and energy density have been increased. To meet these demands, various power sources including Ni-MH batteries and lithium-ion batteries (LIBs) have been the most intensively studied because of their high power density, stable durability and safety upon cycling.[2] However, the energy density of conventional LIBs (≈250 Wh kg^{-1}) is not enough for operating next generation electric vehicles. Thus, metal-air batteries have been considered as promising electrical energy storage (EES) systems due to their environmental benignity and high specific energy densities (**Figure 1**). The significance of the system is open cell structure in order to use the oxygen gas as a cathode material from the ambient air.[3] There are various metal-air batteries based on the types of metal such as lithium, zinc, cadmium, aluminum, iron and calcium.[4] In this regard, there are various reaction mechanisms during charging and/or discharging processes in accord with metals, resulting in the different cell components. The reported metal-air batteries can be classified into two types based on the electrolytes; that is, the aqueous and aprotic solvents. In terms of moisture effects, metal-air batteries based on the aqueous electrolyte show highly stable electrochemical performance. In contrast, the electrochemical performance of that of the aprotic electrolyte can be degraded because of moisture sensitive property. Among a variety of metal-air batteries, Zn–air batteries have emerged as the most promising candidates because of high energy density (ca. 1,084 Wh kg^{-1}), low cost of zinc metal anode and high safety with aqueous electrolytes.[5, 6] Notably, Zn–air batteries demonstrates the highest specific capacity among various metal-air batteries including Fe–, Cd– and Pb–air batteries, which could be charged and discharged in aqueous solution (**Figure 2**).[7]

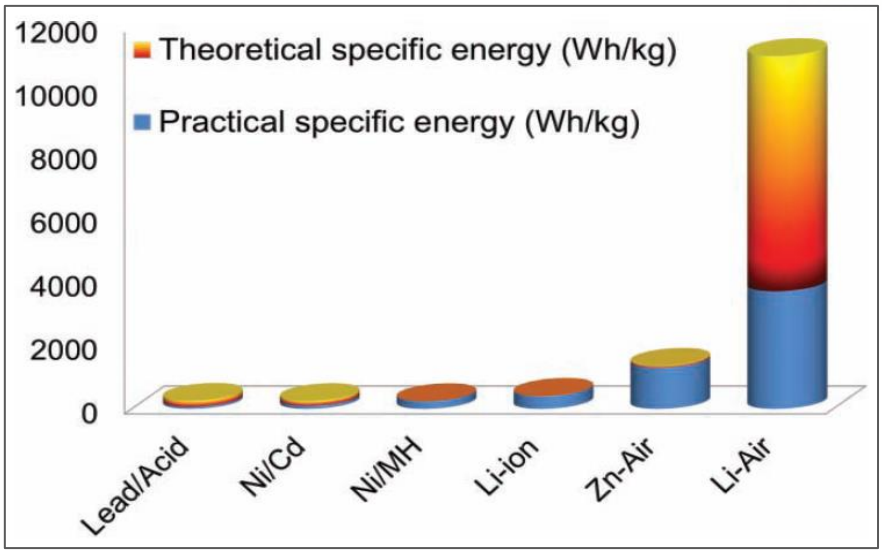

Figure 1. Theoretical and practical energy densities of various types of rechargeable batteries.

This part was reproduced from Lee J.-S., Kim S. T., Cao R., Choi N.-S., Liu M., Lee K. T., *et al.* Metal–Air Batteries with High Energy Density: Li–Air versus Zn–Air. *Adv. Energy Mater.*, **1**, 34-50 (2011).

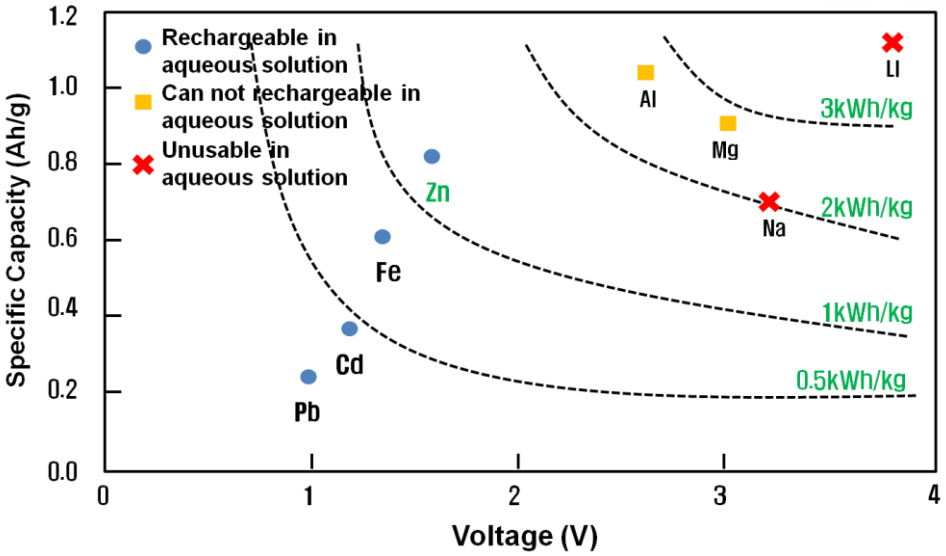

Figure 2. Rechargeability of metal in aqueous solution.

This part was reproduced from Zhang. Zinc-air technology. *Int. Zn. Assoc.*, (2005).

1.2 Principle of Zn–air batteries

Zn–air batteries consists of zinc metal anode, carbon air cathode containing the electrocatalysts, potassium hydroxide electrolyte and separator (**Figure 3**).[4] On discharging, the zinc metal anode is oxidized to divalent zinc ion, providing soluble zincate ions ($Zn(OH)_4^{2-}$). This reaction is occurred until saturation of the zincate ions in the electrolyte.[8] After the saturation, ZnO particles are deposited on the surface of air electrode during discharging process, resulting from the saturation of the zincate ions as shown by the equations below.[9]

Cathode:

$$O_2 + 2H_2O + 4e^- \rightarrow 4OH^- \qquad E^0 = 0.4 \text{ V vs. NHE} \qquad (1)$$

Anode:

$$Zn \rightarrow Zn^{2+} + e^- \qquad (2)$$

$$Zn^{2+} + 4OH^- \rightarrow Zn(OH)_4^{2-} \qquad E^0 = -1.25 \text{ V vs. NHE} \qquad (3)$$

$$Zn(OH)_4^{2-} \rightarrow ZnO + H_2O + 2OH^- \qquad (4)$$

$$Zn + 2H_2O \rightarrow Zn(OH)_2 + H_2 \qquad (5)$$

Overall reaction:

$$2Zn + O_2 \rightarrow 2ZnO \qquad E^0 = 1.65 \text{ V vs. NHE} \qquad (6)$$

Moreover, an undesirable reaction is occurred between aqueous electrolyte and zinc metal anode spontaneously with generating hydrogen gas.[10] This result could be ascribed to the self-corrosion of zinc metal anode, resulting in low utilization of the metal. In parallel with the oxidation of zinc metal anode, the oxygen is reduced to hydroxide ions at air cathode.[11] On charging, both of the oxidation and reduction reactions are reversed. The oxygen reduction reaction (ORR) and oxygen evolution reaction (OER) are key factors to determine the electrochemical performance during discharging and charging processes, respectively.[12] The slow kinetics of ORR and OER hamper the discharging and charging processes of Zn–air batteries

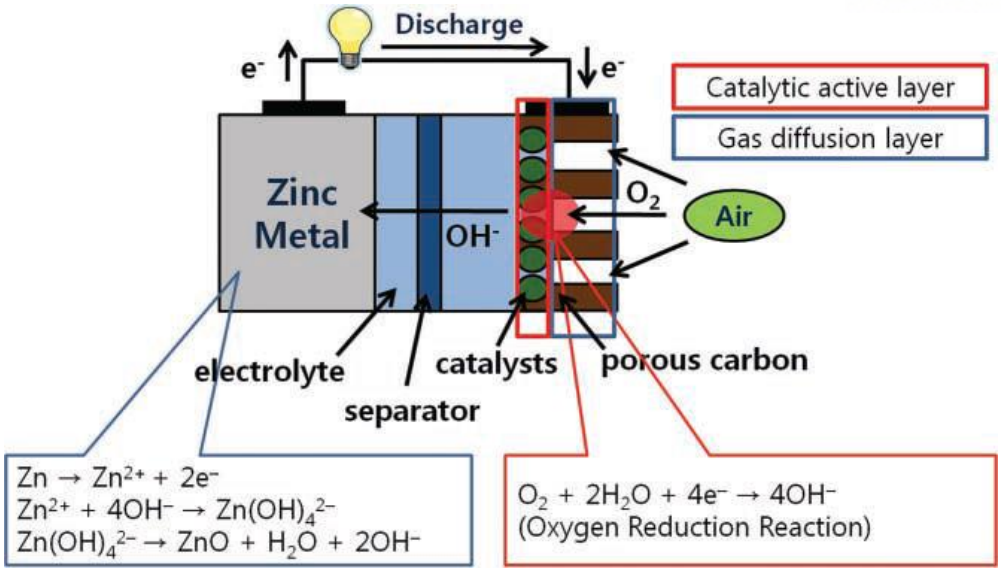

Figure 3. Working principle and electrochemical reactions at cathode and anode of Zn–air batteries.

This part was reproduced from Lee J.-S., Kim S. T., Cao R., Choi N.-S., Liu M., Lee K. T., *et al.* Metal–Air Batteries with High Energy Density: Li–Air versus Zn–Air. *Adv. Energy Mater.*, **1**, 34-50 (2011).

Zinc metal anode

To date, zinc metal have been extensively used as anode for various primary batteries including zinc-nickel, zinc-carbon, zinc-manganese dioxide and zinc-air batteries.[13] Zinc metal have been considered as the promising metal anodes for a variety of batteries because of highly stable in aqueous solution, high specific energy density, abundance and low toxicity.[5] In terms of the morphology of zinc metal, the granulated zinc powder have been used for commercialized zinc batteries. The zinc granules have been selected as anode materials because of highly improved inter particle contact and reduced internal resistance based upon that of particle size and morphology. In other words, the higher surface area of zinc metal particles could improve the electrochemical performance of the batteries. Oyama *et al.* reported the zinc metal powder based upon optimized ratio between coarse and fine particles for high rate performance and self-corrosion, respectively.[14] In addition, a variety of zinc metal electrode with high surface including sphere-, ribbon-, flake-, dendrite- and fiber-shaped morphology have been intensively investigated.[15-17] For example, the zinc foam was synthesized by consolidation of emulsified zinc suspensions.[18] The degree of porosity of the electrode could be controlled by the concentration of dispersed phase in the emulsion. Notably, they demonstrated highly improved electrochemical performance with energy density of ≈300 Wh kg^{-1}. However, high surface area of the electrode could increase the corrosion rate of zinc metal. This undesirable reaction degraded the zinc utilization of the batteries, resulting in low potential retention upon battery cycling. Thus, the alloyed zinc metal with other metals such as bismuth, cadmium, lead, tin and indium have been emerged as alternatives for zinc metal anode.[19, 20] The additives for the zinc electrode including polymers, surfactants and silicates also reported.[21, 22] In particular, they effectively hampered the generation of hydrogen gas.[23] Moreover, the electrochemical performance of zinc electrode could be highly improved by coating. Example includes the lithium boron oxides and aluminium oxides.[24] The coating materials substantially reduce the hydrogen generation, self-discharge and corrosion rate of zinc metal particles, resulting in increase of discharge capacity. In summary, zinc metal anode should be further developed by using various methods such as alloying, coating and adding additives for Zn–air batteries.

Air electrode

In general, the oxygen is reduced at the triple phase boundary during ORR, where the air cathode is directly contact with the gas phase and ionic conductor of electrolyte.[10] The diffusion rate of the oxygen in the gas phase is much faster than that of the electrolyte because of the low diffusivity and solubility of the gas in liquid. The conventional air cathodes demonstrate low current density during ORR, which could be ascribed to the ineffective triple phase reaction. In order to increase the electrochemical performance of the air cathode, a design of gas diffusion electrode with porous structure is needed. At the initial stage of the development of Zn–air batteries, the platinized air cathode with porous carbon was reported in 1878.[25] In 1932, Heise *et al.* reported the Zn–air batteries with alkaline solution by using wax treated air cathode to prevent the electrolyte penetration.[26] Thereafter, the polytetrafluoroethylene (PTFE) bonded air cathode with porous carbon was developed.[27] Importantly, the air cathode consisted of two main components including hydrophobic and hydrophilic materials. The hydrophobic component could act as a protective layer for preventing electrolyte leakage. Moreover, it provides diffusion pathway for oxygen, resulting in the increase of catalytic active sites. In contrast, the hydrophilic component facilitate the high wettability of the air cathode with liquid electrolyte. Notably, the environmental condition significantly affects the electrochemical performance of Zn–air batteries. For example, the electrolyte could be dried or leaked out of the air cathode depending on the degree of humidity. Therefore, the ratio between hydrophobic and hydrophilic components of the air cathode should be optimized for reducing the evaporation and flooding of electrolyte during battery cycling. The ratio could be determined by controlling the amount of PTFE during electrode fabrication.[28, 29] To date, a variety of PTFE bonded air cathode have been reported for metal-air batteries based on aqueous electrolyte. In 1980, Toray Industries commercialized the gas diffusion electrode (GDE). The GDE effectively provided high electrical conductivity and porosity resulting from binding between carbon fibers and graphitized carbon. The bonded PTFE controlled the wettability of the air cathode. In addition, the thinner GDE could increase the oxygen gas permeability. Consequently, the GDE should be further investigated to optimize their physical and chemical properties simultaneously with the development of electrolyte and electrocatalysts.

Electrolyte

The most of Zn–air batteries can be operated in alkaline solutions including potassium hydroxide and sodium hydroxide because of the proper pH value for high electrochemical performance of zinc metal anode and air cathode.[10] Among them, the potassium hydroxide have been considered as the most promising candidates for electrolyte of Zn–air batteries due to the low viscosity, high ionic conductivity and high oxygen diffusivity.[30] In general, Zn–air batteries demonstrates the significantly improved electrochemical performance in potassium hydroxide solution with concentration of 7 M (≈30 wt%), which could provide the highest electrical conductivity. However, the evaporation of electrolyte is critical issue of Zn–air batteries based on open system. In order to prevent the water loss, the gelation of electrolyte have been studied. Othman *et al.* reported a hydroponic gel that could immobilize potassium hydroxide solution of Zn–air batteries.[31] Thereafter, various gelling agents such as polyethylene oxide (PEO) and polyvinyl alcohol (PVA) were developed.[32] Notably, they demonstrated substantially enhanced mechanical strength and electrochemical stability for Zn–air batteries. Recently, the aprotic solution including ionic liquids has been emerged as promising electrolyte for Zn–air batteries. Interestingly, they hampered the deposition of zinc dendrite, resulting in highly stable cyclability of zinc metal anode. Moreover, the reactivity with zinc metal and evaporative property of the aprotic electrolytes are less than that of aqueous electrolyte. However, the reaction mechanism of electrocatalysts in the aprotic electrolytes is different from that of aqueous media.[33] Furthermore, the air cathode suffers from wetting in the aprotic electrolytes. In this context, Harting *et al.* observed the degraded operating potential of Zn–air batteries based on the aprotic electrolyte because of high viscosity.[34] As a result, further studies are required for developing electrolytes with optimized conditions for various factors, demonstrating high electrochemical performance of Zn–air batteries.

Separator

In battery system, separator is an essential component for physical separation between cathode and anode. Although the separator is an inactive component for electrochemical reaction, the various types of separator affect the performance of Zn–air batteries. In order to demonstrate the high electrochemical performance of Zn–air batteries, the separators should provide high electrical resistance and ionic diffusivity. Moreover, high structural stability of the separator is required for the battery safety, resulting from the deposition of zinc dendrite upon battery cycling. To date, a variety of nonwoven polymeric separators including polyvinyl alcohol (PVA), polyethylene (PE) and polypropylene (PP) have been extensively employed in metal-air batteries.[6, 35] Notably, the fibrous structure of nonwoven separator needs high porosity for low ionic resistance and highly stable retention. In general, commercialized Zn–air batteries use the laminated nonwoven separators that are produced by Celgards. The commercialized separators consist of three layers (PP/PE/PP). The PP and PE exhibited high structural integrity and shut down the battery at elevated temperature, respectively. Recently, new types of separators with chemical treatment have been intensively studied for Zn–air batteries. Wu *et al.* developed the sulfonated nonwoven PE/PP separators, demonstrating highly improved ionic conductivity and hydrophilicity in alkaline electrolytes.[36, 37] Moreover, the inorganic microporous membranes also reported as alternative materials for separators.[38] The structure of inorganic separators are more stable at elevated temperature than that of organic polymers. However, the soluble zincate ions could easily permeate from anode to cathode through the inorganic separators. Accordingly, the polarization and battery cycling efficiency are increased and decreased, respectively. In this regard, the anion exchange membranes have emerged as alternatives separators, which could selectively permeate the hydroxide ions. Dewi *et al.* reported a poly(methylsufonio-1,4-phenylenethio-1,4-phenylenetriflate) membrane based upon high anion selectivity.[39] Although the anion exchange membranes effectively hamper the crossover of zinc species, the electrochemical performances of Zn–air batteries were degraded with insufficient long-term stability.[40] In conclusion, a novel separator with proper permeability of hydroxide ions and zinc species is required for significantly enhanced electrochemical performance and stability of next generation Zn–air batteries.

1.3 Materials and chemistry for electrocatalysts

In the twenty-first century, environmental friendly energy sources have been extensively developed as alternatives to petroleum fuels for providing sustainable and clean energy.[1] Notably, Zn–air batteries have attracted great research interest for electrochemical energy storage (EES) systems because of high energy density, environmental friendly components, high safety and low cost.[4] However, there are critical issues for highly improved electrochemical performance, which ascribe to the sluggish ORR and OER during discharging and charging processes, respectively (**Figure 4**). The detailed equations for both of the reactions are described, respectively, as follows.

Oxygen reduction reaction (ORR):

$$O_2 + 2H_2O + 4e^- \rightarrow 4OH^- \qquad E^0 = 0.4 \text{ V vs. NHE} \qquad (7)$$

Oxygen evolution reaction (OER):

$$4OH^- \rightarrow O_2 + 2H_2O + 4e^- \qquad E^0 = -0.4 \text{ V vs. NHE} \qquad (8)$$

To date, Pt have been reported as the most outstanding electrocatalyst for ORR because of the high catalytic activity. However, many researchers have been hampered improving the Pt based electrocatalysts due to the scarcity of Pt. Moreover, the stability of Pt in alkaline solution is lower than that of various electrocatalysts including metal free-, non-precious metal-, and metal oxide-based catalysts. Therefore, the alternative inexpensive catalysts with high ORR activity should be intensively studied.[41, 42] In terms of OER activity, IrO_2 and/or RuO_2 are known as the most promising electrocatalysts. However, bi-functional electrocatalysts based upon highly enhanced electrochemical performance in both of ORR and OER should be developed for rechargeable Zn–air batteries.

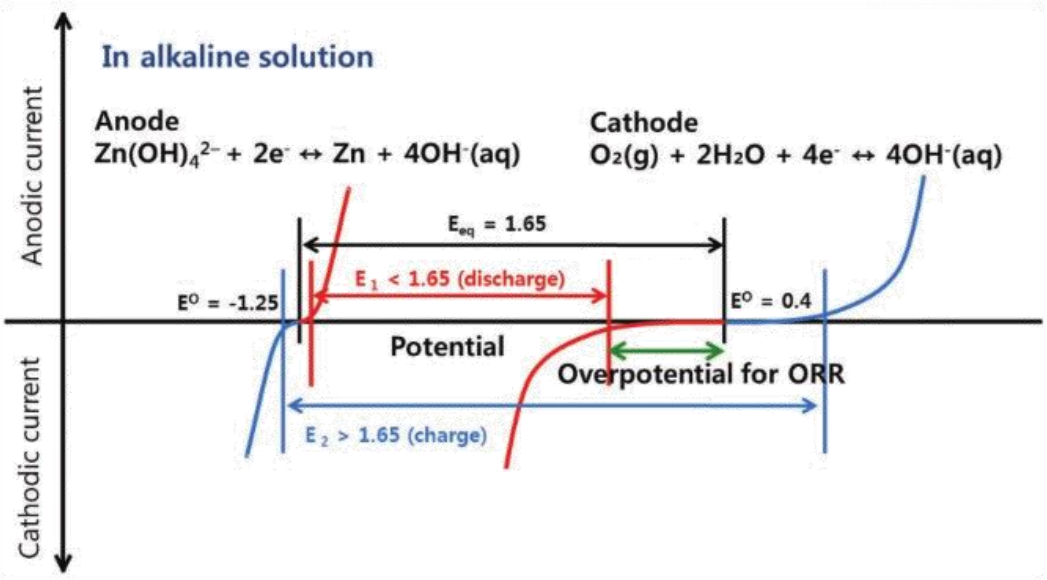

Figure 4. Schematic polarization curves of Zn–air batteries.

This part was reproduced from Lee J.-S., Kim S. T., Cao R., Choi N.-S., Liu M., Lee K. T., *et al.* Metal–Air Batteries with High Energy Density: Li–Air versus Zn–Air. *Adv. Energy Mater.*, **1**, 34-50 (2011).

Metal-free electrocatalysts

Recently, carbon based ORR electrocatalysts have been considered as promising candidates for Zn–air batteries. However, pristine carbon materials showed degraded catalytic activities with predominant two-electron pathway forming peroxides in aqueous solutions during ORR.[43-45] Accordingly, chemical modifications are required for enhancing the electrocatalytic activity of the carbon materials.[46] Among them, nitrogen-doped carbon materials have been intensively studied as efficient metal-free electrocatalysts.[47-49] They provide the disordered carbon nanostructure and high surface polarity based upon electron donation from nitrogen to adjacent carbon. Note that carbon materials formed pyrrolic, pyridinic and graphitic nitrogen by reacting with nitrogen species at elevated temperature. In this regard, the defects of graphene edge derived from the reaction showed higher catalytic activity than that of graphene plane because of the high oxygen adsorption at the edge sites.[50, 51] In terms of catalytic activity, heat treatment is the most promising synthesis method for the nitrogen-doped carbon materials.

Non-precious metal catalysts (NPMC)

The nitrogen-doped metal-free materials have been widely reported as electrocatalysts for ORR in alkaline solution. However, they showed still limited electrocatalytic activity, which is lower than that of state-of-the-art platinum. Thus, the metal/nitrogen/carbon (M/N/C) materials, hereafter referred to as a NPMC, have been emerged as more promising electrocatalysts for Zn–air batteries than the metal-free materials. In general, the electrocatalysts are synthesized by heat treatment at elevated temperature of around 900 °C using iron, cobalt and nitrogen precursors with carbon support.[52-54] Importantly, the metal cations coordinated by nitrogen in the NPMC have been revealed as the origin of highly improved catalytic activity during ORR.[55-57] Among them, the Fe-N_x moieties have been extensively studied because of their outstanding ORR activity. In order to synthesize the reactive NPMC, the precursors of metal, nitrogen and carbon supports should be properly selected for effectively providing active sites. For example, a significantly enhanced Co/N/C catalyst was synthesized by pyrolysis using tetramethoxyphenyl porphyrin cobalt complex. Zn–air batteries based on the catalyst demonstrated high current density with stable potential retention. In addition, the Fe/Co/N/C catalyst was reported as ORR electrocatalyst for Zn–air batteries.[58] They also showed substantially improved peak power density. In conclusion, the NPMC could be possible alternatives for platinum catalysts because of comparable catalytic activity, stable structure and low cost.

Metal oxides electrocatalysts

To date, the metal oxide materials have been intensively investigated as electrocatalysts for Zn–air batteries. Notably, they are more preferred as bi-functional electrocatalysts than precious metals because of highly stable structure upon cycling and low costs. In this regard, the binary and/or ternary oxides with certain types of structures including perovskite, spinel and other structures have been extensively studied.[59-61] Among them, the manganese oxides have been considered as promising candidates for electrocatalysts because of high oxidation states of the transition metal, stable structure based upon high crystallinity and low costs. In this regard, the commercialized Zn–air batteries have been widely used the manganese oxides as electrocatalysts for ORR. For example, Duracell produced the hearing aid by using the commercialized Zn–air batteries with manganese oxides as electrocatalysts for highly enhanced electrochemical performance.[62] Notably, the Zn–air batteries showed high energy densities of around 400 Wh kg^{-1}. Recently, the bi-functional electrocatalysts with high ORR and OER activity are required for rechargeable Zn–air batteries. However, previously mentioned electrocatalysts exhibited the lower OER activity than that of state-of-the-art RuO_2 and/or IrO_2. Accordingly, perovskite oxides have been studied as bi-functional electrocatalysts for rechargeable Zn–air batteries because of their high bi-functional catalytic activity, high structural and chemical stability upon battery cycling.[63-66] The chemical composition of perovskite oxide structure is ABO_3 consisting of A- and B-site cations and divalent oxygen anions. Notably, the catalytic origin of the perovskite oxides were determined by B-site cations.[67] Suntivich *et al.* demonstrated a volcano-shaped relationship between the e_g orbital filling of B-site cations and the intrinsic catalytic activities of perovskite oxides.[66] They also proposed the metal-oxygen covalency as a secondary factor influencing activity. Jung *et al.* explained that a catalytic activity of perovskite oxides is dependent on the concentration of oxygen vacancies and the valence state of B-site cations via ex situ X-ray absorption near edge structure (XANES) and extended X-ray absorption fine structure (EXAFS) analysis.[65] However, these perovskite oxides showed lower ORR activities than other ORR catalysts. Another limitation of perovskite oxides is the formation of undesirable phases during heat treatment.

1.4 Pyrochlore oxides as bi-functional electrocatalysts

Recently, pyrochlore oxides have been emerged as promising candidates for bi-functional electrocatalysts. The chemical composition of pyrochlore oxides is $A_2B_2O_7$, which consists of A- and B-site cations and divalent oxygen anions.[68] Pyrochlore oxide structure is cubic structure with space group of Fd-3m consisting eight formula units per one unit cell. They could be synthesized by the fluorite structure *via* eliminating one eighth of the anions. Thus, the composition of pyrochlore oxides can be indicated as $A_2B_2O_{7-x}$ with oxygen vacancies.[69] There are two types of divalent oxygen ions in the pyrochlore lattice structure (**Figure 5**). One is the divalent oxygen ions at the 48f site, which are located at tetrahedral sites by bonding with A- and B-site cations. The other is the divalent oxygen ions at 8b sites, which are located at tetrahedral sites by bonding with four of A-site cations. Notably, the coordination contains two of the divalent oxygen ions at 8b sites with very short distance and six of the divalent oxygen ions at 48f sites with much longer distance. The A-site cations are located at 16d sites by coordinating with eight of divalent oxygen ions. Moreover, the B-site cations are located at 16c sites by coordinating with six of divalent oxygen ions.

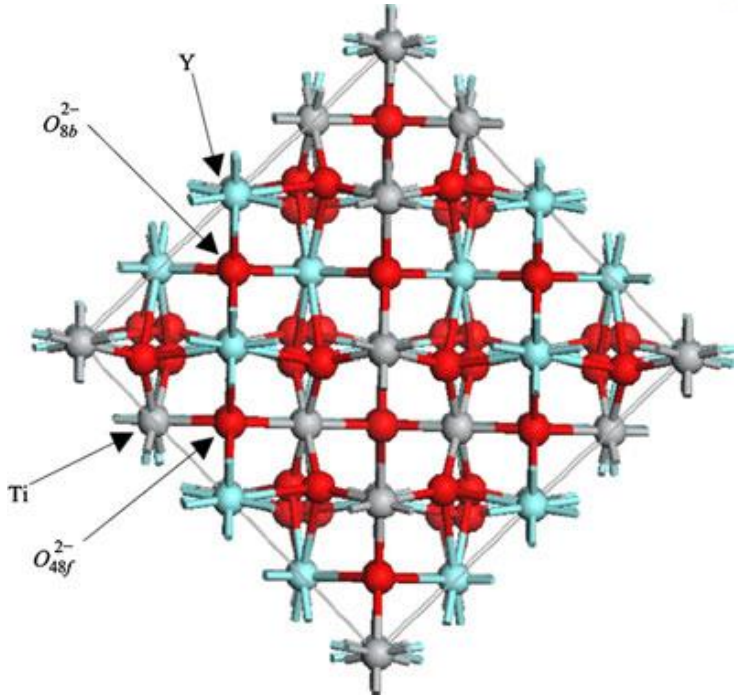

Figure 5. Schematic of a unit cell of the pyrochlore oxide.

This part was reproduced from Brik M. G., Srivastava A. M., Tanaka I. Pyrochlore Structural Chemistry: Predicting the Lattice Constant by the Ionic Radii and Electronegativities of the Constituting Ions. *J. Am. Ceram. Soc.*, **95**, 1454-1460 (2012).

Pyrochlore oxides as electrocatalysts

In general, the chemical composition of pyrochlore oxides is $A_2B_2O_6O'_{1-x}$ consisting of A- and B-site cations and divalent oxygen ions.[70] The A-site cations are rare-earth elements, lead, bismuth and titanium. The B-site cations are transition and post-transition metals including ruthenium, iridium and lead. The pyrochlore oxide structures are consisted of two-sublattice including B_2O_6 and A_2O' structures (**Figure 6**).[71] Notably, the framework of corner-shared BO_6 structures with bent B-O-B bonds effectively provides pathway for high electrical conductivity. In terms of the divalent oxygen ions, the general type oxygen ions (O) bond with the A- and B-site cations, whereas that of the distinct oxygen ions (O') only bond with A-site cations by forming corner-shared A_4O' tetrahedral structures.[72-74] In addition, the d electron wave functions of B-site cations were controlled by the types of A-site cations because of A-B interactions in the pyrochlore oxides. Accordingly, the electronic conductivity of the pyrochlore oxides were determined, and they were classified into two groups; metallic pyrochlore oxides based upon the A-site cations of lead, bismuth and titanium; semiconducting pyrochlore oxides based upon the A-site cations of yttrium, neodymium and praseodymium.[75-77] Interestingly, the pyrochlore oxides contain high oxygen vacancies based upon A_2O' sublattices with stable structure suggesting high structural flexibility.[78] The nonstoichiometric values of x in $A_2B_2O_6O'_{1-x}$ ranged from 0.5 to 1 which corresponds the $A_2B_2O_{6.5}$ and $A_2B_2O_7$, respectively. The types of A- and B-site cations determine the electrocatalytic activity of pyrochlore oxides. In particular, the B-site cations could be doped at A-sites, resulting in the formation of $A_2[B_{2-x}A_x]O_{7-y}$.[79]

The electrocatalytic activities of pyrochlore oxides have been intensively reported as bi-functional electrocatalysts for electrical energy storage systems. They are affected by various factors including the types of A- and B-site cations, oxygen vacancies, surface area and valence states of B-site cations.[80, 81] The effect of actions of pyrochlore oxides on the electrocatalytic activities were revealed by investigating a series of the materials. Among them, the $Pb_2Ir_2O_{7-x}$ and $Pb_xBi_{2-x}Ru_2O_{7-y}$ exhibited high ORR and OER activities with stable structure in alkaline solution.[82] In this context, the iridium based pyrochlore oxides have been studied for investigating the effect of oxygen vacancies on the catalytic performance. Kortenaar *et al.* revealed the origin of enhancement of ORR and OER activities of $Pb_2[Pb_xIr_{2-x}]O_{7-x}$ and Nd_3IrO_7 based upon the oxygen deficiency.[81] In addition, Prakash *et al.* demonstrated the effect of doping of A-site cations at B-site and corresponding changes of specific surface area of $Pb_2Ru_2O_{7-x}$.[72] For example, partially doped $Pb_2[Pb_{0.33}Ru_{1.67}]O_{6.5}$ and $Pb_2[Pb_{0.2}Ru_{1.8}]O_{6.5}$ showed higher catalytic activity during ORR than that of stoichiometric $Pb_2Ru_2O_{6.5}$. This result could be ascribed to the increase of specific surface area of the catalysts based upon the values of 55, 44 and 35 $m^2\ g^{-1}$ for $Pb_2[Pb_{0.33}Ru_{1.67}]O_{6.5}$, $Pb_2[Pb_{0.2}Ru_{1.8}]O_{6.5}$ and $Pb_2[Pb_{0.33}Ru_{1.67}]O_{6.5}$, respectively.

Recently, Nazar group reported the pyrochlore oxides as bi-functional electrocatalysts for Li–air batteries.[78] They synthesized the $Pb_2[Ru_{1.73}Pb_{0.27}]O_{6.5}$ and $Bi_2[Ru_{1.53}Bi_{0.47}]O_{7-x}$ by using a chemical precipitation method with high surface area, high oxygen nonstoichimetry and abundant defects. They showed significantly enhanced discharge capacities and lowered anodic overpotentials based upon the high active sites. Moreover, the prepared electrocatalysts effectively transfer the electrons with mixed oxidation states. Notably, the small amount of gold additives derived substantial improvement of electrochemical performance of the pyrochlore oxides. In order to further enhance the catalytic activity of pyrochlore oxides, they reported the mesoporous $Pb_2[Ru_{1.6}Pb_{0.44}]O_{6.5}$ with metallic conduction.[83] It was synthesized by using liquid-crystal self-assembly followed *via* chemical oxidation (**Figure 7**a). **Figure 7**b shows the disordered mesoporous structure of the pyrochlore oxides. The $Pb_2[Ru_{1.6}Pb_{0.44}]O_{6.5}$ with surface area of 155 $m^2\ g^{-1}$ demonstrated higher electrochemical performance upon battery cycling than that of the $Pb_2[Ru_{1.7}Pb_{0.3}]O_{6.5}$ with surface area of 66 $m^2\ g^{-1}$. These results suggest that the higher concentration of oxygen defects on the surface of pyrochlore oxides could improve the ORR and OER activities.

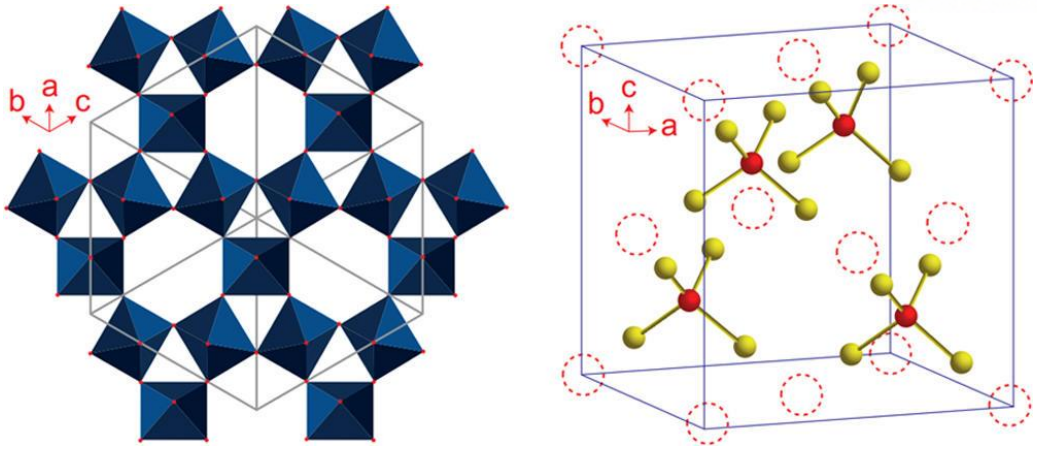

Figure 6. Structure of the oxygen nonstoichiometric pyrochlore $A_2B_2O_{7-x}$ (x = 0.5; A = Pb, Bi; B = Ru), demonstrating oxygen vacancies and electron conduction paths *via* BO_6 octahedral structure that provide metallic conductivity.

This part was reproduced from Oh S. H., Black R., Pomerantseva E., Lee J. H., Nazar L. F. Synthesis of a metallic mesoporous pyrochlore as a catalyst for lithium-O_2 batteries. *Nat. Chem.*, **4**, 1004-10 (2012).

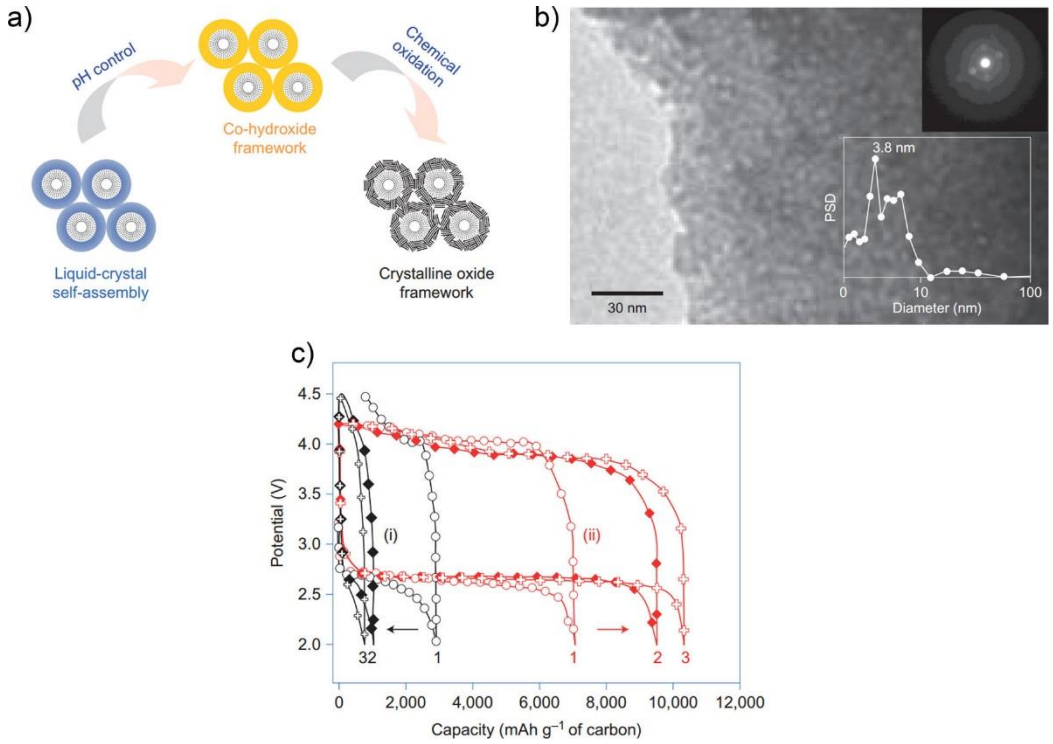

Figure 7. (a) Schematic representation for the synthetic method of the mesoporous lead ruthenium pyrochlore oxide. (b) TEM image of the mesoporous lead ruthenium pyrochlore oxide. The inset figure indicates the SAED pattern of the nanocrystalline walls. The inset graph presents the pore size distribution (PSD) result of the surfactant-free mesoporous lead ruthenium pyrochlore oxide. (c) The first three cycles of discharge-charge curves for carbon in $LiPF_6$/TEGDME (i) and the mesoporous lead ruthenium pyrochlore oxide (ii) at a current rate of 70 mA g^{-1}.

This part was reproduced from Oh S. H., Black R., Pomerantseva E., Lee J. H., Nazar L. F. Synthesis of a metallic mesoporous pyrochlore as a catalyst for lithium-O_2 batteries. *Nat. Chem.*, **4**, 1004-10 (2012).

1.5 Scope and organization of this dissertation

The objective of this dissertation is the study of pyrochlore oxides as electrocatalysts for Zn–air batteries and the design of novel flexible batteries.

The chapters are categorized as follows:

Chapter 2 reports the cable-type flexible Zn–air batteries based on the non-precious metal catalysts and freestanding gel polymer electrolyte, providing highly enhanced electrochemical performance during bending tests.

Chapter 3 presents the highly pure single crystalline pyrochlore nanoparticles with metallic conduction ($Pb_2Ru_2O_{6.5}$) as an efficient electrocatalyst for rechargeable Zn–air batteries. The origin of catalytic activity of pyrochlore oxides was revealed.

Chapter 4 investigates the yttrium ruthenate nanoparticles ($Y_2[Ru_{2-x}Y_x]O_{7-y}$) with pyrochlore structure as highly active bi-functional oxygen electrocatalysts for Zn–air batteries, providing insight into the roles of A- and B-site cations in pyrochlore oxides during ORR and OER.

Chapter 5 demonstrates the polyhedral bismuth ruthenate pyrochlore ($Bi_2Ru_2O_7$) as a bi-functional oxygen electrocatalyst for Zn–air batteries. The facets evolution of the prepared catalyst during synthesis was revealed by *in situ* TEM analysis.

Chapter 2

All-solid-state cable-type flexible Zn–air batteries

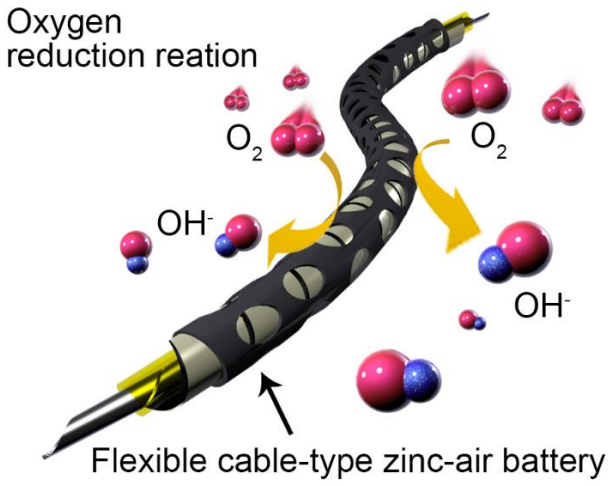

For the flexible design of cable-type flexible Zn–air batteries (ZAB), we first developed the flexible design of the ZAB with a reliable high-performance. To achieve the flexible system, we fabricated a freestanding gelatin based gel polymer electrolyte (GGPE) with 0.1 M KOH, showing an ionic conductivity of 3.1×10^{-3} S cm^{-1} at 24 °C. In addition, the non-precious metal catalyst derived from silk fibroin was synthesized to enhance oxygen reduction reaction (ORR) rate in the ZAB. Significantly, this novel cable-type ZAB is designed to enable an outstanding flexible and bendable property with a stable discharge curve of 0.92 V of voltage plateau, of which value is identical to non-bending condition.

This chapter has been published.

Park J., Park M., Nam G., Lee J., Cho J.* All-Solid-State Cable-Type Flexible Zinc-Air Battery, *Adv. Mater.*, 27, 1396-1401 (2015).

2.1 Introduction

Wearable and portable electronic devices have received the spotlight for practical applications such as smart electronics and flexible devices.[84] To realize this concept, the flexibility of each component in such devices has been considered as a key issue as well as their electrochemical ability. Among them, the battery system is regarded as an essential component for the energy storage.[85-87] For example, in lithium-ion batteries (LIBs) fields, various types of flexible designs such as a cable, stretchable and bendable type have been reported by many research groups.[86, 88-90] Especially, Peng and co-workers have pioneered the direction on one-dimensional batteries and supercapacitors based on cable-type structures.[91-97] However, a flexible design for Zn–air batteries has not yet explored.

The Zn–air battery (ZAB) has been considered as an inexpensive, safe and eco-friendly system due to the non-reactive zinc metal and aqueous solvent.[5, 6] Furthermore, the ZAB has a high specific energy density with 1084 Wh kg^{-1}.[4] However, the conventional stack-type ZAB has a design rigidity in order to apply for the wearable electronic devices compared to previously reported flexible LIBs. Also, coin-type ZAB is commercialized for hearing aids only. Achieving a stable electrochemical performance during the repetitive external strain force, each component of the battery should satisfy the flexibility with electrochemical stability in the cathode, anode, separator and electrolyte. Especially, a typical liquid electrolyte is not appropriate for a flexible system due to its evaporation and leakage problems. To extend the application range of the ZAB, a novel design is required to replace the conventional stack-type battery system.

An important component of the ZAB for the flexible design is a solid type electrolyte. As for the conventional ZAB system, 6 M KOH aqueous solution is widely used as an optimized electrolyte due to its high ionic conductivity and low viscosity.[98] To obtain the solid-type electrolyte, the KOH-based gel polymer electrolyte (GPE) has been reported by using various polymers, such as poly(vinyl alcohol) (PVA), poly(ethylene glycol) (PEO), poly(vinylpyrrolidone) (PVP) and as gelling agents, which have ionic conductivities of ca. 10^{-3}–10^{-4} S cm^{-1} with a high concentration of KOH with >10 wt%.[99-104] Typically, the GPE presents a relatively lower ionic conductivity than liquid counterparts. However, to obtain flexibility, there is a trade-off between ionic conductivity and electrochemical performance. Thus, our goal in the electrolyte part is the development of new highly conductive GPE with a minimum use of KOH to ensure leak-free solid-type behavior.

Here, we first fabricated all-solid-state cable-type flexible ZAB with spiral zinc anode with a freestanding gel polymer electrolyte (GPE) and air electrode with nonprecious metal catalyst (NPMC) to replace platinum (Pt) with disadvantages of its high cost, low stability and poor kinetics.[12, 41, 105] Use of an electrocatalyst is the most effective method to improve the electrochemical performance of an air cathode in metal–air batteries.[106-108] Importantly, the gelatin was used as gelling agent that contains

KOH solution with abundant OH^- ions, standing on its superb gelation ability and high ionic conductivity for alkaline GPE.[109-111] This alkaline GPE based on gelatin (GGPE) has never been reported for the ZAB. Although the GGPE is based on a lower concentration of 0.1 M (0.56 wt%) KOH than previously reported KOH-based GPEs, it has comparable and even higher ionic conductivity. In addition, an NPMC based on silk fibroin for metal/nitrogen/carbon (M/N/C) catalysts with high catalytic activity for the ORR was synthesized to enhance ORR in the cable-type flexible ZAB.

2.2 Experimental detail

Catalyst Preparation: 0.05 g of iron acetylacetonate (Aldrich) as an iron precursor was fully dissolved in 50 mL of distilled water at room temperature for about 20 min. Iron acetylacetonate was completely dissolved in water and 0.05 g of commercial Ketjenblack EC-600JD (KB) was added into the solution with stirring uniform dispersion of KB. 0.3 g of commercial silk fibroin into the dispersed solution was added and stirred for 12 h. Finally, the obtained precursor was pyrolyzed under Ar atmosphere (flow rate of 50 mL min^{-1}) at 800, 900 and 1000 °C for 3 h.

Preparation of Catalyst Ink and the Working electrode: The catalyst ink was prepared with a mixture of 10 mg of the Fe/N/C catalyst powder, 100 μL of 0.05% Nafion (Aldrich) solution and 400 μL of ethanol. Briefly, the desired catalyst ink was prepared by ultrasonically mixing in distilled water for at least 1 h to form homogeneous catalysts ink. A portion of 5 μL of the ink was loaded on the surface of the working electrode, resulting in 0.796 mg_{cat} cm^{-2}. For the 79.6 μg_{Pt} cm^{-2} catalysts, 10 mg of 20 wt% Pt on Vulcan XC 72 (Premetek Co.) were dissolved in 200 μL of 0.05% Nafion (Aldrich) solution and 800 μL of ethanol. This catalyst ink was ultrasonically mixed at least 1 h to get a homogeneous catalyst ink. Then, 5 μL of ink was loaded on the surface of the working electrode, resulting in 0.398 $mg_{(20\ wt\%\ Pt/C)}$ cm^{-2} , corresponding to 79.6 μg_{Pt} cm^{-2} with the same methods as those mentioned above.

Electrochemical Measurements: Rotating ring disk electrode (RRDE) (ALS Co., Ltd) experiments were carried out using the Fe/N/C series catalyst film (deposited on glassy carbon electrode) as the working electrode in 0.1 M KOH alkaline electrolyte with saturated O_2. Hg/HgO and Pt wire are used as reference and counter electrodes, respectively. Electrochemical characterization was conducted using bipotentiostat (IviumStat). A 10 mV s^{-1} scan rate was swept from 0.2 to −0.7 V and a sufficient ring potential of 0.4 V was biased to oxidize intermediate during ORR. The collection efficiency (N) was determined under Ar atmosphere using 10 mM $K_3[Fe(CN)_6]$, which is around 0.41. This is similar value of theoretical value which is 0.42. The peroxide yields (H_2O^-) and number of transferred electrons (n) were calculated using the equations below:

$$H_2O^-(\%) = 100\frac{2I_r/N}{I_d+I_r/N} \quad (1)$$

$$\mathrm{n} = 4\frac{I_d}{I_d+I_r/N} \quad (2)$$

Stack-Type Zn–air full cell tests: For a stack-type full cell test of our catalysts, we prepared 0.75 g of zinc granular as an anode and 200 μL of 6 M KOH was used for the electrolyte. A nylon membrane was used for the separator. The air cathode was prepared by uniformly casting ink on the prepared gas

diffusion layer (the catalyst ink formulation: 10 mg of catalyst, 100 μL of 5 wt% of Nafion in mixture of lower aliphatic alcohols and H_2O (Aldrich) and 400 L of ethanol). An assembled full-cell was tested at the discharge current densities of 25 mA cm^{-2}, 50 mA cm^{-2} and 100 mA cm^{-2}. The gas diffusion layer (GDL) was prepared from a mixture of activated charcoal (Darco G-60A, Aldrich) and PTFE binder (60 wt% PTFE emulsion in water, Sigma–Aldrich) at a weight ratio of 7:3 with about 450 μm of thickness to ensure proper gas distribution and sufficient current collection. This prepared GDL was used as the reference for comparison to confirm the enhanced performance of catalyzed air electrode in polarization curve of the Zn–air battery.

Preparation of Gel Polymer Electrolyte: 10 g of commercial gelatin powder (Geltech Co., Ltd., Korea) were fully dissolved in 25 mL of 0.1 M KOH solution at 60 °C under magnetic stirring for about 30 min.

Preparation of Cable-Type Flexible Zn–Air Battery: A zinc metal plate was used as the anode and its width and length can be controllable. In our case, we used an as-received zinc plate with a width of 3 mm and a length of 10 cm and the diameter and length of the cable-type flexible Zn–air battery were 8 mm and 7 cm, respectively. First, the zinc plate was wound on s stainless-steel rod; the rod was removed and then the wound zinc plate was placed in a cellophane template. Here, we could control the battery dimension with the cellophane template size. For this study, we used a cellophane template that had a diameter of 8 mm and a length of 7 cm. The next step was to fill it by the prepared gel polymer electrolyte solution. To gelate the prepared solution, the solution was cooled to 4 °C in a refrigerator over 1 h and then the air electrode (MEET Company) with a 5 mm width and a 10 cm height was wound. Finally, the punched heat contraction rubber cable with holes of 6 mm diameter and 12 mm cable diameter and a 10 cm cable length, was used. This rubber has a shrinkable property when applying external heat to pack the electrode assembly.

Mechanical Bending Test: The mechanical bending test was carried out by bending the length of the cable-type ZAB. At the beginning of discharge, the length was 7 cm, followed by decreasing its length by continuous bending to 5 and 3 cm, respectively during 20 min. After this, the bent ZAB returned to the original length of 7 cm. The discharge current density was 0.1 mA cm^{-2}. The discharge current density was 0.1 mA cm^{-2}.

Physical Characterization: The material morphology was examined using SEM (S-4800m Hitachi) and high-resolution transmission electron microscopy (HR-TEM) (JEOL JEM-2100F) operating at 200 kV. Powder analysis was performed using an X-ray diffractometer (XRD) (D/Max2000, Rigaku). The oxidation state of the elements was analyzed using X-ray photoelectron spectroscopy (XPS) (Thermo Scientific Kα spectrometer, 1486.6 eV).

2.3 Results and discussion

Figure 8 is a schematic representation of the cable-type flexible ZAB composed of a spiral zinc anode, freestanding GGPE and electrocatalyst loaded air cathode. **Figure 8**a shows a fabrication process of the cable-type flexible ZAB assembly. First, the zinc metal plate was coiled on the surrounding stainless steel rod, followed by removing the rod. Then, the spiral zinc metal was located at the center of cellophane template. Controlling battery diameter is important for portable electronics. Accordingly, a small diameter may be better to apply for miniaturized electronic devices. However, we selected the battery's diameter as 8 mm to maximize electrochemical performance while maintaining the flexibility. By controlling the cellophane template size, we can decrease its diameter from 8 to 4 mm or much smaller. However, there is a trade-off between diameter and electrochemical performance. After the step, the spiral zinc is coated to the GGPE, the electrolyte solution consisting of the gelatin and 0.1 M KOH poured into the cellophane template (**Figure 8**b). In order to obtain the freestanding GGPE, the zinc rod immersed in the electrolyte solution was kept in refrigerator at 4 °C for 1 h. Next, the electrocatalyst loaded air electrode was winded on the surrounding the GGPE. Importantly, to enhance the surface contact between electrodes and GGPE, we used the punched heat-contraction rubber cable that has shrinkable property when applied external heat to pack the electrode assembly. The punched hole in the final product acts as an air pathway. **Figure 8**b shows the schematic diagram of the GGPE coating process on the surrounding spiral zinc anode. Gelatin is composed of three chains as triple helix structure.[112] When gelatin is powder phase, the chains are twisted as triple helix. Dissolving it in solution, the chains are unfolded by heating process. At a high concentration of alkaline solution, these chains are interrupted to fold as a triple helix.[113] In other words, such as 6 and 1 M of KOH solution, the gelation of gelatin was interrupted by the lack of gelation material. Moreover, its concentration was decreased to 0.25 M and we could not get the freestanding gel electrolyte. Accordingly, we optimized the concentration of KOH solution to 0.1 M (**Table 1**).

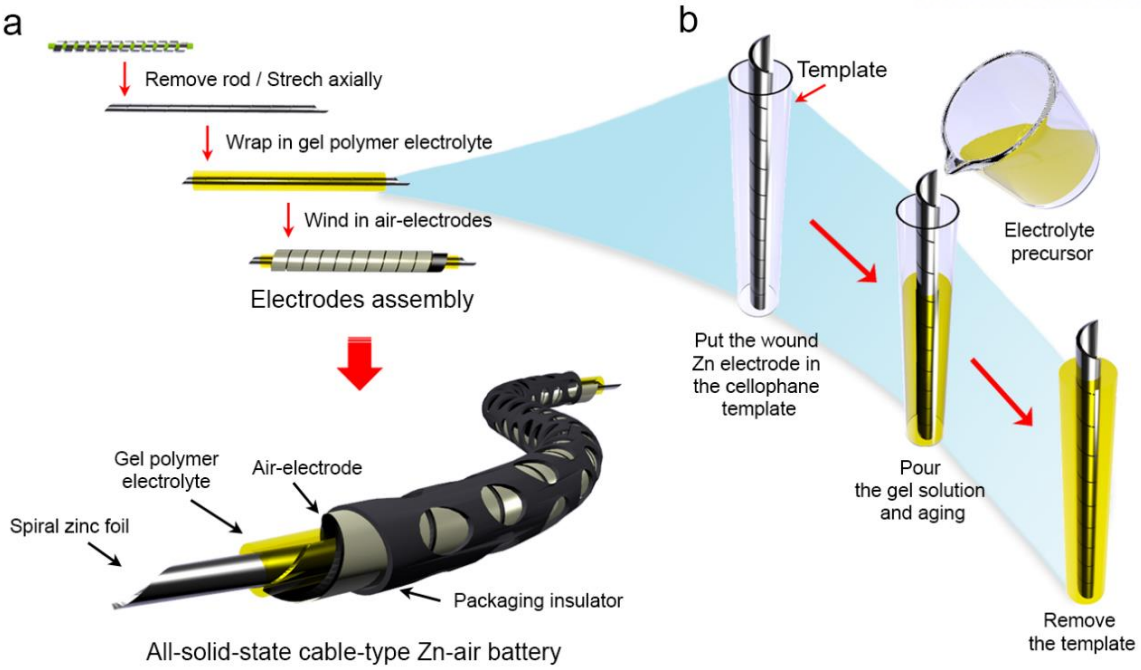

Figure 8. (a) Schematic diagram of the all-solid-state cable-type flexible Zn–air battery assembly and (b) coating process of gelatin-based gel polymer electrolyte (GGPE) and 0.1 M KOH on the surrounding spiral zinc anode.

Table 1. Gelation of gelatin with various concentration of KOH solution.

	6 M KOH	1 M KOH	0.25 M KOH	0.1 M KOH
Gelation	X	X	X	O
Electrical performance	•	•	•	O

In high concentration of KOH with gelatin, gelation of gelatin is hampered. In other words, it is hard to synthesize solid-type electrolyte based on high concentration with high concentration KOH such as 6, 1 and 0.25 M (**Table 1**). As the results, the highest concentration of KOH for a freestanding GGPE was 0.1 M.

The oxygen reduction reaction (ORR) is a rate determining step (RDS) because of sluggish reaction in the air cathode. To enhance the cell performance of the cable-type flexible ZAB, we used the silk fibroin as a major precursor for the electrocatalyst. Silk cocoon consists of two main proteins such as fibroin and sericin.[114] Fibroin, composed of amino acids such as glycine, alanine and serine, is located at the center of silk cocoon. Sericin (silk gum) is also coated on fibroin with sticky characteristics. Importantly, the fibroin can act as a precursor for nitrogen and carbon atom. The iron acetylacetonate was used for transition metal precursor as an iron source. In addition, to increase the surface area and electron conductivity of carbonized silk fibroin, a small amount of ketjenblack (KB) was added to increase the active sites for ORR reaction.[115] Briefly, the iron precursor and KB nanoparticles were homogeneously coated on the silk fibroin surface by stirring process as self-adsorption. After drying at oven, the obtained product was pyrolyzed under Ar atmosphere at optimized temperature as 900 °C during 3 h for carbonization of silk fibroin (**Figure 9**). After pyrolysis, the Fe/N/C catalyst with high catalytic activity for ORR was successfully synthesized.

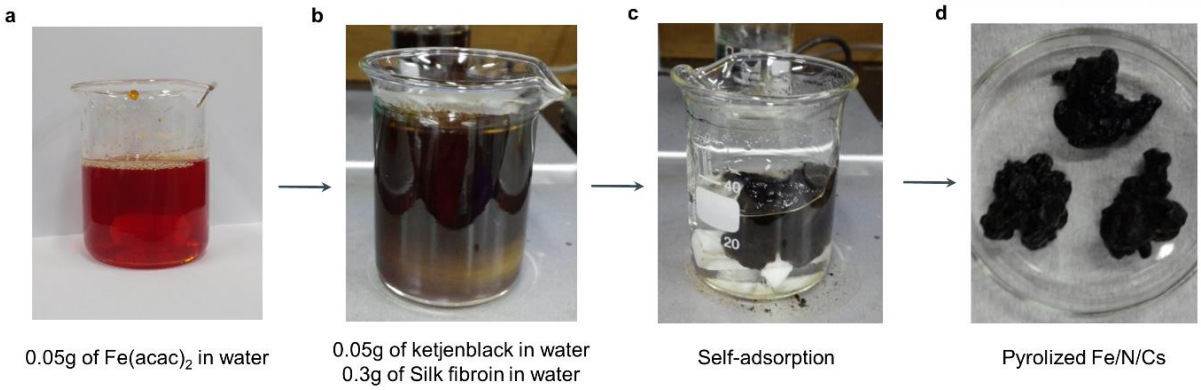

Figure 9. Pictures for synthetic process of Fe/N/C-series. (a) Iron solution, (b) Homogeneous ketjenblack/iron solution with silk, (c) Self-adsorption of ketjenblack and iron source on surface of silk after stirring, (d) After pyrolysis process at 900 °C.

Figure 10 shows the XRD data and TEM image of Fe/N/C composite pyrolyzed at 900 °C (labeled as Fe/N/C-900). As presented in **Figure 10**a, there are two broad peaks at 26° and 43°, corresponding to (002) and (100) planes, respectively, showing the formation of crystalline structures with a partially disordered moiety. Using the diffraction data for α-Fe (JCPDS No. 87–0722) and Fe_3C (JCPDS No. 89–2867), the metallic Fe and Fe_3C phases were confirmed. The SEM image also showed that the Fe_3C/Fe with a rod shape and KB nanoparticles were homogeneously distributed on carbon backbone (**Figure 12**). TEM image of the composite also showed same phenomena to the above (**Figure 2**b). Fast Fourier transform (FFT) image of Fe/N/C-900 indicates the mixed phases both amorphous and crystalline structure derived from carbon and Fe_3C/Fe, respectively. The high-resolution transmission electron microscopy (HR-TEM) image presents that the Fe_3C/Fe nanoparticles with a diameter of ca. 10 nm is covered by six to eight graphitic layers with a 3 nm thick (**Figure 10**c). The crystallinity of the Fe_3C/Fe nanoparticles was also confirmed from the FFT image (**Figure 10**d). For detailed analysis of surface chemical composition of the Fe/N/C-900 sample, the XPS survey was presented in **Figure 13** and **Table 2**. This catalyst shows improved ORR activity due to nitrogen derived active sites, such as pyridinic (≈398.5 eV) and graphitic nitrogen (≈401.3 eV). Bulk composition and surface composition of Fe/N/C-900 is analyzed by XPS. Surface composition is important for ORR activity because of its surface reaction. To select the optimized catalyst, we used the electrochemical analysis based on rotation ring disk electrode (RRDE) method. As shown in **Figures 14 and 15**, the electrochemical properties of the prepared Fe/N/C samples synthesized at various temperatures were compared to Pt/C catalyst. Consequentially, we selected the Fe/N/C-900 catalyst as an optimized nonprecious electrocatalyst which has proper combination of pyridinic and graphitic nitrogen contents. This optimized catalyst demonstrated comparable electrochemical activity to Pt/C. In consequence, our new catalyst can be used in all-solid-state cable type flexible ZAB.

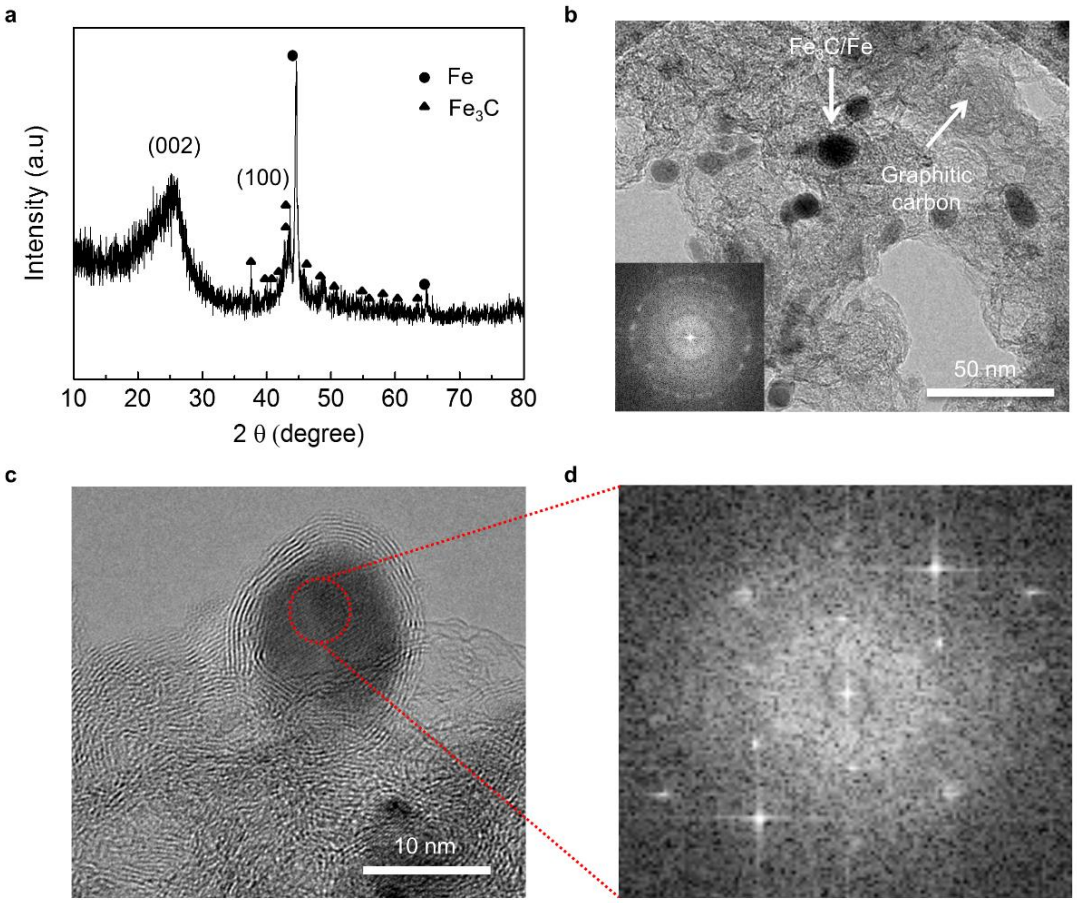

Figure 10. (a) XRD data of Fe/N/C-900 electrocatalyst. (b) HR-TEM image of iron nanoparticle with amorphous carbon. (c) TEM image of iron nanoparticle encapsulated in graphitic sheets, with (d) FFT image.

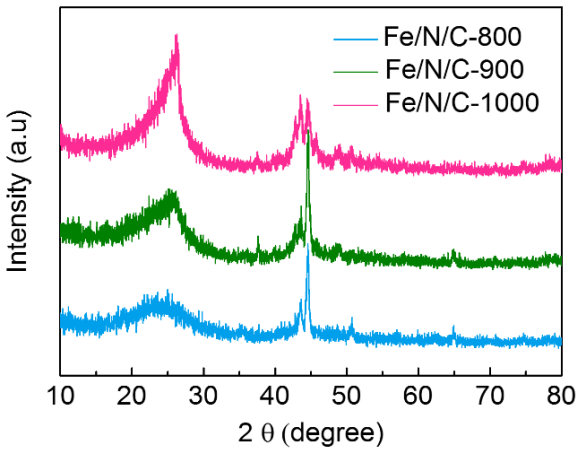

Figure 11. XRD patterns of Fe/N/C samples.

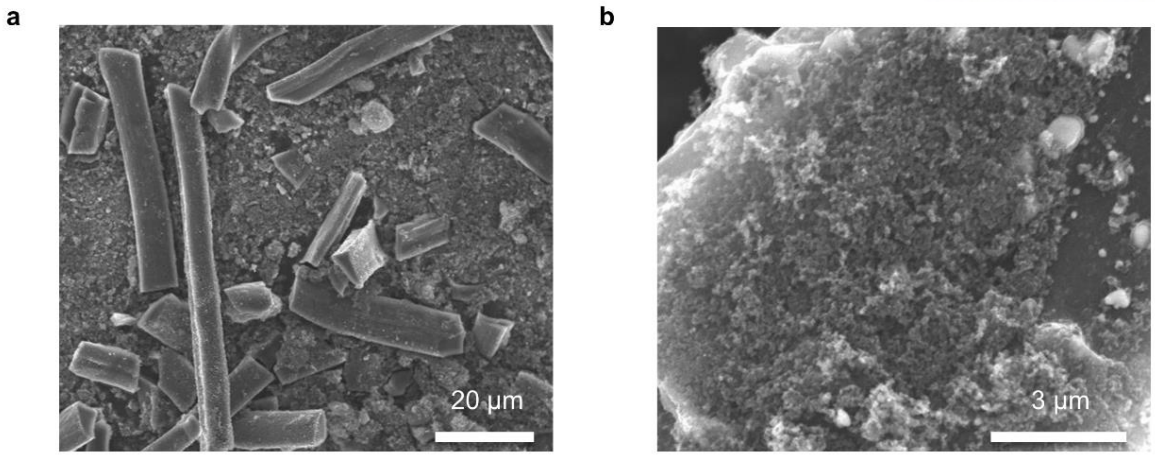

Figure 12. SEM image of Fe/N/C-900 catalyst (a) in low resolution and (b) high resolution.

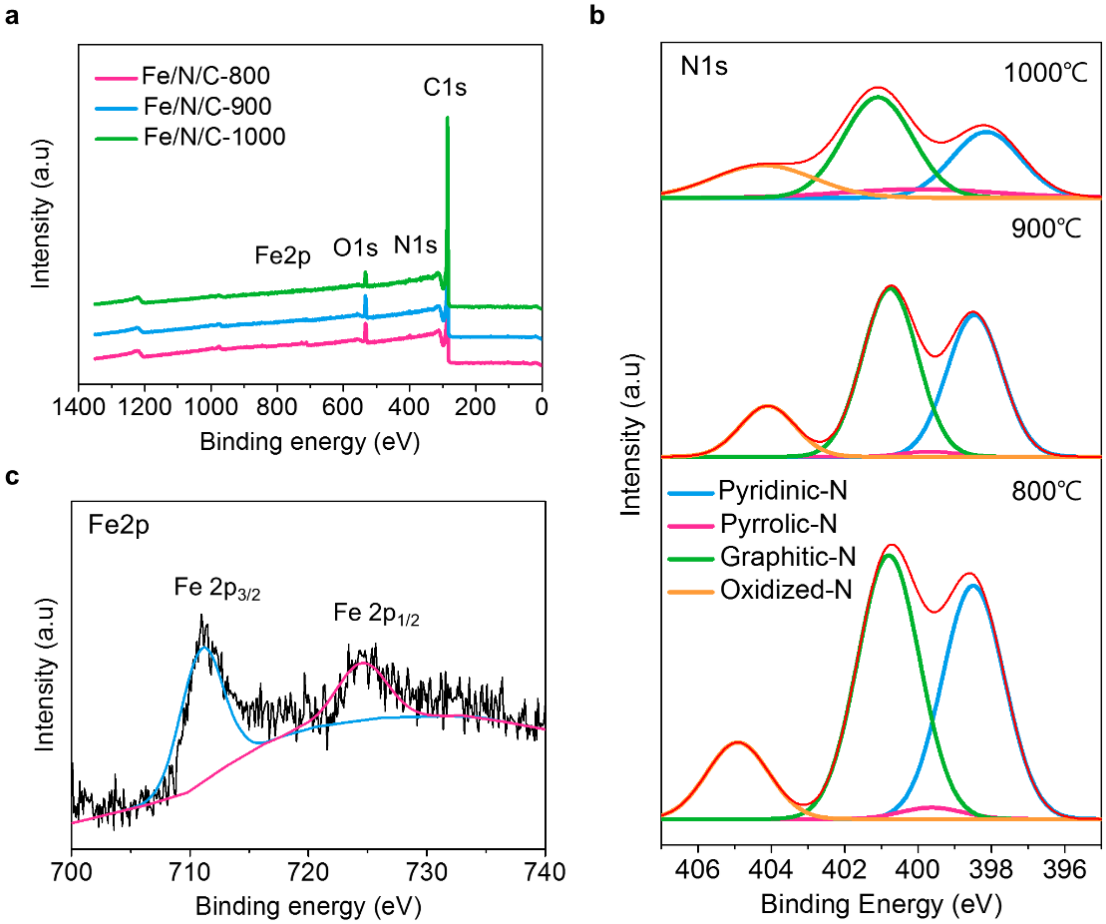

Figure 13. (a) XPS survey and (b) high resolution N 1s of Fe/N/C samples pyrolyzed at different temperatures (Fe/N/C-800, 900 and 1000 °C). (c) XPS high resolution Fe 2p.

The bulk and surface compositions of Fe/N/C-900 were analyzed by XPS. The surface composition is important for ORR activity because of its surface reaction. The XPS spectra of carbon, nitrogen, oxygen and iron of Fe/N/C-900 are shown in **Figure 13**a. In high resolution spectra of N 1s (**Figure 13**b), there are four types of nitrogen such as pyridinic (≈398.5 eV), pyrrolic (≈400.3 eV), graphitic (≈401.3 eV) and oxidized N (≈404 eV). As increasing pyrolyzed temperature, there is increasing tendency of the ratio of graphitic N to pyridinic N from 1.13 to 1.52. In addition, relative nitrogen contents compare with other elements are decreased from 1.6 to 1.36 wt% as increasing pyrolyzed temperature from 800 to 1000 °C (**Table 3**). These results have been already reported by many researchers.[111] Furthermore, in case of Fe 2p core level spectra, Fe $2p_{3/2}$ is appeared at 711 eV. According to the fact, iron is successfully existed in Fe/N/Cs catalyst. Low relative surface contents of nitrogen and iron are caused by existence of few carbon layers around Fe_3C nanoparticles (**Figure 13**c).

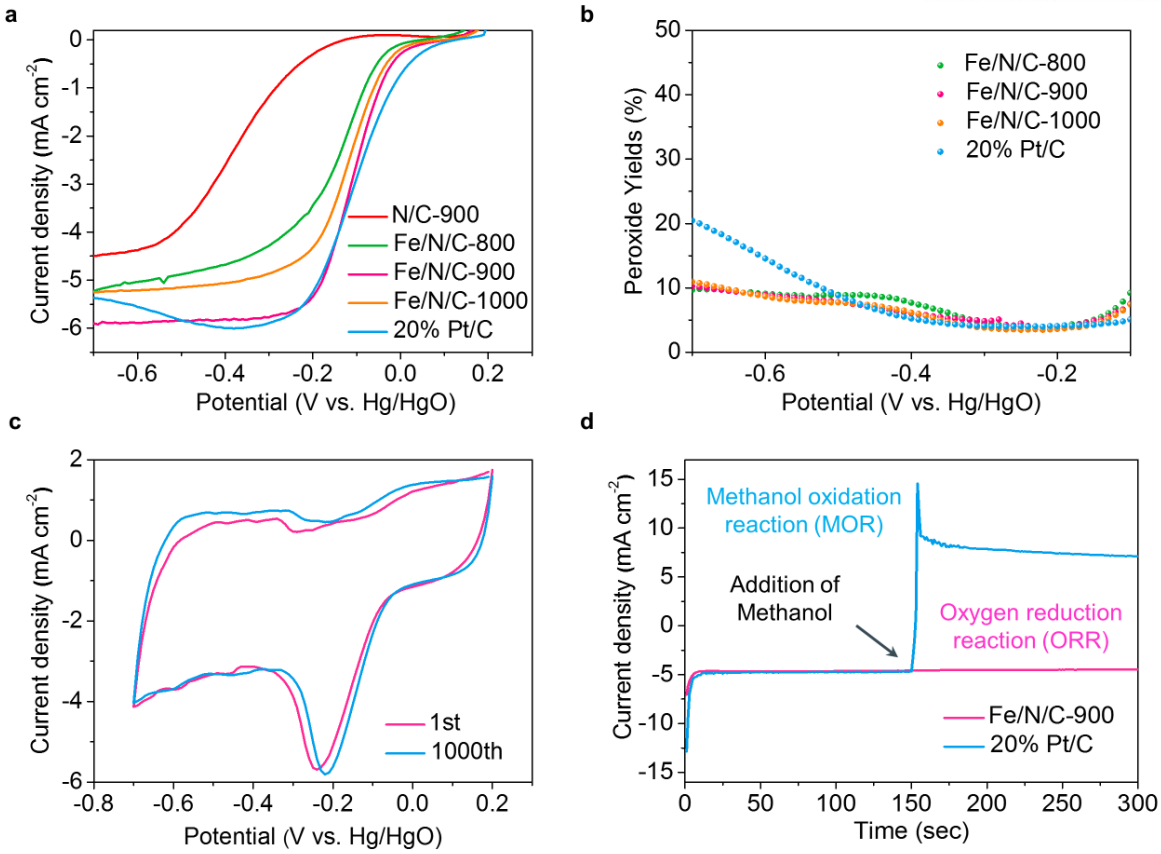

Figure 14. Electrochemical characterization for Fe/N/Cs catalysts. (a) Steady-state RRDE experiments of Fe/N/Cs (0.796 mg_{cat} cm^{-2}) and 20% Pt/C (79.6 μg cm^{-2}) in O_2-saturated 0.1 M KOH at 1600 rpm and 10 mV s^{-1} scan rate. (b) Calculated peroxide yields (H_2O-) of Fe/N/Cs samples. (c) CV curves at initial and after 1000 cycles at 50 mV s^{-1} scan rate in O_2-saturated 0.1 M KOH solution. (d) Chronoamperometric response of 10 % (w/w) methanol of Fe/N/C-900 and 20 % Pt/C in O_2-saturated 0.1M KOH solution at −0.2 V (vs. Hg/HgO) at 1600 rpm and 10 mV s^{-1} scan rate.

The ORR activities of Fe/N/C series and platinum through rotation ring disk electrode (RRDE) is shown in **Figure 14** with linear sweep voltammetry (LSV) measurements in O_2-satruated 0.1 M KOH at 1600 rpm and 10 mV s^{-1} scan rate. A current density of the pyrolyzed carbon backbone at 900 °C, which derived from silk fibroin (N/C-900), Fe/N/C series with adding iron and ketjenblack and 20 % Pt/C are shown in **Figure 14**a. The N/C-900 indicates onset potential as −0.1 V and limiting current density as −4.5 mA cm^{-2}. From the fact, carbon backbone has possibility of enhancing ORR activity. Through the influence of increasing conductivity due to add carbon material (KB) and Fe-N_4 ORR active sites due to add iron, the Fe/N/C series show highly improved onset potential, half-wave potential ($E_{1/2}$) and limiting current density. Particularly, the Fe/N/C-900 shows comparable ORR activity with platinum with onset potential as near 0 V and limiting current density as −5.9 mA cm^{-2}. Furthermore,

hydrogen peroxide yield of Fe/N/C-900 which means number of two-electrons in ORR has low as similar as platinum (**Figure 14**b). **Figure 14**c demonstrates cyclic voltammetry curves of Fe/N/C-900 even after 1000 cycles. The difference between looped curves of 1st and 1000th is only 7.4 % which means great durability of Fe/N/C-900. The significantly enhanced durability is also supported by chronoamperometric (i-t) response in **Figure 15**. As can be seen, the continuous ORR at −0.2 V (vs Hg/HgO) showed that a remaining relative current density for Fe/N/C-900 (87.46% at 20000 s) is higher than that of platinum electrodes (81.64 % at 20000 s). Furthermore, in a methanol tolerance test, the current response of Fe/N/C-900 is insensitive to the added methanol (**Figure 14**d). The other way, platinum catalyst showed a sharp fluctuation upon the addition of methanol. Therefore, Fe/N/C-900 can be applied for direct methanol fuel cell (DMFC) as well as efficient and durable cathode catalysts for Zn–air battery.

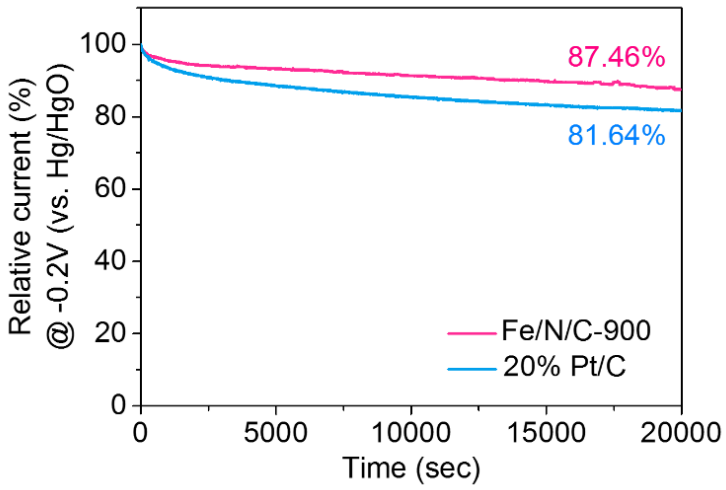

Figure 15. (a) Chronoamperometric response of Fe/N/C-900 and 20 % Pt/C in O_2-saturated 0.1 M KOH solution at −0.2 V (vs. Hg/HgO) at 1600 rpm.

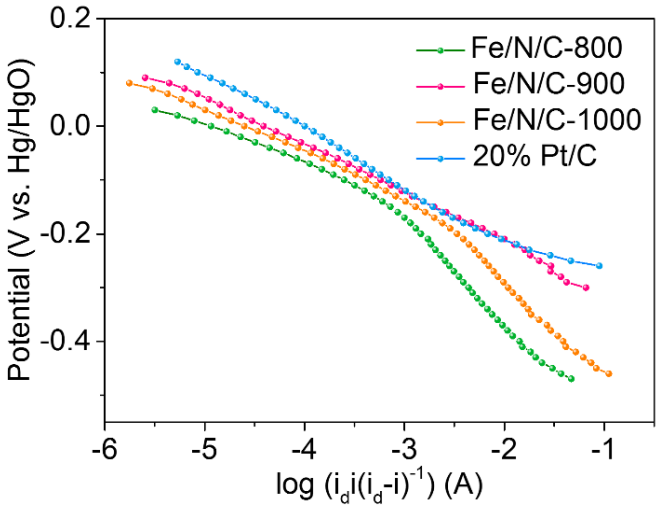

Figure 16. Tafel plots of log I_k (A) vs. E (V) for the ORR on Fe/N/Cs electrodes in an O_2-saturated 0.1 M KOH solution at a rotation rate of 1600 rpm. Limiting current density obtained at potential −0.5 V vs. Hg/HgO was used to calculate I_k using the equations, $i_k = i_L \cdot i/(i_L - i)$.

In order to explore the kinetic reaction of ORR, the mass-transfer corrected Tafel plots of log I_k(A) vs. the electrode potential E for the ORR on the Fe/N/Cs and platinum catalysts in an O_2-satureated 0.1 M KOH solution (**Figure 16**). There is no large difference of the plot shape between Fe/N/Cs and platinum. At low overpotential region, its slope is around 60 mV dec^{-1} and at high overpotential region, it is around 120 mV dec^{-1}, corresponding to the values of Damjanovic and co-workers.[116]

Table 2. Atomic percent of various samples by XPS.

	Elemental composition by XPS (At. %)			
Sample	C 1s	N 1s	O 1s	Fe 2p
Fe/N/C-800	92.54	1.60	5.39	0.48
Fe/N/C-900	92.46	1.59	5.43	0.53
Fe/N/C-1000	94.49	1.36	3.82	0.33

Table 3. Tafel slopes (mV dec^{-1}) for Fe/N/Cs at different voltages.

Catalysts	**Low η**	**High η**
Fe/N/C-800	58.6	119
Fe/N/C -900	67	116
Fe/N/C -1000	67	122

To achieve the all-solid-state flexible ZAB, we assessed the ionic conductivity of the GGPE with OH^- ions. **Figure 17**a shows the image of the optimized freestanding GGPE and its ionic conductivity was obtained from AC impedance spectra. The ionic conductivity of gel polymer electrolyte can be calculated by ohmic resistance, which can be get from AC impedance spectra. **Figure 17**b shows the bulk resistance of GGPE as 32 Ω. Moreover, we used gel polymer electrolyte which of thickness is 0.2 cm and 2.01cm^{-2}. On the basis of the equation of ionic conductivity, we can get the conductivity of 0.1 M KOH based GGPE as 3.01×10^{-3} S cm^{-1}. **Figure 17**c demonstrates the electrochemical impedance spectra of the stack-type ZAB based on liquid electrolyte and GGPE, respectively. Based on Nyquist plot data, both solution resistance (R_s) and charge transfer (R_{ct}) resistance of our GGPE sample are higher than those of the liquid electrolyte. However, such a high conductivity of the GGPE in spite of its solid-like nature led to reasonably high discharge times at 0.1, 0.5 and 1 mA cm^{-2} in the stack-type ZAB (**Figure 17**d).

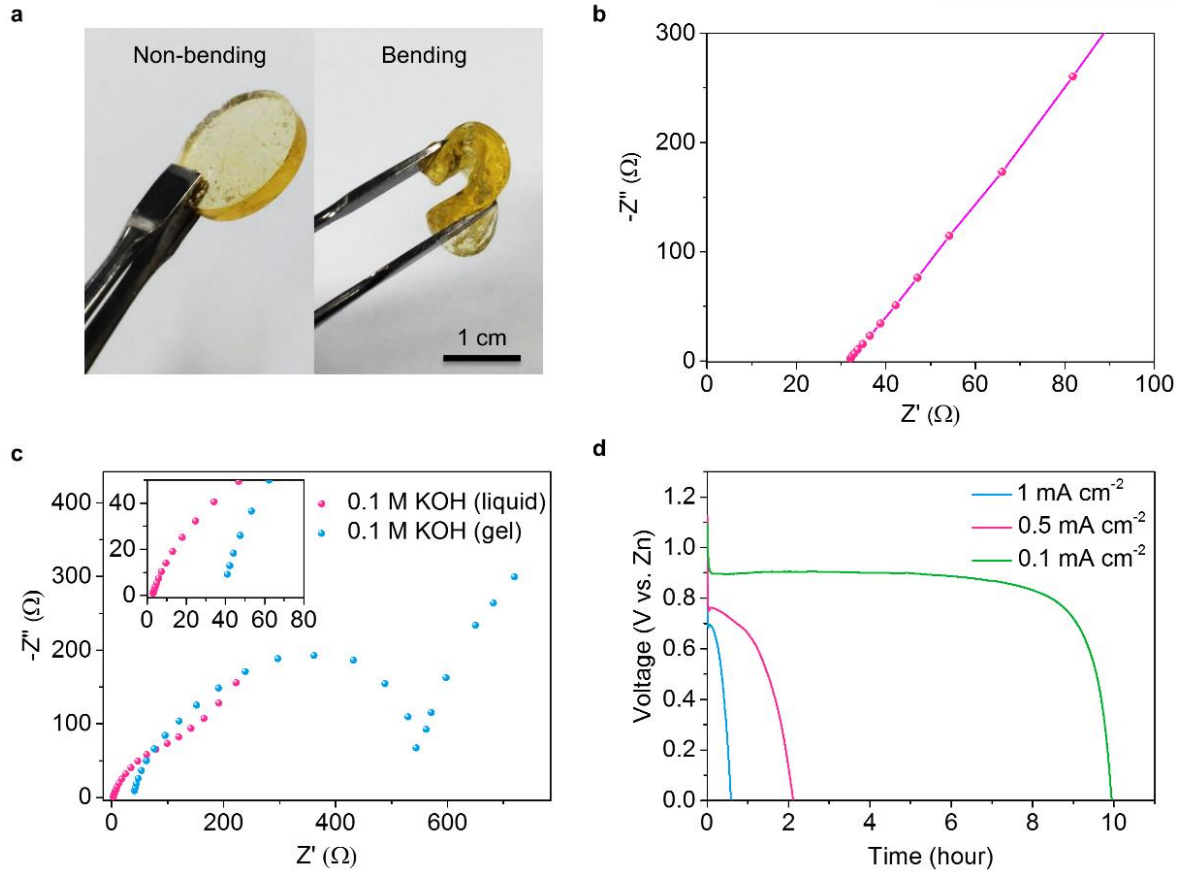

Figure 17. (a) Digital photograph of freestanding 0.1M KOH-based GGPE. (b) AC impedance spectra of the GGPE in the frequency ranged from 10 kHz to 0.01 Hz. (c) AC impedance spectra of stack-type ZAB based on GGPE in the frequency ranged from 10 kHz to 0.01 Hz. (d) Discharge curves of stack-type ZAB with the GGPE electrolyte at various current density of 0.1, 0.5 and 1 mA cm^{-2}.

Figure 18a and b display the digital photograph and its cross sectional image of the cable-type flexible ZAB, respectively. The cross-sectional image of the ZAB presents the four layers consisting of spiral zinc plate, gel polymer electrolyte, air electrode and heat-contraction rubber package. The discharge curves of stack-type and cable-type ZAB based on GGPE at 0.1 mA cm^{-2} are shown in **Figure 18**c. Fe/N/C-900 loaded and nonleaded air electrodes (MEET Company) are used for the cathode electrodes. In case of stack-type ZAB, Fe/N/C-900 loaded air electrode shows higher voltage plateau and longer duration time than that of non-loaded sample, showing 0.9 V and 10 h discharge times, respectively (**Figure 18**c). The cable-type ZAB using non-loaded air electrode shows voltage plateau with 0.76 V and 8 h 10 min duration. Noticeably, the Fe/N/C-900 loaded air electrode demonstrated better electrochemical performance with 0.92 V of voltage plateau and 9 h discharge duration. The almost flat voltage profile curve indicates that the electrical potential of the electrode is independent of its overall composition based on the Gibbs phase rule since the residual value of F is zero if the overall pressure (P) and thermodynamic temperature (T) is specified (**Figure 19**).[116] Different discharge curve of stack-type and cable types ZAB was believed to be caused by unstable contact of each component in cable-type flexible ZAB due to the low external pressure of heat-contraction rubber. However, too high external pressure when assembling the electrode may block the oxygen entrance of air electrode. In the future, to solve this problem, new kinds of alternative materials are needed to effectively provide air entrance and high packing pressure to improve the battery component's contact at the same time. **Figure 18**d demonstrates the bending test of cable-type flexible ZAB. During discharge at 0.1 mA cm^{-2}, the external strain is loaded on battery every 20 min from initial length of 7 to 3 cm. There were no differences in the discharge voltage profiles between the bending and non-bending conditions, indicating that the cable-type flexible ZAB can be successfully operated with external strain. In case of three connected cable-type flexible Zn–air batteries in series exhibited open cell voltage of 2.97 V (**Figure 21**).

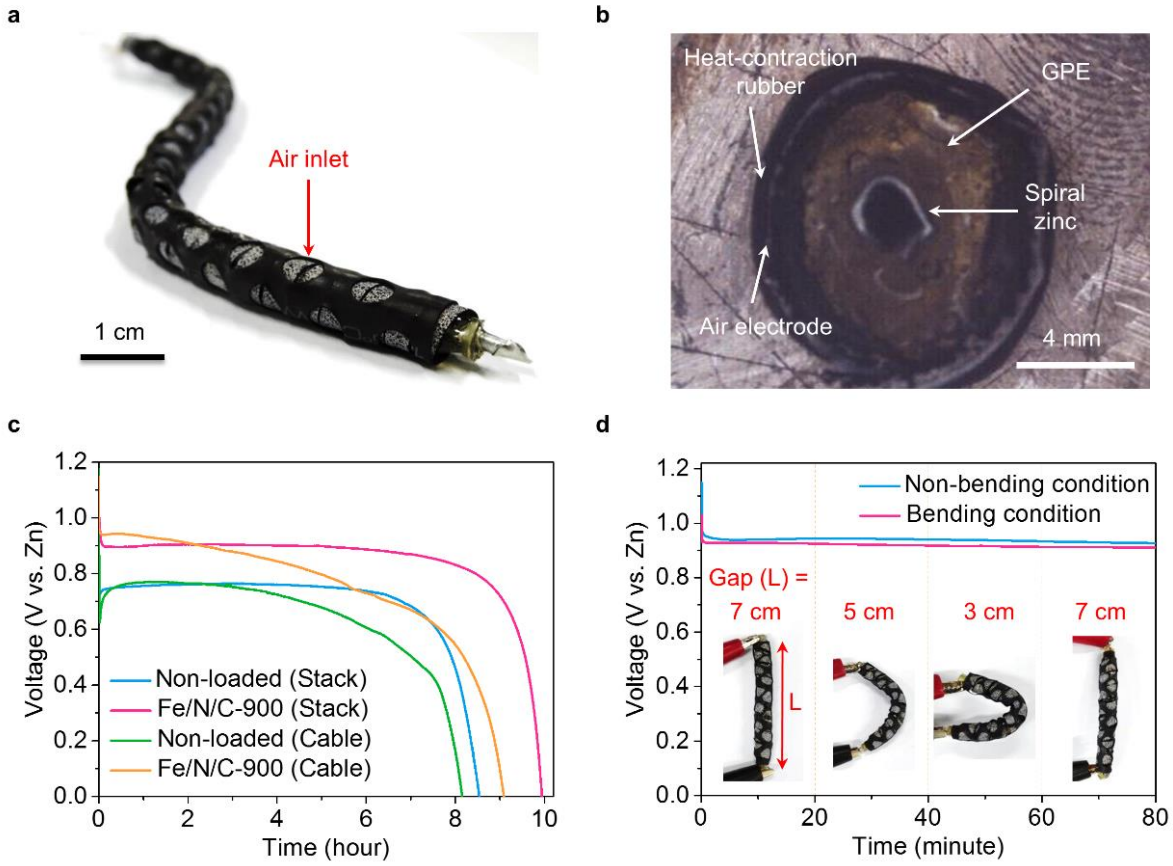

Figure 18. (a) Photograph of the prototype cable-type flexible ZAB. (b) Optical microscopy (OM) for cross-sectional image of the cable-type flexible ZAB. (c) Discharge curves of stack-type and cable-type ZAB with and without Fe/N/C electrocatalysts, respectively. The discharge current density was 0.1 mA cm^{-2}. (d) Discharge curves of cable-type ZAB by applying bending strain every 20 min at discharge current density was 0.1 mA cm^{-2} (Discharge tests of the battery were carried out using ambient static air at 24 °C).

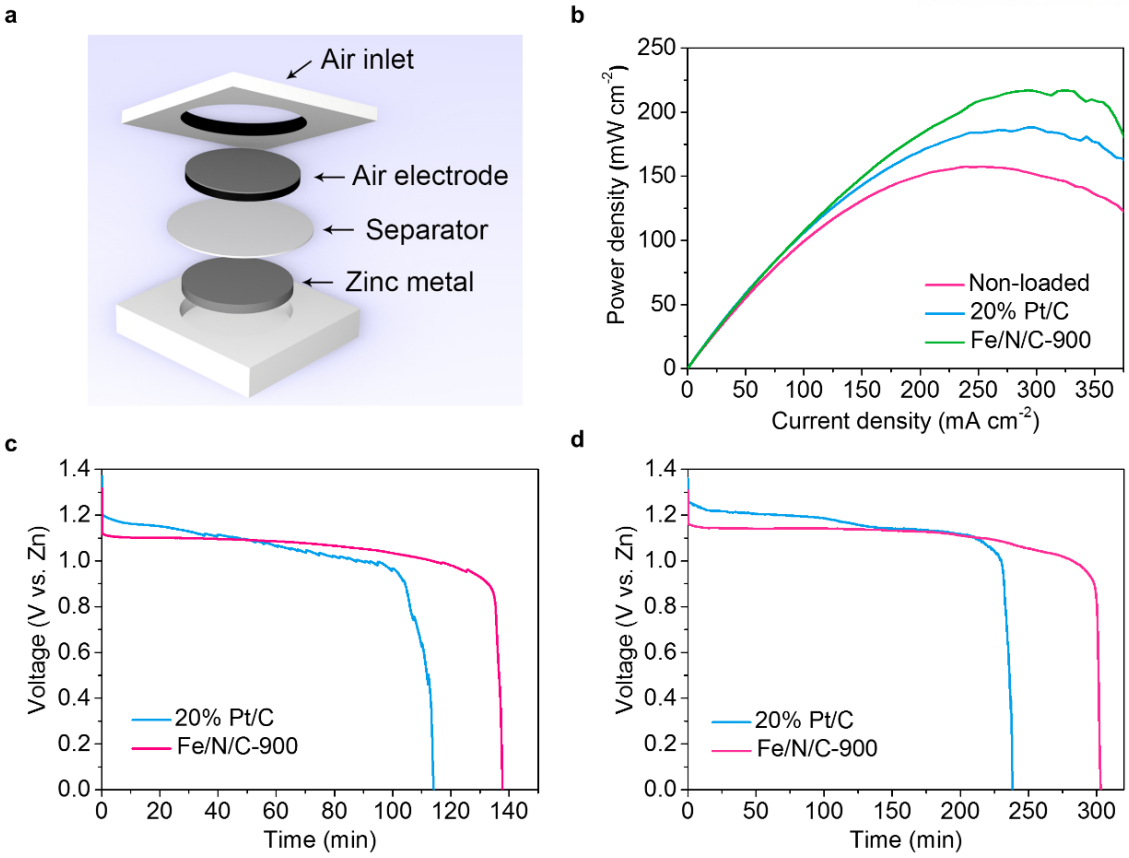

Figure 19. Electrochemical characterizations for stack-type Zn−air battery. (a) Schematic diagram of stack-type ZAB. (b) Power-current curves of stack-type ZABs with Fe/N/C-900 and 20% Pt/C electrocatalysts. (c) Discharge curves of stack-type ZABs for current density at 50 mA cm^{-2} and (d) at 25 mA cm^{-2} by using zinc granular and 6 M KOH liquid electrolyte.

As illustrated in **Figure 19**a, the stack-type Zn–air battery is composed of zinc granular anode, separator, 6 M KOH liquid electrolyte and electrocatalyst loaded air cathode. The air cathode is consisted of gas diffusion layer (GDL) and catalyst layer (e.g., Fe/N/C-900 or Pt/C catalysts). **Figure 16**b shows power-current curves of stack-type ZABs with Fe/N/C and 20 % Pt/C electrocatalysts. The current densities of the test batteries are varied from 0 to 375 mA cm^{-2}, demonstrating peak power densities of 217 mW cm^{-2} for the battery with Fe/N/C-900 catalyst, 188 mW cm^{-2} for that with the 20 % Pt/C catalyst and 157 mW cm^{-2} for the cell with air electrode without any electrocatalyst. These results suggest that the Fe/N/C-900 loaded air electrode is comparable to the commercial 20 % Pt/C loaded air electrode in performance, but the former is much cheaper than the latter. As shown in **Figure 19**b and c, we carried out stack-type ZAB test with diverse discharge current densities at 25 and 50 mA cm^{-2} by enhancing Fe/N/C-900 and 20 % Pt/C electrocatalysts, respectively. In this case, testing the ZAB under ambient static air condition is more practical environment than under purposely oxygen blowing and

ideal conditions as water vapor saturated because both of the intrinsic activity and architecture of catalysts sensitive to oxygen and electrolyte diffusion can contribute overall battery performance. As expected, the voltage profile curve shows almost flat, indicating that the electrical potential of the electrode is independent of its overall composition based on the Gibbs phase rule. The residual value of F is zero if the overall pressure (P) and thermodynamic temperature (T) is specified.[103] As a result, we can observe that Fe/N/C-900 loaded air electrode is enhanced electrochemical improvement comparable to that of 20 % Pt/C loaded air electrode. Moreover, the discharge curves at a high current density of 100 mA cm^{-2} demonstrates similar tendency with low cases (**Figure 20**). Notably, the discharge duration of Fe/N/C-900 at a current density of 100 mA cm^{-2} is much longer than that of 20% Pt/C. Consequently, the air electrode containing the Fe/N/C-900 is used for cable-type flexible ZAB.

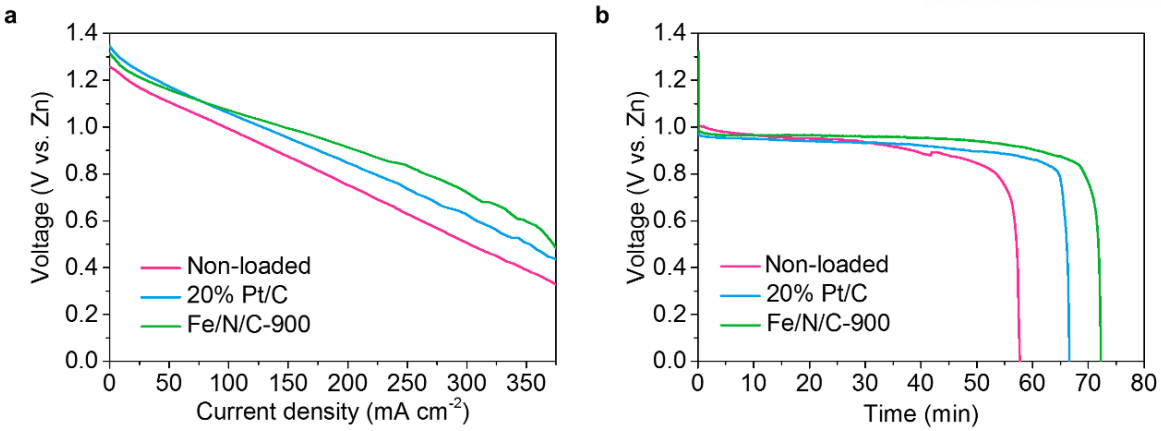

Figure 20. (a) Current-voltage of stack-type Zn–air batteries with Fe/N/C-900 (with zinc granular) and (b) discharge curve for discharge current density at 100 mA cm^{-2}.

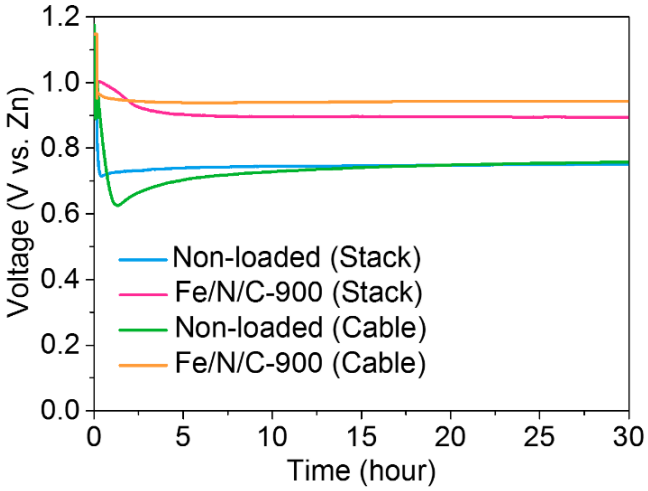

Figure 21. The magnified data of discharge curves of stack-type and cable-type ZAB with and without Fe/N/C electrocatalysts.

We used commercial air electrode (MEET Company) to load electrocatalysts. As we mentioned in the experimental section, electrocatalyst layer was loaded on the air electrode using ink solution. Note that the commercial air electrode was not uniform. Accordingly, we observed the difference of open circuit voltage (OCV) between stack- and cable-type Zn–air batteries. As shown in **Figure 21**, the OCV of stack-type Zn–air battery with Fe/N/C-900 was 1.09 V. Moreover, they showed the voltage drop of 0.19V during initial discharging. On the other hand, the OCV of cable-type Zn–air battery with Fe/N/C-900 electrocatalyst was 1.14 V. However, the voltage drop was slightly larger than that of stack-type Zn–air battery, showing 0.21 V. Interestingly, both of the stack- and cable-type Zn–air batteries showed similar results, which could be ascribed to the non-uniformity of the air electrode.

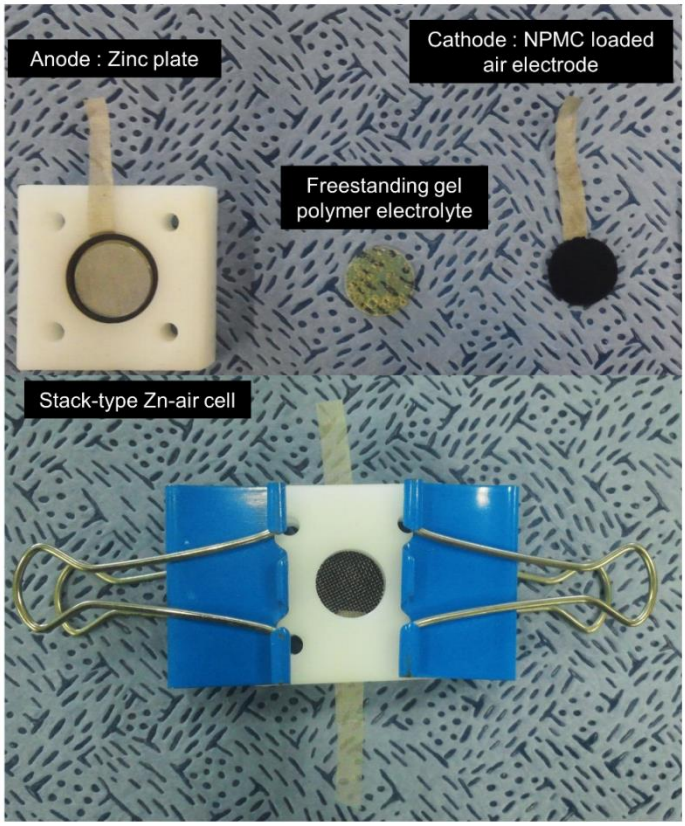

Figure 22. Digital photograph and schematic diagram of stack-type Zn–air battery.

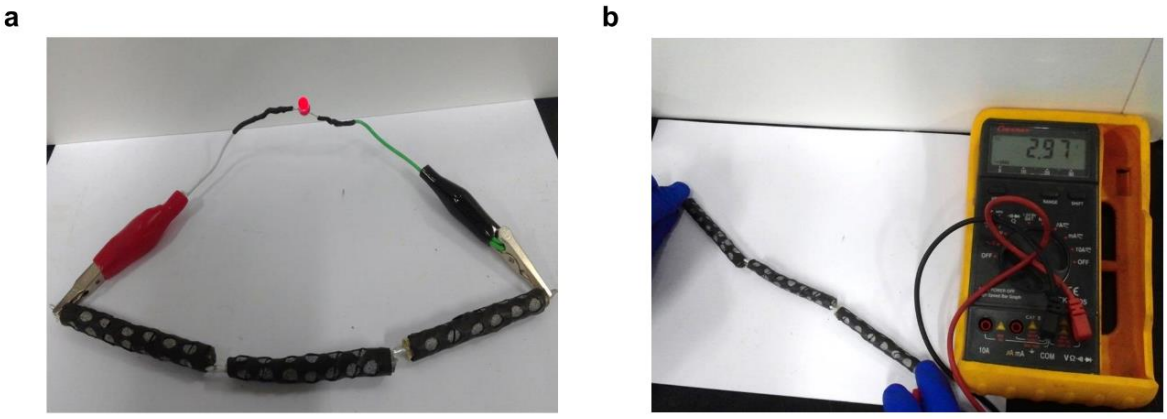

Figure 23. Real image of connected cable-type flexible Zn–air battery in series (a) with LED and (b) its open circuit voltage (OCV).

In order to evaluate the practical performance of cable-type flexible Zn–air battery, we used red light emitting diode (LED). The Zn–air battery demonstrated low power density because of low KOH concentration in gel polymer electrolyte (GPE). We needed to select effective electrical devices. The red LED needs only 1.9 to 2.1 V for operation. As presented in **Figure 18**c, the cable-type flexible Zn–air battery showed the discharge voltage values ranged from 0.75 to 0.9 V. Thus, we should connect the batteries in series for operating the LED (**Figure 23**). The OCV value of serially connected cable-type flexible Zn–air battery was ≈2.97 V.

2.4 Summary

In conclusion, we propose a cable-type flexible ZAB consisting of spiral zinc anode, freestanding gel polymer electrolyte (GPE) and an air cathode containing non-precious metal catalyst (NPMC) for broad application toward wearable electronic devices by overcoming the design limitation. To achieve a successful flexibility of the ZAB, we designed an all-solid-state battery system with gelatin-based GPE (GGPE) with a KOH solution due to its high ionic conductivity. More importantly, the cable-type flexible ZAB demonstrated successful operation with external strain.

Chapter 3

Single crystalline pyrochlore nanoparticles with metallic conduction as efficient bi-functional oxygen electrocatalysts for Zn−air batteries

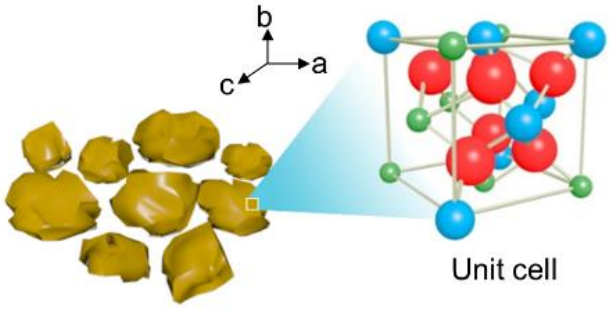

Pyrochlore oxide catalysts
($A_2B_2O_{7-x}$, A = Pb and Sm, B = Ru)

Oxygen reduction reaction (ORR) or oxygen evolution reaction (OER) electrocatalysts including carbon-, non-precious metal-, metal alloy-, metal oxide- and carbide/nitride-based materials are of great importance for energy conversion and storage technologies. Among them, metal oxides (e.g., perovskite, pyrochlore) are known as the promising candidates as electrocatalysts. Nevertheless, the intrinsic catalytic activities of pyrochlore oxides are still poorly understood because of the formation of undesirable phases derived from synthesis processes. Herein, we present highly pure single crystalline pyrochlore nanoparticles with metallic conduction ($Pb_2Ru_2O_{6.5}$) as an efficient bi-functional oxygen electrocatalyst. Notably, it was experimentally shown that the covalency of Ru-O bonds affects the ORR and OER activities by comparing X-ray absorption near edge structure (XANES) of the metallic $Pb_2Ru_2O_{6.5}$ and insulating $Sm_2Ru_2O_7$ for the first time. Moreover, we followed the interatomic distance changes of Ru-O bond by *in situ* X-ray absorption spectroscopy (XAS) to investigate the structural stabilities of the pyrochlore catalysts during electrocatalysis. The highly efficient metallic $Pb_2Ru_2O_{6.5}$ exhibited outstanding bi-functional catalytic activities and stabilities for both ORR and OER in aqueous Zn–air batteries.

This chapter has been published.

Park J., Risch M., Nam G., Park M., Shin T. J., Park S., Kim M. G.*, Shao-horn Y.*, Cho J.* "Single crystalline pyrochlore nanoparticles with metallic conduction as efficient bi-functional oxygen electrocatalysts for Zn–air batteries", *Energy Environ. Sci.*, 10, 129-136 (2017).

3.1 Introduction

Environmentally friendly energy storage systems are required to reduce environmental contamination and fossil fuel dependence. Among various energy conversion and storage technologies, metal–air batteries with high power and energy densities are promising candidates for the operation of portable devices and electric vehicles,[1, 117] particularly Zn–air batteries due to their long shelf-life, low price and abundant zinc deposits.[4-6, 10, 118] Zn–air batteries have higher specific energy density (ca. 1,084 Wh kg^{-1}) than Li-ion batteries (200–250 Wh kg^{-1}).[4] However, to achieve rechargeable Zn–air batteries, there are critical limitations on charging and discharging because of the sluggish rates of the oxygen reduction reaction (ORR) and oxygen evolution reaction (OER).[12, 42] Highly active and stable ORR or OER electrocatalysts including carbon-,[47, 48, 111, 119-121] non-precious metal-,[121-124] metal alloy-,[125] carbide/nitride-,[126-128] metal oxide-based materials[107, 129-136] are the key for enhancing the electrochemical performance of Zn–air batteries. However, the current electrocatalysts other than metal oxide-based materials showed poor bi-functional electrocatalytic activity for both ORR and OER in rechargeable Zn–air batteries.

Along with the extensive research and development of metal oxide-based materials, perovskite oxides[107, 129-136] have been intensively investigated as bi-functional electrocatalysts in rechargeable Zn–air batteries with high ORR ($O_2 + 2H_2O + 4e^- \rightarrow 4OH^-$) and OER ($4OH^- \rightarrow O_2 + 2H_2O + 4e^-$) activities due to their stable structures and chemical flexibilities.[63-66] Suntivich *et al.* demonstrated a volcano-shaped relationship between the e_g orbital filling of B-site cations and intrinsic catalytic activities of perovskite oxides (ABO_3).[64, 66] They also proposed the metal-oxygen covalency as a secondary factor influencing activity. Jung *et al.* explained that catalytic activity of perovskite oxides is dependent on the concentration of oxygen vacancies and valence state of B-site cations via *ex situ* X-ray absorption near edge structure (XANES) and extended X-ray absorption fine structure (EXAFS) analyses.[131] However, these perovskite oxides showed lower ORR activities than other ORR catalysts. Another limitation of perovskite oxides is the formation of undesirable phases during heat treatment.[137]

Furthermore, pyrochlore oxides ($A_2B_2O_{7-x}$) have been studied as possible electrocatalyst candidates for ORR and/or OER among metal oxide-based materials. Examples include $Pb_2Ir_{2-x}Pb_xO_{7-y}$,[80] $Bi_2[Ru_{2-x}Bi_x]O_{7-y}$,[138] $Pb_2[Ru_{2-x}Pb_x^{4+}]O_{6.5}$,[80, 138] $Pb_2Ru_2O_{6.5}$,[139-141] $Bi_{2.4}Ru_{1.6}O_7$,[141] $Bi_2Ru_2O_7$[139, 142] and $Pb_2Ru_2O_{7-x}$[73] (**Table 4**). It was reported that their high catalytic activity and electrical conductivity can be ascribed to the metallic property of pyrochlore oxides. However, in terms of the structural integrity, previously reported pyrochlore catalysts showed undesirable phases and impurities such as RuO_2 derived from the synthesis processes (e.g., solid-state reaction and precipitation). Therefore, high phase purity is required to investigate the intrinsic catalytic activities of pyrochlore oxides. Oh *et al.* studied the electrochemical behavior of a mesoporous pyrochlore catalyst for aprotic Li–O_2 batteries and proposed a mechanism

for Li_2O_2 formation.[83] However, the origin of outstanding catalytic activities and structural stabilities of pyrochlore oxides in aqueous Zn–air batteries are not clearly revealed, in part due to the difficulty in identification during electrocatalysis.

Herein, we present the highly pure single crystalline pyrochlore nanoparticles with metallic conduction ($Pb_2Ru_2O_{6.5}$) as an efficient electrocatalyst. Notably, the covalency near the surface of pyrochlore oxides directly related to the ORR and OER activities.[141] Accordingly, we provide experimental evidence that the covalency of Ru-O bonds affects the ORR and OER activities by comparing X-ray absorption near edge structure (XANES) of the metallic $Pb_2Ru_2O_{6.5}$ and insulating $Sm_2Ru_2O_7$ for the first time. In addition, we use *in situ* X-ray absorption spectroscopy (XAS) to follow the distance changes between ruthenium at the B-site and oxygen in pyrochlore oxides in order to monitor the structural stabilities of the pyrochlore catalysts during ORR and OER in real-time. Furthermore, the highly efficient metallic $Pb_2Ru_2O_{6.5}$ nanoparticles demonstrates outstanding ORR and OER activities in half- and full-cells for primary and rechargeable Zn–air batteries.

Table 4. Reported pyrochlore oxide electrocatalysts either ORR or OER.

Catalysts	Synthetic procedure	Crystalline phase	Half-cell	Full-cell	Reference
$Pb_2Ru_2O_{6.5}$	**Sol-gel 650 °C**	**Pure**	**ORR OER**	**Zn-air batteries**	**This work**
$Sm_2Ru_2O_7$	**Sol-gel 1050 °C**	**Pure**	**ORR OER**	**Zn-air batteries**	**This work**
$Pb_2Ir_{2-x}Pb_xO_{7-y}$	Solid state reaction 850 °C	n/a	ORR OER	n/a	J. Am. Chem. Soc. **1990**, 112, 2076
$Bi_2[Ru_{2-x}Bi_x]O_{7-y}$	Precipitation 200 °C	n/a	ORR OER	n/a	J. Electrochem. Soc. **1983**, 130, 1851
$Pb_2[Ru_{2-x}Pb_x^{4+}]O_{6.5}$	Solid state reaction 850 °C	n/a	ORR OER	n/a	J. Am. Chem. Soc. **1990**, 112, 2076
$Pb_2[Ru_{2-x}Pb_x^{4+}]O_{6.5}$	Precipitation 200 °C	n/a	ORR OER	n/a	J. Electrochem. Soc. **1983**, 130, 1851
$Pb_2[Ru_{2-x}Pb_x^{4+}]O_{6.5}$	Solution 100 °C	Pure	n/a	Li-air batteries	Nat. Chem. **2012**, 12, 1004
$Pb_2Ru_2O_{6.5}$	Solid state reaction 900 °C	n/a	OER	n/a	Bull. Korean Chem. Soc. **1997**, 18, 972
$Pb_2Ru_2O_{6.5}$	Precipitation 300 °C	Pure	ORR OER	n/a	J. Electrochem. Soc. **1999**, 146, 4145
$Pb_2Ru_2O_{6.5}$	Precipitation 272atm 45 °C	Pure	OER	n/a	J. Mater. Chem. A. **2015**, 3, 10819
$Bi_{2.4}Ru_{1.6}O_7$	Precipitation 300-500 °C	Impure	OER	n/a	J. Mater. Chem. A. **2015**, 3, 10819
$Bi_2Ru_2O_7$	Solid state reaction 900 °C	n/a	OER	n/a	Bull. Korean Chem. Soc. **1997**, 18, 972

$Bi_2Ru_2O_7$	Sol-gel 600-900 °C	Impure	n/a	SOFC	RSC Advances **2013**, 3, 19866
$Pb_2Ru_2O_{7-x}$	Precipitation 700 °C	Impure	ORR	n/a	J. Electrochem. Soc. **2015**, 162, 129

3.2 Experimental detail

Preparation of pyrochlore oxide catalysts: To prepare the pyrochlore oxide catalysts, a buffer solution was required. The buffer solution, NH_4–EDTA, was made with a mixture of 10 g anhydrous ethylenediaminetetraacetic acid (≥ 99% titration, Sigma-Aldrich), 1 M ammonia solution (28.0–30.0%, Samchun chemical) and 1.5 mL nitric acid (HNO_3, ACS regent 70%, Sigma-Aldrich) at a solution pH of 7. To prepare $Pb_2Ru_2O_{6.5}$, 8.22×10^{-4} mol lead (IV) acetate (reagent grade 95%, Sigma-Aldrich), 8.22×10^{-4} mol ruthenium (III) nitrosyl nitrate solution (1.5 wt% Ru, Sigma-Aldrich) and 10 g anhydrous citric acid (99%, Sigma-Aldrich) were dissolved and stirred with the buffer solution for 24 h at 150 °C. At this point, gelation was observed. The gelled solution was transferred to an oven at 200 °C for 6 h drying. The prepared powder was calcined in air at 650 °C for 5 h. To prepare $Sm_2Ru_2O_7$, a similar process was used except that the A-site metal precursor was 8.22×10^{-4} mol of samarium (III) nitrate hexahydrate, respectively and the final calcination temperature was 1050 °C.

Preparation of the catalyst inks and working electrode: The catalyst inks were prepared with mixture of 16 mg of the pyrochlore oxides powder, 4 mg of ketjenblack carbon (EC 600JD), 200 μL of the 5wt% of Nafion in mixture of lower aliphatic alcohols and H_2O (Sigma-Aldrich) and 800 μL of ethanol. Briefly, the catalyst inks were prepared by ultrasonically mixing in distilled water for 1 h to make homogeneous mixture. The portion of 5 μL of inks were loaded on the glassy carbon of rotation ring disk electrode (RRDE) as the working electrode. The area of RRDE was 0.1256 cm^2. As a result, the loading levels of the pyrochlore oxides were 0.637 mg_{cat} cm^{-2}. For the loading level of 79.6 μg_{pt} cm^{-2} benchmarking catalyst, 10 mg of Pt/C on Vulcan XC 72 (20wt%, Premetek Co.) was dispersed in 200 μL of the 0.05% titrated Nafion solution and 800 μL of ethanol. After that, this catalyst ink was prepared by ultrasonically mixing in distilled water for at least 1 h to make homogeneous ink. Then, 5 μL of ink was loaded on the glassy carbon of working electrode that the loading levels of 20% Pt/C and the pure Pt were 0.398 $mg_{(20\%\ Pt/C)}$ cm^{-2} and 79.6 μg_{Pt} cm^{-2}, respectively.

Electrochemical measurements: A three-electrode cell was used to measure the electrocatalytic activities of the pyrochlore oxides. Rotating ring disk electrode (RRDE) (ALS Co., Ltd) tests were carried out based on the pyrochlore oxides film (loaded on the glassy carbon of RRDE) for the working electrode in O_2-saturated 0.1 M KOH alkaline electrolyte. Platinum wire and Hg/HgO were used as the counter and reference electrodes, respectively. Electrochemical characterizations were conducted using a bipotentiostat (IviumStat). The scan rate of 10 mV s^{-1} was swept from 1.13 V to 0.26 V (vs. RHE) for oxygen reduction reaction (ORR) and from 1.23 to 1.82 V (vs. RHE) for oxygen evolution reaction (OER). The ORR capacitance were corrected by averaging current of cyclic voltammetry plots (CVs) in O_2- and Ar-saturated electrolytes. The OER CVs were capacitive-corrected by averaging current of

the forward and backward sweeps. The capacitive-corrected ORR and OER currents were ohmically corrected with the measured ionic resistance (≈45 Ω).

In addition, a ring potential of 0.4 V (vs. Hg/HgO) was applied to oxidize peroxide during ORR. The collection efficiency (N) was determined under Ar atmosphere using 10 mM $K_3[Fe(CN)_6]$, which is around 0.41. This value is similar to the theoretical value of 0.42. The peroxide yield (H_2O^-) and the number of transferred electrons (n) were calculated from the below equations.

$$H_2O^-(\%) = 100\frac{2I_r/N}{I_d+I_r/N} \quad (1)$$

$$\mathrm{n} = 4\frac{I_d}{I_d+I_r/N} \quad (2)$$

Primary Zn-air batteries tests: For primary Zn–air batteries tests based on the pyrochlore oxides, 0.75 g of zinc granular is used as an anode and 200 μL of 6 M KOH was used as an electrolyte. A nylon membrane was used as a separator. The air electrode which is a cathode was prepared by uniformly loaded gas diffusion layer (GDL) (the catalyst ink formulation: 16 mg of catalyst, 4 mg of ketjenblack, 200 μL of the 5wt% of the Nafion solution and 800 μL of ethanol on nickel mesh. Thickness of the electrode is around 500 μm. The assembled primary Zn–air batteries were tested at the discharge current densities of 20 mA cm^{-2}. The GDL was prepared from a mixture of activated charcoal (Darco G-60A, Sigma-Aldrich) and PTFE binder (60 wt% PTFE emulsion in water, Sigma-Aldrich) at a weight ratio of 7:3 with about 450 μm of thickness to ensure proper gas distribution and sufficient current collection. This prepared GDL was used as the reference for comparison to confirm enhanced performance of air electrode based on catalysts in polarization curves of the Zn–air batteries.

Rechargeable Zn-air batteries tests: For primary Zn–air batteries tests based on pyrochlore oxides, 0.5 g of zinc plate is used as an anode and 2 mL of 6 M KOH with 0.2 M ZnO as an electrolyte. Preparation method of air electrode with the catalysts is same as primary Zn–air batteries except nickel mesh. Thickness of the electrode is around 950 μm. In this case, nickel foam is used for air electrode instead of mesh. The assembled rechargeable Zn–air batteries were tested at the discharge/charge current densities of 10 mA cm^{-2}.

Materials characterizations: The material morphologies were examined using SEM (VERIOS 460, FEI), high-resolution transmission electron microscopy (HR-TEM) (JEM-2100F, JEOL) operating at 200 kV. Powder analysis was performed using an X-ray diffractometer (XRD) (D/Max2000, Rigaku). X-ray absorption near edge structure (XANES) and extended X-ray absorption fine structure (EXAFS) were collected on BL10C beam line at the Pohang light source (PLS-II) with top-up mode operation under a ring current of 200 mA at 3.0 GeV.

3.3 Results and discussion

Figure 24a shows the synthetic procedure for the highly pure single crystalline pyrochlore oxide nanoparticles ($A_2Ru_2O_{7-x}$, A = Pb and Sm). We employed a sol-gel method in order to crosslink the A-site and B-site cations using a citric acid as chelating agent. Then, the pyrochlore oxides were crystallized *via* a heat treatment method at temperatures of 650 °C for $Pb_2Ru_2O_{6.5}$ and 1,050 °C for $Sm_2Ru_2O_7$, respectively. As shown in **Figure 24**b, cubic phases of the pyrochlore oxides ($A_2B_2O_{7-x}$) without any impurities were successfully prepared, as confirmed by X-ray diffraction (XRD). The space group of cubic $Pb_2Ru_2O_{6.5}$ has F-43m symmetry. This structure includes 0.5 mol defects at the oxygen sites, which originate from the charge imbalance between divalent lead ions and tetravalent and/or pentavalent ruthenium ions. On the other hand, there is no defects at the oxygen sites in the other sample because of the balanced oxidation states of trivalent samarium and tetravalent ruthenium ions; this sample is cubic crystal with Fd-3m symmetry. **Figure 24**c exhibits the scanning electron microscopy (SEM) image of $Pb_2Ru_2O_{6.5}$. The primary particles of the pyrochlore oxides were aggregated, showing angular shapes with average sizes of ≤ 200 nm. To investigate the highly crystalline nanostructure of the pyrochlore particles, fast Fourier transform (FFT) image of high resolution transmission electron microscopy (HR-TEM) was obtained by focused ion beam (FIB) sampling (**Figure 24**d). The FFT analysis of $Pb_2Ru_2O_{6.5}$ was carried out in the [110] direction as the main zone axis. The FFT image showed cubic phases based on the unit spots of (–11–1) and (–111), with an interaxial angle of 70.53°. Also, high-angle annular dark field scanning TEM (STEM-HAADF) images with $Pb_2Ru_2O_{6.5}$ d-spacing identified cubic pyrochlore oxide phases on the lattice scale (**Figure 24**e). The lattice fringes with *d*-spacing values of 0.304 nm correspond to (111) crystal planes. The (002) crystal planes showed d-spacing values around 0.51 nm. The $Sm_2Ru_2O_7$ exhibited the same cubic phase as $Pb_2Ru_2O_{6.5}$ (**Figure 25**). Notably, the FFT patterns of both samples showed the formation of single crystalline phases. Elemental composition and distribution of the pyrochlore oxides were analyzed in more detail by STEM energy-dispersive X-ray spectroscopy (EDS) and elemental mapping (**Figures 26–29**). The atomic ratios of A- and B-site cations in the pyrochlore oxides were ca. 1 and these values corresponded exactly to the results from XRD analysis (**Table 5 and 6**). Collectively, these results revealed that cubic phases of the pyrochlore oxides with highly pure single crystalline nanoparticles were successfully synthesized.

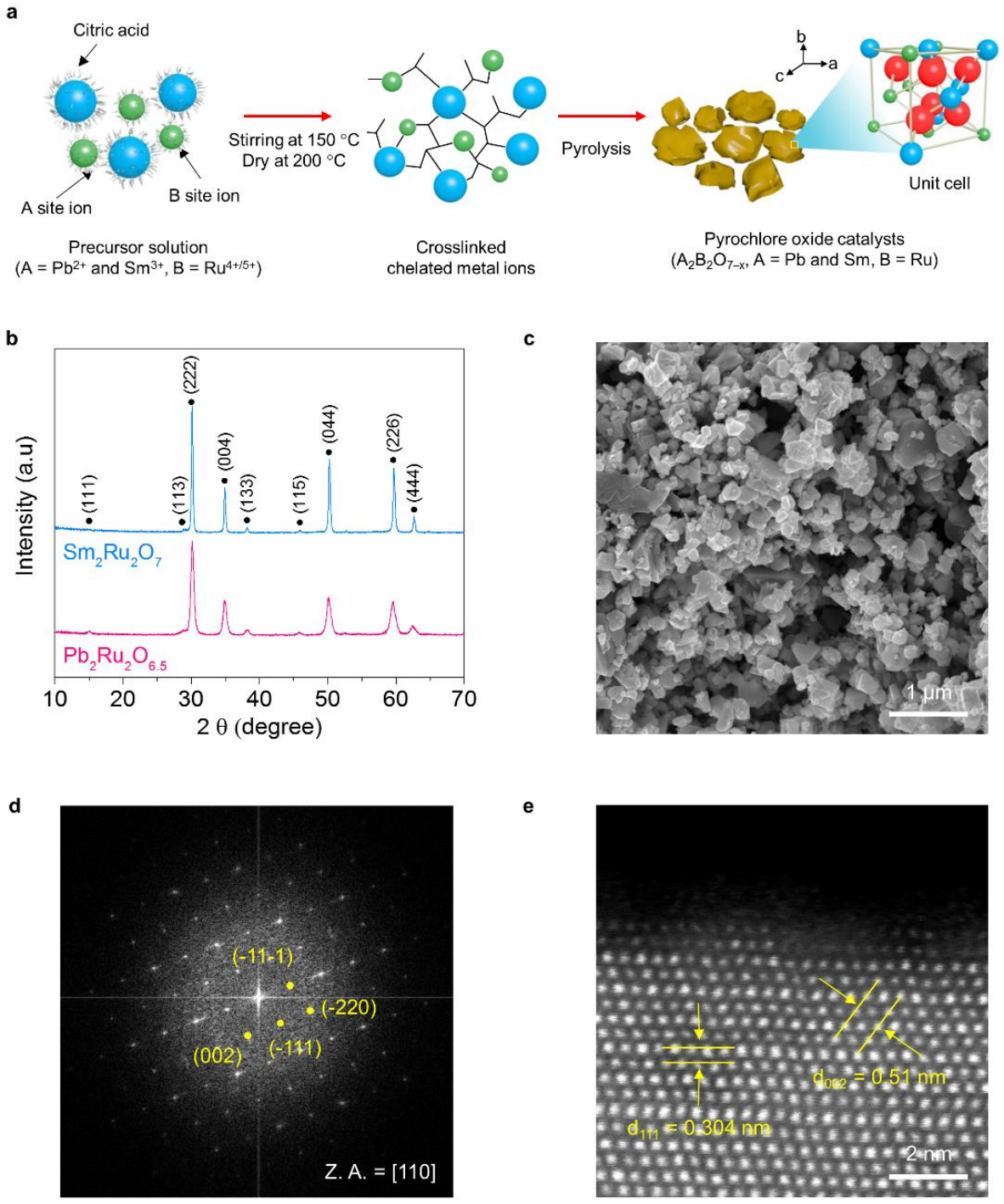

Figure 24. Preparation, morphology and structural characterization of the highly pure single crystalline pyrochlore oxide nanoparticles ($A_2B_2O_{7-x}$, A = Pb and Sm, B = Ru). (a) Schematic representation of the preparation process for the highly pure single crystalline pyrochlore oxide nanoparticles. During sol-gel process, A-site cations (blue spheres) are crosslinked with B-site cations (green spheres) by citric acid (black lines). After heat-treated at the different temperature (650 °C for $Pb_2Ru_2O_{6.5}$ and 1,050 °C

for $Sm_2Ru_2O_7$), the powdered pyrochlore member (red brown solid figures) are synthesized. (b) XRD patterns of $Pb_2Ru_2O_{6.5}$ and $Sm_2Ru_2O_7$. (c) SEM image, (d) FFT image of HR-TEM along the [110] zone axis and (e) STEM-HAADF image of $Pb_2Ru_2O_{6.5}$. In (d), the indexed points refer to the lattice planes of (–11–1), (–220), (–111) and (002) in clockwise order. In (e), 0.304 and 0.510 nm denote the lattice spacing on the (111) and (002) planes, respectively.

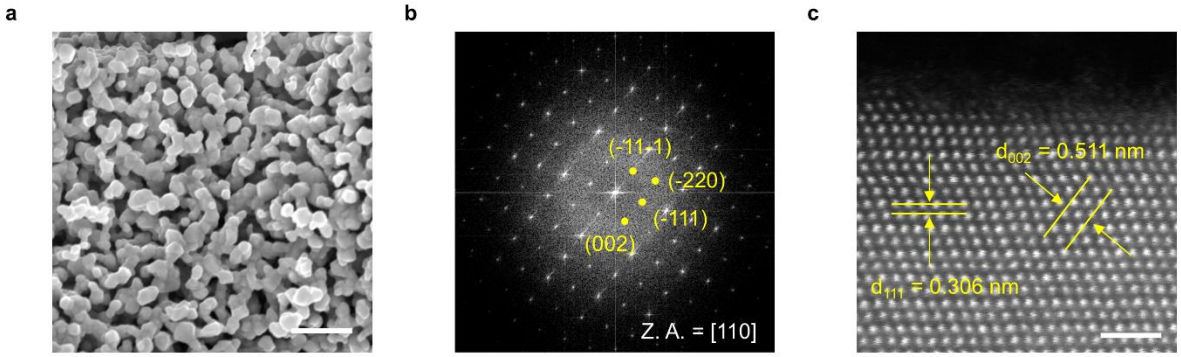

Figure 25. (a) SEM image of $Sm_2Ru_2O_7$. The primary particles of the pyrochlore catalyst showed angular shapes with average sizes of ≈200 nm. (b) HR-TEM FFT image along the [110] zone axis with indexed unit spots of $Sm_2Ru_2O_7$. The indexed points refer to the lattice planes of (–11–1), (–220), (–111) and (002) in clockwise order. (c) Lattice scale STEM-HAADF image with d-spacing of $Sm_2Ru_2O_7$. 0.306 nm and 0.511 nm denote the lattice spacing indicated by yellow arrows and lines, on the (111) and (002) planes, respectively. Scale bars are 1 μm and 2 nm in (a) and (c), respectively.

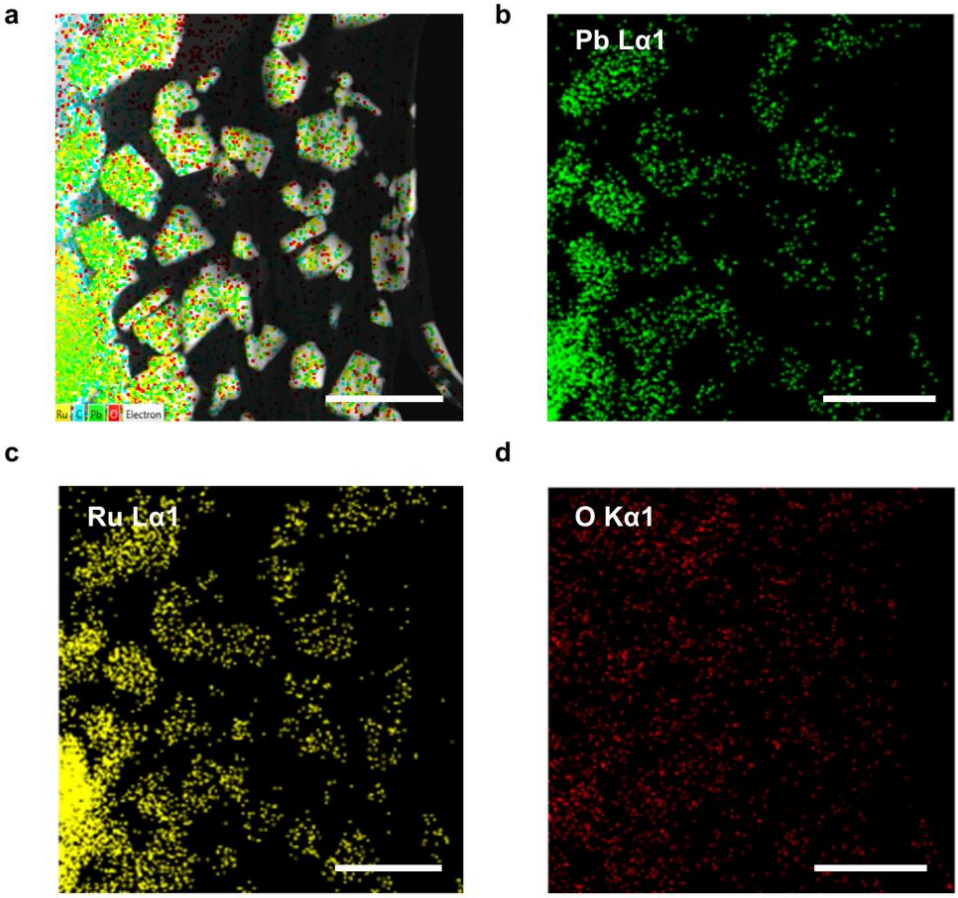

Figure 26. STEM-HAADF-EDS images of $Pb_2Ru_2O_{6.5}$ and elemental maps of (a) all elements, (b) Pb, (c) Ru and (d) O. Scale bars are 500 nm in (a), (b), (c) and (d).

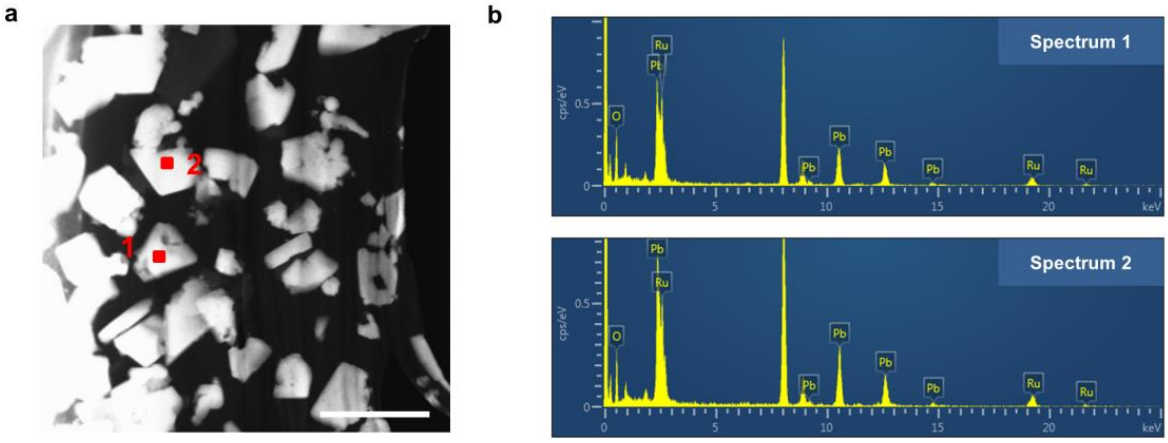

Figure 27. (a) STEM and (b) EDS of $Pb_2Ru_2O_{6.5}$ at different point. Scale bar is 500 nm in (a).

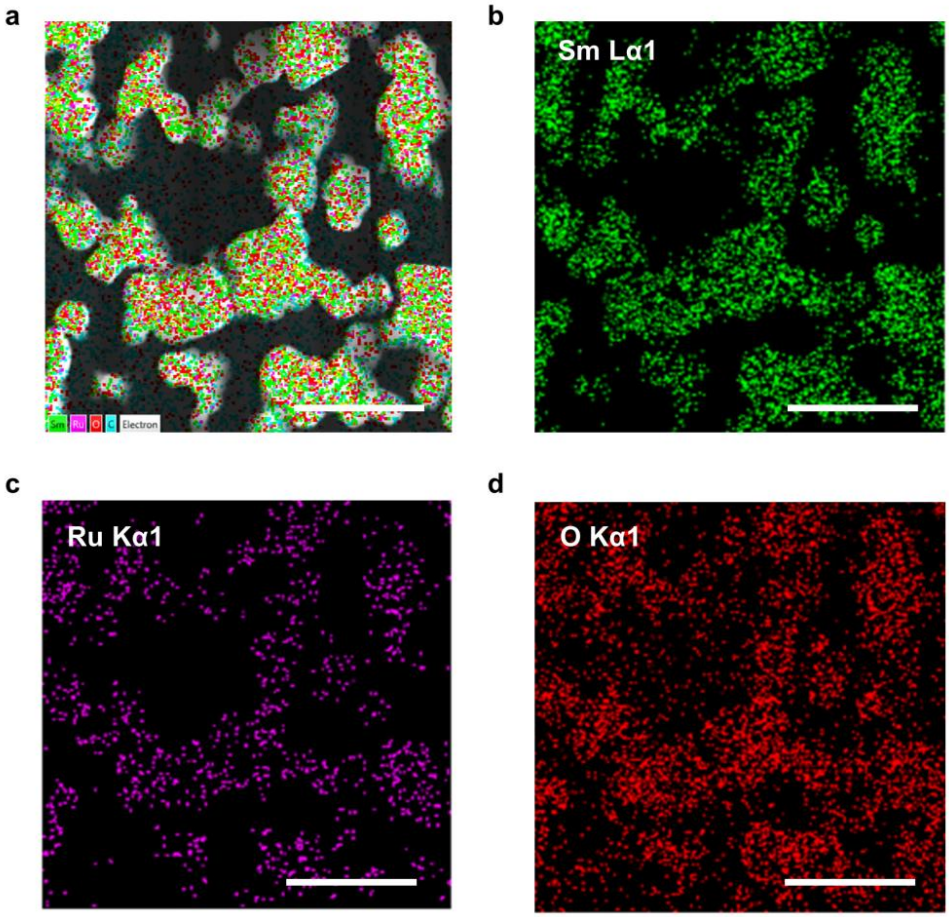

Figure 28. STEM–HAADF–EDS images of $Sm_2Ru_2O_7$ and element maps of (a) all elements, (b) Sm, (c) Ru and (d) O. Scale bars are 500 nm in (a), (b), (c) and (d).

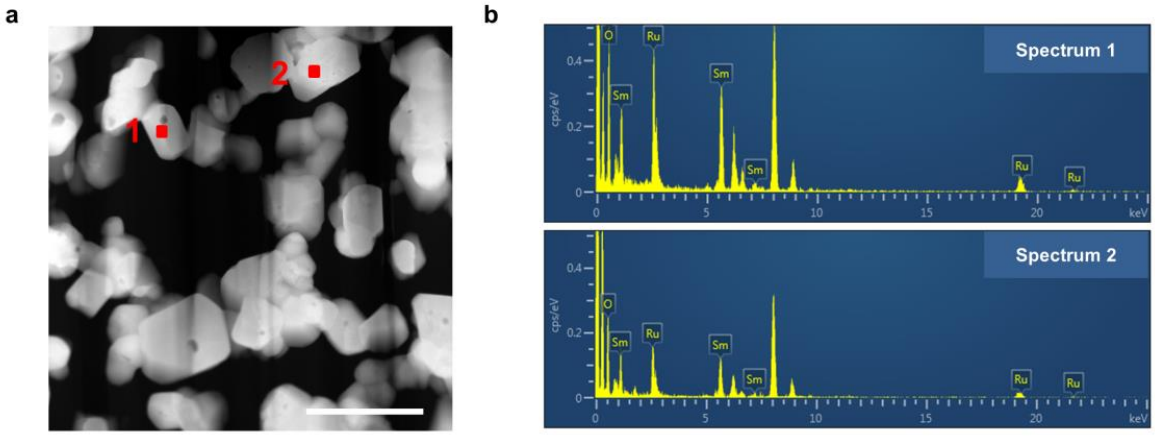

Figure 29. (a) STEM and (b) EDS of $Sm_2Ru_2O_7$ at different points. Scale bar is 500 nm in (a).

Table 5. Percent composition and atomic ratios of lead and ruthenium in $Pb_2Ru_2O_{6.5}$ at different points (**Figure 27**).

Catalyst	Sites	Pb (wt %)	Ru (wt %)	Pb/Ru (At. %)
$Pb_2Ru_2O_{6.5}$	1	58.70	28.92	1.01
	2	62.61	28.38	0.93

Table 6. Percent composition and atomic ratios of samarium and ruthenium in $Sm_2Ru_2O_7$ at different points (**Figure 29**).

Catalyst	Sites	Sm (wt %)	Ru (wt %)	Sm/Ru (At. %)
$Sm_2Ru_2O_7$	1	51.22	28.47	1.2
	2	47.15	26.18	1.14

Figure 30 shows the ohmic- and capacitive-corrected electrocatalytic activities of the pyrochlore oxides as bi-functional electrocatalysts for ORR and OER. The linear scan voltammogram (LSV) curves for the ORR exhibited an exceptional onset potential for $Pb_2Ru_2O_{6.5}$ of 0.89 V vs. RHE (**Figure 2**a). Commercial Pt/C was used as a reference, which showed an onset potential of 1.05 V. Compared with the limiting current density of Pt/C (–5.7 mA cm^{-2}_{disk}), $Pb_2Ru_2O_{6.5}$ showed a very similar value of –5.7 mA cm^{-2}_{disk} near 0.5 V. In the ORR, there are two pathways: direct four-electron and intermediate two-electron reactions. We can determine the reaction pathway by calculating the disk and ring current densities. As shown in **Figure 30**b, the $Pb_2Ru_2O_{6.5}$ demonstrates a highly increased number of transferred electrons (n) of almost 4; compare this value to the $Sm_2Ru_2O_7$ ($\leq$ 3.5). The corresponding limiting current density for the resulting value (n = 4) is about –5.7 mA cm^{-2}_{disk} which is consistent with experimentally obtained values for Pt/C and $Pb_2Ru_2O_{6.5}$ in **Figure 30**a. This dominant four-electron pathway implies superb catalytic activity of the $Pb_2Ru_2O_{6.5}$ for ORR.

To further understand the kinetic reactions, mass transfer-corrected Tafel plots for the ORR were measured for the pyrochlore catalysts and Pt/C (**Figure 30**c). At low overpotential regions, the average Tafel slopes of the pyrochlore was around 60 mV dec^{-1}, similar to Pt/C (60 mV dec^{-1}), implying that the rate determining step (RDS) in the ORR is the formation of superoxide *via* a one electron transfer reaction ($O_{2(ads.)} + e^- \rightarrow O_{2(ads.)}^-$) (**Table 7**).[116] It also indicated mass and charge transfer-limited processes at low and high overpotential regions, respectively.[143] Higher kinetic current density of $Pb_2Ru_2O_{6.5}$ as compared to $Sm_2Ru_2O_7$ at 0.85 V is an indicative of higher ORR activity (**Figure 30**d). $Pb_2Ru_2O_{6.5}$ is among the most active oxides reported for ORR (**Table 8**). Moreover, the $Pb_2Ru_2O_{6.5}$ shows a higher OER activity with lower onset potentials than that of the $Sm_2Ru_2O_7$ and RuO_2 reference sample (**Figure 30**e). Compared with the current density of RuO_2 at 1.55 V (1.42 mA cm^{-2}_{disk}), the $Pb_2Ru_2O_{6.5}$ showed a higher value of 2.96 mA cm^{-2}_{disk}, which could be ascribed to the significantly enhanced bi-functional catalytic activities (**Table 9**). Moreover, Tafel slope of the $Pb_2Ru_2O_{6.5}$ showed 114.2 mV dec^{-1} (**Table 10**), similar to the OER catalyst standard of RuO_2 (115.9 mV dec^{-1}).

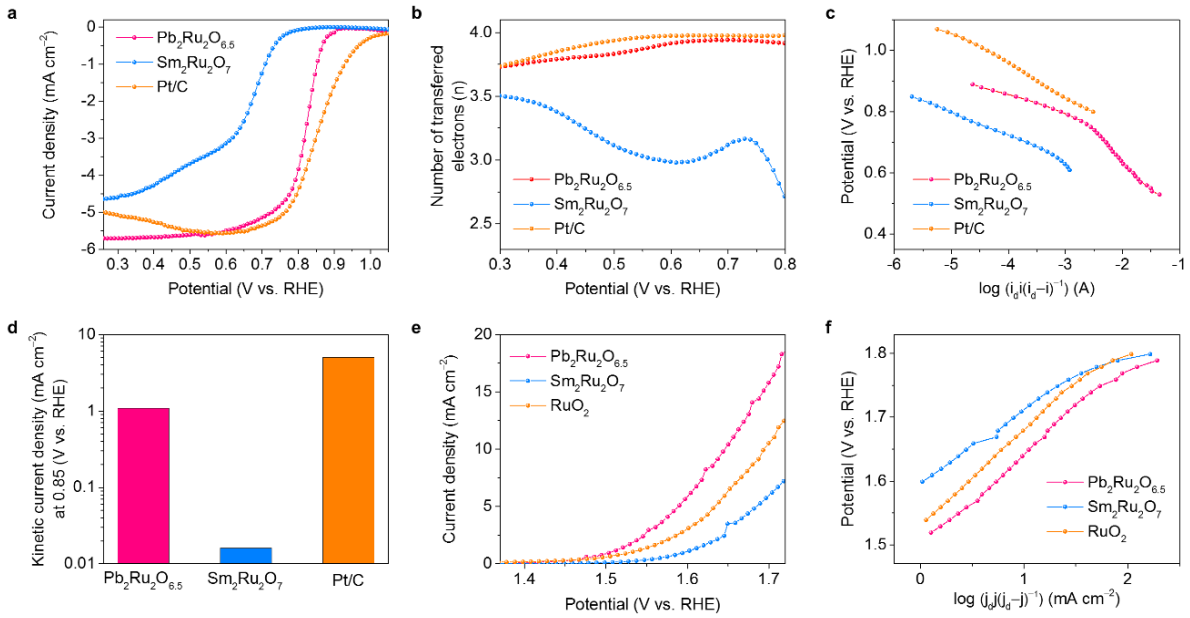

Figure 30. Electrocatalytic activities for ORR and OER on the highly pure single crystalline pyrochlore oxide nanoparticles ($A_2B_2O_{7-x}$, A = Pb and Sm, B = Ru). (a) Linear scan voltammogram (LSV) curves and (b) the number of transferred electrons in O_2-saturated 0.1 M KOH at a rotation speed of 1,600 rpm and scan rate of 10 mV s^{-1} for $Pb_2Ru_2O_{6.5}$, $Sm_2Ru_2O_7$ and Pt/C at a rotating ring-disk electrode (RRDE). (c) Tafel plots of log I_k (A) vs. E (V vs. reversible hydrogen electrode (RHE)) for the pyrochlore catalysts and Pt/C at the potential range for the ORR. In (c), the limiting current density obtained at potential = 0.35 V was used to calculate i_k using the equation, $i_k = i_L \bullet i/(i_L - i)$. (d), Kinetic current density of the pyrochlore oxides and Pt/C at 0.85 V. (e) LSV curves of the pyrochlore oxides and RuO_2. (f) Tafel plots of log J_k (mA cm^{-2}) vs. E (V vs. RHE) for the pyrochlore oxides and RuO_2 at the potential range for the OER.

Table 7. Tafel slopes (mV dec^{-1}) of the pyrochlore oxide catalysts and Pt/C for the ORR at different voltages.

Catalysts	Slope at low ŋ (mV dec^{-1})	Slope at high ŋ (mV dec^{-1})
$Pb_2Ru_2O_{6.5}$	56	126
$Sm_2Ru_2O_7$	62	125
Pt/C	60	120

Table 8. Electrocatalytic activities of the pyrochlore oxide catalysts and reported metal-oxide based electrocatalysts for ORR in O_2-saturated 0.1 M KOH. Abbreviation of Ketjenblack, acetylene black and carbon black are KB, AB and CB, respectively.

Catalysts	Loading (mg cm^{-2}) /Rotation rate (rpm)	Onset Potential (V vs. RHE)	Half-wave Potential (V vs. RHE)	Current Density (mA cm^{-2}) @ ~ (vs. RHE)	Reference
$Pb_2Ru_2O_{6.5}$ /KB	**0.637 /1600**	**0.89**	**0.81**	**–1.28 @ 0.85 V**	**This work**
$Sm_2Ru_2O_7$ /KB	**0.637 /1600**	**0.78**	**0.65**	**–0.01 @ 0.85 V**	**This work**
20% Pt/C	**0.319 /1600**	**1.08**	**0.85**	**–3.02 @ 0.85 V**	**This work**
$LaCu_{0.5}Mn_{0.5}O_3$ /AC	0.3	0.85	n/a	n/a	Nat. Chem. **2011**, 3, 546
$LaMnO_3$ /AC	0.3	0.87	0.66	–0.02 @ 0.85 V	Nat. Chem. **2011**, 3, 546
$LaCoO_3$ /AC	0.3	0.83	0.67	–0.03 @ 0.85 V	Nat. Chem. **2011**, 3, 546
$LaSrMnO_3$	n/a	0.88	n/a	n/a	Energy Environ. Sci. **2013**, 6, 1582
BSCF-5528_Ar /KB	0.639 /1600	0.76	0.63	0.0375 @ 0.85 V	Adv. Energy Mater. **2015**, 5, 1501560
BSCF-5582_Ar /KB	0.639 /1600	0.75	0.62	–0.256 @ 0.85 V	Adv. Energy Mater. **2015**, 5, 1501560
$La_{0.7}$-50 nm /KB	0.64 /1600	0.77	0.68	–0.163 @ 0.85 V	Energy Environ. Sci. **2016**, 9, 179
$Pb_2Ru_2O_{7-x}$ /CB	0.5 /3600	0.89	0.73	–0.383 @ 0.85 V	J. Electrochem. Soc. **2015**, 162, 129

Table 9. Electrocatalytic activities of the pyrochlore oxide catalysts and reported metal-oxide based electrocatalysts for OER in O_2-saturated 0.1 M KOH.

Catalysts	Loading ($mg\ cm^{-2}$) /Rotation rate (rpm)	Potential (V vs. RHE) @ 2.5 $mA\ cm^{-2}$	Current density ($mA\ cm^{-2}$) @ ~ (vs. RHE)	Reference
$Pb_2Ru_2O_{6.5}$ /KB	**0.637 /1600**	**1.56**	**6.2 @ 1.6 V**	**This work**
$Sm_2Ru_2O_7$ /KB	**0.637 /1600**	**1.67**	**1.44 @ 1.6 V**	**This work**
IrO_2 /KB	**0.637 /1600**	**1.61**	**3.26 @ 1.6 V**	**This work**
De-$LiCo_{0.33}Ni_{0.33}Fe_{0.33}O_2$ /CB	0.1	1.52	10 @ 1.55 V	Nat. Commun. **2014**, 5, 4345
BSCF-5528_Ar /KB	0.639 /1600	1.62	2.1 @ 1.6 V	Adv. Energy Mater. **2015**, 5, 1501560
BSCF-5582_Ar /KB	0.639 /1600	1.71	2.0 @ 1.6 V	Adv. Energy Mater. **2015**, 5, 1501560
BSCF-5582_O_2 /KB	0.64 /1600	1.69	0.78 @ 1.6 V	Adv. Mater. **2015**, 27, 266
BSCF-5582 /KB	0.64 /1600	1.77	0.45 @ 1.6 V	Adv. Mater. **2015**, 27, 266
$La_{0.7}$–50 nm /KB	0.64 /1600	1.54	10 @ 1.8 V	Energy Environ. Sci. **2016**, 9, 179
$Pb_2Ru_2O_{6.5}$	0.2 /1600	1.41	28 @ 1.5 V	J. Mater. Chem. A. **2015**, 3, 10819
$Bi_{2.4}Ru_{1.6}O_7$	0.2 /1600	1.53	9.1 @ 1.6 V	J. Mater. Chem. A. **2015**, 3, 10819

Table 10. Tafel slopes (mV dec^{-1}) of the pyrochlore oxide catalysts and RuO_2 for the OER at different voltages.

Catalysts	Average slope (mV dec^{-1})
$Pb_2Ru_2O_{6.5}$	114.2
$Sm_2Ru_2O_7$	100.8
RuO_2	115.9

Figure 31a shows a schematic representation of *in situ* XAS electrochemical cell used for real-time investigation of the electron configurations and local structures of ruthenium in the pyrochlore catalysts during ORR and OER. The normalized ruthenium K-edge XANES spectra of Ru metal, RuO_2 and the pyrochlore catalysts are shown in **Figure 31**b, which can initially explain the correlation between catalytic activity and the intrinsic electron configuration of ruthenium. In $Pb_2Ru_2O_{6.5}$, two distinct-peaks were observed at photon energies of 22,140 and 22,150 eV. This split maximum was caused by the dipole-allowed transition from ruthenium 1s to bound 5p states and continuum 5p states, respectively.[144, 145] On the other hand, $Sm_2Ru_2O_7$ showed two overlapping-peaks at photon energies of 22,135 and 22,145 eV. Furthermore, **Figure 31**c shows the oxygen K-edge XANES spectra, in which the spectra are categorized into two types of pyrochlore catalysts, similar to the ruthenium K-edge XANES results. The double peaks at 525 and 529 eV were assigned to the number of holes in the t_{2g} and e_g orbitals of the ruthenium 4d states that originated from hybridization between ruthenium 4d and oxygen 2p, respectively.[146, 147] The intensity ratio of the t_{2g} and e_g orbitals was 2:4 for both pyrochlore oxides, corresponding to low spin states of ruthenium orbital. Based upon the chemical composition of the pyrochlore catalysts, the electronic configurations of ruthenium are estimated as $4d^{4.5}$ ($t_{2g}^{4.5}e_g^0$) for $Pb_2Ru_2O_{6.5}$ and $4d^4$ ($t_{2g}^4e_g^0$) for $Sm_2Ru_2O_7$ with low spin states in common. The absolute intensity of $Pb_2Ru_2O_{6.5}$ was higher than $Sm_2Ru_2O_7$, meaning more covalent Ru-O bonding characteristic because the higher bond covalency leads to more hole density in oxygen 2p orbital by stronger hybridization between ruthenium 4d and oxygen 2p orbitals. It could be explained by Fermi energy (E_F) differences between the e_g states of the ruthenium 4d (ca. 5 eV) and A-site metal states (ca. 6 eV). For instance, the E_F of the lead 6p states (near to ruthenium 4d) are significantly lower than those of the samarium 4f states (far from ruthenium 4d).[148] According to dynamic mean field theory (DMFT), there were quasiparticle (QP) peaks in $Pb_2Ru_2O_{6.5}$ that were attributed to low electron-electron correlation in the t_{2g} states of ruthenium 4d. However, $Sm_2Ru_2O_7$ did not show QP peaks, resulting from obvious splitting of the Hubbard band due to high electron-electron correlation in the ruthenium 4d states.[149] Therefore, these differences were caused by the splitting degree of the Hubbard bands to upper and lower levels by the QP band at the E_F near the ruthenium 4d states,[150] which made $Pb_2Ru_2O_{6.5}$ good conductors and $Sm_2Ru_2O_7$ relative insulators.

Furthermore, to quantify the covalency of Ru-O bond on the surface of the pyrochlore catalysts, we calculated a degree of covalency using an equation of absorbance/($hole_{eg}$+1/4$hole_{t2g}$) as shown in **Figure 31**d.[28] The excitations of oxygen 1s → ruthenium 4d – oxygen 2p bands in pre-edge of oxygen K-edge spectra can be assigned to the absorbance of ruthenium covalency, and it was calculated by subtracting the integrated area of the fitted linear background from that of the pre-edge peak. Normalization of the integral by ($hole_{eg}$+1/4$hole_{t2g}$) gave excellent agreement with the expected trends

in a previous study.[151] The normalization factor is based on the assumption of a 2-fold higher transfer integral of the e_g symmetry states as compared to the t_{2g} states due to the angular overlap with the ligand field. This would lead to about 4 times higher holes in the e_g states of the oxygen K-edge spectral intensity than that of the t_{2g} states. The quantified covalency values for $Pb_2Ru_2O_{6.5}$ and $Sm_2Ru_2O_7$ were around 0.65 and 0.39, respectively. These results implied that the surface of the metallic $Pb_2Ru_2O_{6.5}$ demonstrated the stronger covalency of Ru-O bond than that of the insulating $Sm_2Ru_2O_7$, resulting in highly enhanced electrochemical performances. It might be attributed to the enhanced kinetics of O^{2-}/OH^- exchange on the surface ruthenium ions and the deprotonation of the oxyhydroxide group to form peroxide ions, which were considered as the RDSs in the ORR and OER, respectively.[64, 66]

It could be also explained by the difference of Pauling electronegativity between Ru (2.2) and A-site cations of Pb (2.33) and Sm (1.17), respectively. Namely, chemical bonding nature of Ru-O-Ru/Pb with similar electronegativity values is much more covalent than that of Ru-O-Ru/Sm bonding. The fact means that the electrons in bonding character of Ru-O-Ru/Pb can be more delocalized through long-range order than that of Ru-O-Ru/Sm. Consequently, the freer charges of $Pb_2Ru_2O_{6.5}$ than relatively-trapped charges of $Sm_2Ru_2O_7$ can quickly respond to charge-transfer reaction during ORR and OER. This result was consistent to the electrochemical performances of the pyrochlore oxides. The significance of the results is that we first revealed the effect of covalency on ORR and OER activities in these pyrochlore oxides.

To identify structural stabilities on the basis of intrinsic Ru-O bonding characteristics in the pyrochlore catalysts during electrocatalysis, we carried out *in situ* XAS to investigate redox reactions around ruthenium. By using *in situ* XAS, we experimentally observed the redox reactions of ruthenium, resulting from changes in the distance between ruthenium and oxygen during electrocatalysis. **Figure 31**e shows the calculated interatomic distances for Ru-O bonds of the pyrochlore catalysts at various applied potentials during chronoamperometric tests (**Table 11 and 12**). The potential ranges for ORR and OER are 0.7–0.3 and 1.3–1.7 V, respectively (**Figure 33**). Going to both the ORR and OER potentials from open circuit, the interatomic distance of Ru-O bond for $Pb_2Ru_2O_{6.5}$ was slightly decreased from 1.967 Å to 1.948 Å (ORR at 0.3 V) and 1.953 Å (OER at 1.7 V), which is in good agreement with partial oxidation of ruthenium. In contrast, $Sm_2Ru_2O_7$ showed partially reduced ruthenium corresponding to increase of Ru-O bond distance from 1.988 Å to 2.001 Å (ORR at 0.3 V) and 2.004 Å (OER at 1.7 V). Note that $Pb_2Ru_2O_{6.5}$ and $Sm_2Ru_2O_7$ showed insignificant interatomic distance changes of Ru-O bonds (< 0.02 Å) in the ORR and OER potential regions, implying stable bulk structure of either pyrochlore oxide. The origin of significantly improved structural stabilities of the pyrochlore catalysts might be caused by the high crystallinity of the pure single crystalline nanoparticles.

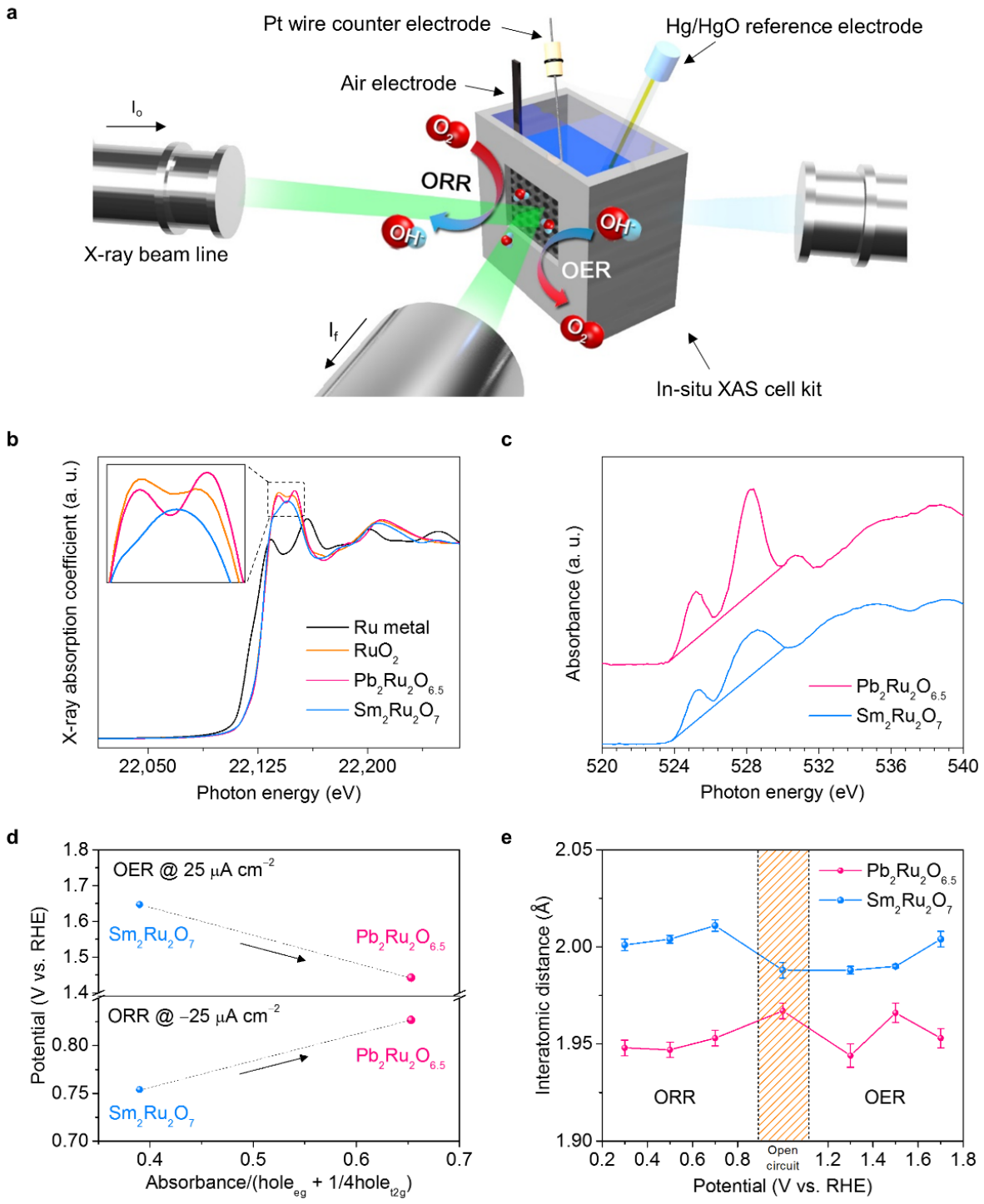

Figure 31. *Ex situ* XANES and *in situ* XAS analyses of the highly pure single crystalline pyrochlore oxide nanoparticles ($A_2Ru_2O_{7-x}$, A = Pb and Sm). (a) Schematic representation of *in situ* XAS design combined with XAS and a three-electrode half-cell. The half-cell consists of the pyrochlore oxide-based air electrode as the working electrode, Hg/HgO reference electrode and Pt wire as the counter electrode in 0.1 M KOH electrolyte. Incident X-rays (I_o) are absorbed by the pyrochlore oxide-based air electrode

and emit photons towards the fluorescence detector during the ORR and OER. (b) Normalized ruthenium K-edge XANES spectra for Ru metal, RuO_2, $Pb_2Ru_2O_{6.5}$ and $Sm_2Ru_2O_7$. (c) Normalized oxygen K-edge XANES total electron yield mode spectra for the pyrochlore catalysts. (d) Potentials at –25 and 25 μA cm^{-2} as a function of the Ru-O bonding covalency in the pyrochlore oxides for ORR and OER, respectively. (e) The corresponding interatomic distances for the reduced distances of the pyrochlore oxides at various applied potentials during electrocatalysis.

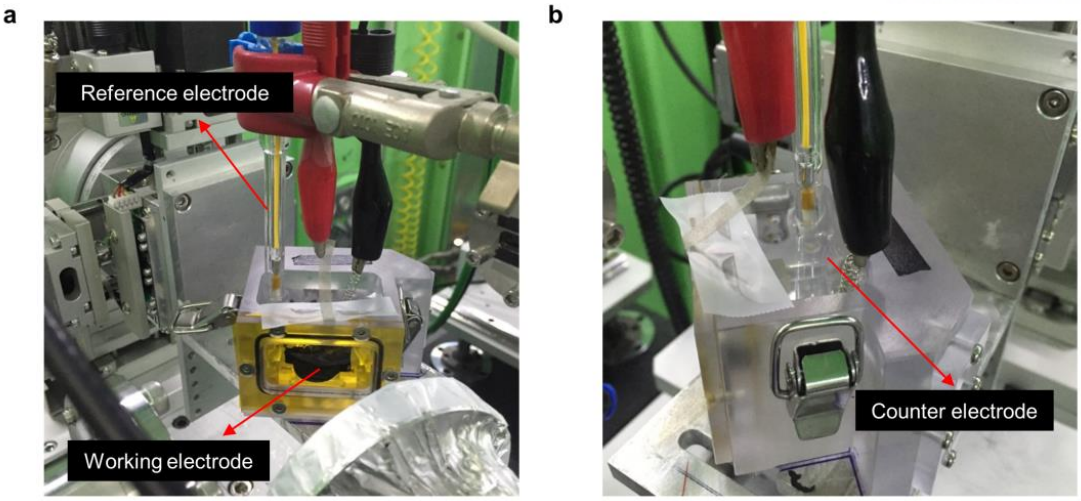

Figure 32. Photograph of three electrodes half-cell for *in situ* XAS analysis. The half-cell consists of the pyrochlore oxides based air electrode as working electrode, Hg/HgO reference electrode and Pt wire as counter electrode in 0.1 M KOH electrolyte.

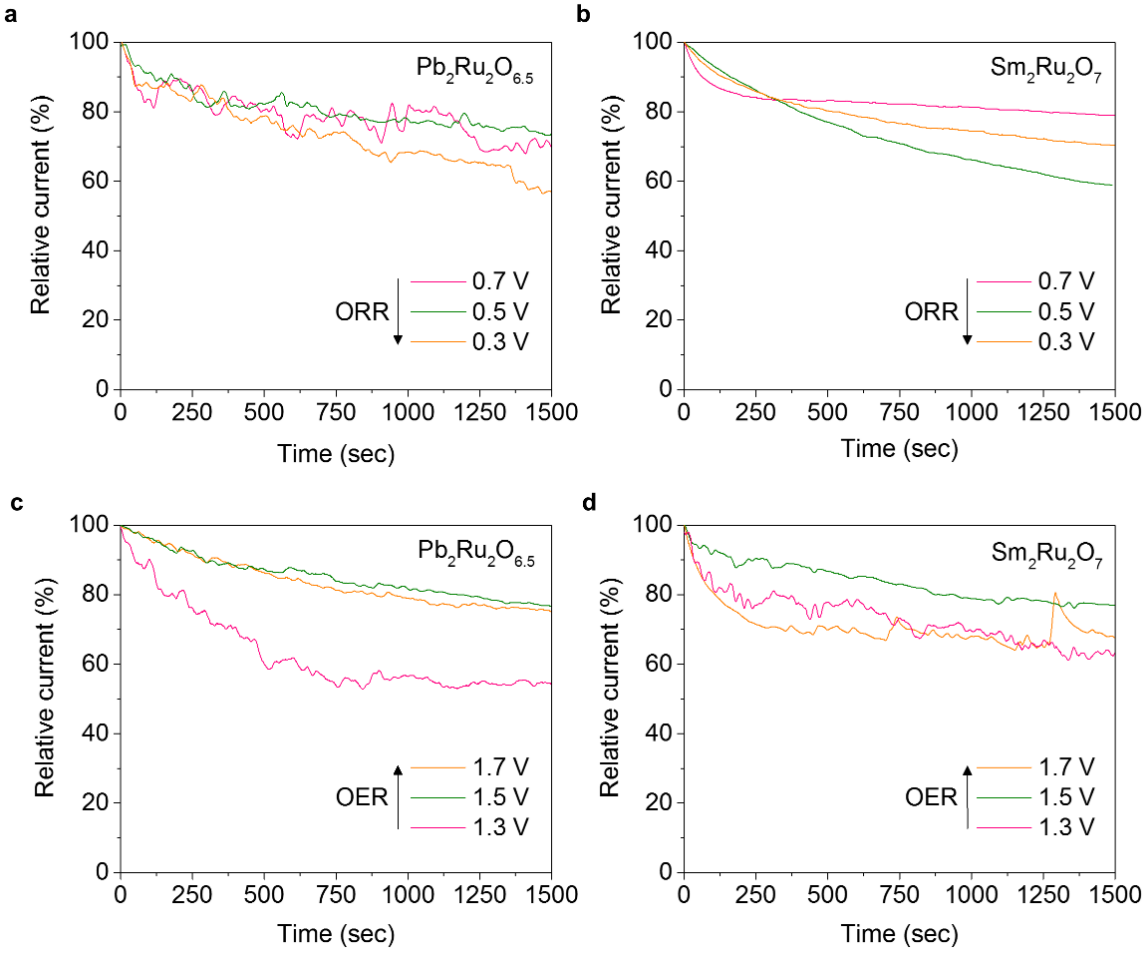

Figure 33. Chronoamperometric tests of (a) $Pb_2Ru_2O_{6.5}$ and (b) $Sm_2Ru_2O_7$ in 0.1 M KOH at 0.7 V, 0.5 V and 0.3 V (vs. RHE) for *in situ* XAS analysis during the ORR. Chronoamperometric tests of (c) $Pb_2Ru_2O_{6.5}$ and (d) $Sm_2Ru_2O_7$ in 0.1 M KOH at 1.3 V, 1.5 V and 1.7 V (vs. RHE) for *in situ* XAS analysis during the OER.

Table 11. EXAFS structural parameters of ruthenium K-edge k^3-weighted EXAFS spectra for $Pb_2Ru_2O_{6.5}$.

	Applied potential	Energy shift (eV)	Interatomic distance (Å)	Coordination number	Debye-Waller factor (x 10^{-3} Å^2)	R-factor*
Initial at OCV**		1.50 (±1.15)	1.967 (±0.004)	5.81 (±0.42)	3.05	0.018
ORR	0.7 V	-1.51 (±1.12)	1.953 (±0.004)	5.75 (±0.36)	3.05	0.015
	0.5 V	-2.84 (±1.13)	1.947 (±0.004)	5.81 (±0.36)	3.05	0.016
	0.3 V	-2.01 (±1.18)	1.948 (±0.004)	6.07 (±0.42)	3.05	0.019
OER	1.3 V	-2.77 (±1.78)	1.944 (±0.006)	5.24 (±0.48)	3.05	0.021
	1.5 V	1.77 (±1.21)	1.966 (±0.005)	5.74 (±0.42)	3.05	0.019
	1.7 V	-0.57 (±1.19)	1.953 (±0.005)	5.85 (±0.36)	3.05	0.022

* The Goodness of fit: $\sum\{Re\Delta\chi(\mathrm{k})^2 + Im\Delta\chi(\mathrm{k})^2\}11/\sum\{Re(\chi(\mathrm{k})_{\mathrm{data}})^2 + Im(\chi(\mathrm{k})_{\mathrm{data}})^2\}$.

** The value means pyrochlore electrode sample is wetted in 0.1M KOH solution at open-circuit voltage (OCV), i.e. without applied voltage.

Table 12. EXAFS structural parameters of ruthenium K-edge k^3-weighted EXAFS spectra for $Sm_2Ru_2O_7$.

	Applied potential	Energy shift (eV)	Interatomic distance (Å)	Coordination number	Debye-Waller factor (x 10^{-3} Å^2)	R-factor
Initial at OCV		-0.37 (±0.97)	1.988 (±0.004)	6.66 (±0.24)	2.70	0.011
ORR	0.7 V	4.78 (±0.73)	2.011 (±0.003)	5.58 (±0.24)	2.70	0.011
	0.5 V	3.43 (±0.43)	2.004 (±0.002)	5.46 (±0.12)	2.70	0.004
	0.3 V	2.93 (±0.87)	2.001 (±0.003)	5.64 (±0.18)	2.70	0.012
OER	1.3 V	0.97 (±0.61)	1.988 (±0.002)	5.52 (±0.24)	2.70	0.006
	1.5 V	1.46 (±0.36)	1.990 (±0.001)	6.18 (±0.12)	2.70	0.003
	1.7 V	3.89 (±0.96)	2.004 (±0.004)	4.92 (±0.30)	2.70	0.012

Using AUTOBK module in UWXAFS package,[1] the k^3-weighted Ru K-edge EXAFS spectra, $k^3\chi(k)$, have been obtained through background removal and normalization processes on the edge jump of ~ 22130 eV. In order to present effective radial distribution functions (RDF) for each sample during various electrocatalytic reactions, the $k^3\chi(k)$ spectra have been Fourier-transformed (FT) in the k range between 2.5 and 13.0 Å^{-1} The experimental Fourier-filtered $k^3\chi(k)$ spectra have been inversely Fourier-transformed with the *hanning* window function in the r space range between 1.0 and 2.0 Å. To determine the structural parameters for the first Ru-O bond pair, the curve-fitting process has been carried out by using the single bonding model. Theoretical scattering path of octahedral Ru-6O single shell has been calculated with FEFF8 code under the space group of *Fd-3m* for the well-known cubic pyrochlore model.[2, 3] In the EXAFS curve fitting process with FEFFIT module, total amplitude reduction factor, S_i^2, were fixed to 0.85 for the central Ru atom. The EXAFS structural parameters for each voltage-cutoff spectra, energy shift (ΔE), bond distance (R) and coordination numbers (N), have been determined with allowed R-factor value which is quality of the fit determined with $\sum\{Re\Delta\chi(\mathrm{k})^2 + Im\Delta\chi(\mathrm{k})^2\}/\sum\{Re(\chi(\mathrm{k})_{\mathrm{data}})^2 + Im(\chi(\mathrm{k})_{\mathrm{data}})^2\}$, where χ(k) is EXAFS-function) and $\Delta\chi$(k) means $\chi(\mathrm{k})_{\mathrm{data}} - \chi(\mathrm{k})_{\mathrm{best\text{-}fitted}}$. On the other hand, Debye−Waller factors (σ^2) for voltage-cutoff electrocatalytic reactions in each pyrochlore sample were fixed in the EXAFS fitting process.

In order to evaluate the activities of the pyrochlore catalysts, we performed primary and rechargeable Zn–air batteries tests. The discharge polarization curves of the pyrochlore catalysts and Pt/C were obtained by increasing the current density to 300 mA cm^{-2} (**Figure 34**a). Initially, commercial Pt/C showed the lowest overpotential of the pyrochlore catalysts. The electrochemical performance of $Pb_2Ru_2O_{6.5}$ was comparable to that of Pt/C at current densities of >125 mA cm^{-2}. $Pb_2Ru_2O_{6.5}$ showed the highest peak power density of 195 mW cm^{-2}, which was higher than that of Pt/C (188 mW cm^{-2}) (**Figure 34**b). For practical application, a current density of 20 mA cm^{-2} was chosen as the discharge rate of the primary Zn–air batteries containing the pyrochlore catalysts and Pt/C (**Figure 34**c). Pt/C showed the lowest overpotential and highest operating voltage at a current density of 20 mA cm^{-2}, which was in agreement with the results of the polarization test shown in **Figure 34**a. However, $Pb_2Ru_2O_{6.5}$ showed significantly improved durability over 330 min, although it showed a lower plateau voltage, than Pt/C. These results implied that the Zn–air battery containing $Pb_2Ru_2O_{6.5}$ could show highly stable discharge performance with high power density due to the strong covalency of ruthenium on the surface of the metallic pyrochlore oxide. The $Sm_2Ru_2O_7$ showed slightly degraded power densities, resulting from the weak covalency of ruthenium in the insulating pyrochlore oxides. These results correspond well with the order estimated from *in situ* XAS analysis.

Figure 34d shows the anodic and cathodic polarization curves of the rechargeable Zn–air batteries. On discharging, the mixture of Pt/C and IrO_2 showed the lowest overpotential of 0.2 V at a current density of 50 mA cm^{-2}. $Pb_2Ru_2O_{6.5}$ showed a similarly low overpotential (0.23 V). On charging, $Pb_2Ru_2O_{6.5}$ showed reliable bi-functional properties, with a substantially lower overpotential (0.52 V) than the mixture of Pt/C and IrO_2 (0.77 V). To explore the bi-functional catalytic properties, we performed short cycle period tests (600 s per cycle) at a current density of 10 mA cm^{-2}, which corresponded to a depth of discharge (DOD) of ≈1% (**Figure 34**e). We calculated the operating voltage differences between charge and discharge after 200 cycles ($\Delta\eta_{200}$) for 33 h. The mixture of Pt/C and IrO_2 showed $\Delta\eta_{200}$ of 1.05 V, implying a larger overpotential compared to $Pb_2Ru_2O_{6.5}$ (0.77 V). These results implied that the rechargeable Zn–air batteries containing the $Pb_2Ru_2O_{6.5}$ demonstrated superior electrochemical performance and durability compare to that of the state-of-the-art catalyst of $La_{0.7}$-BSCF5582 perovskite with larger overpotential (1.0 V @ 100 cycles).[65] Further, we increased the DOD to ≈7.5%, corresponding to a cycle period of 2 h, which was required to gain reliable rechargeability of the Zn–air batteries (**Figure 34**f). $Pb_2Ru_2O_{6.5}$ showed a lower difference of operating voltage between charge and discharge after 18 cycles ($\Delta\eta_{18}$ = 1.13 V) than the mixture of Pt/C and IrO_2 (1.42 V). The results were consistent with those obtained with a DOD of ≈1%, suggesting that the electrons were easily transferred through Ru in $Pb_2Ru_2O_{6.5}$. In contrast, $Sm_2Ru_2O_7$ showed slightly degraded overpotentials due to a lack of electron transport (**Figure 35**). We believe that these results correlate

with cycle durability in the electrochemical reactions. This is evidenced in the ruthenium K-edge EXAFS/XANES spectra and XRD patterns after 100 cyclic voltammogram (CV) for the pyrochlore catalysts, confirming that only the insulating $Sm_2Ru_2O_7$ was partially reduced because of lower electrochemical stability compared to the metallic $Pb_2Ru_2O_{6.5}$ (**Figure 36**).

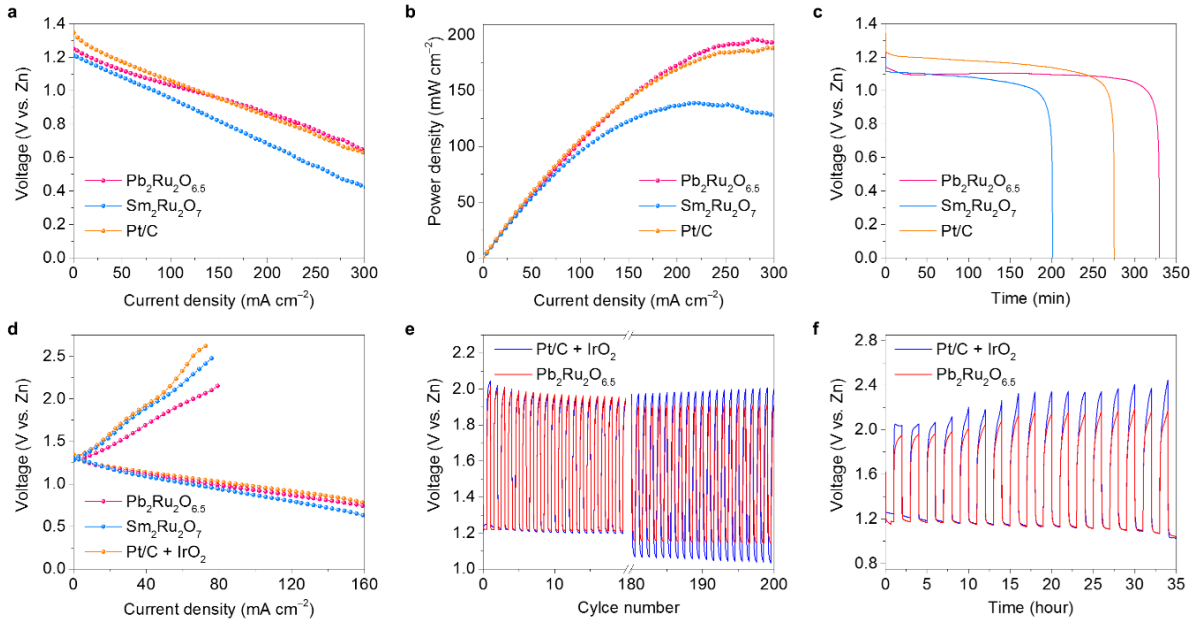

Figure 34. Performance of primary and rechargeable Zn–air batteries based on the highly pure single crystalline pyrochlore oxide nanoparticles ($A_2Ru_2O_{7-x}$, A = Pb and Sm). (a) Current density–voltage curves, (b) power–current density curves and (c) discharge curves at a current density of 20 mA cm^{-2} of primary Zn–air batteries using $Pb_2Ru_2O_{6.5}$, $Sm_2Ru_2O_7$ and Pt/C-based air electrodes as ORR catalysts. (d) Anodic and cathodic polarization curves of rechargeable Zn–air batteries with the pyrochlore oxide catalysts and mixture of Pt/C and IrO_2 catalyst. (e) Discharge and charge cycling curves of rechargeable Zn–air batteries based on $Pb_2Ru_2O_{6.5}$ and the mixture of Pt/C and IrO_2 at a current density of 10 mA cm^{-2} in short cycle periods (600 s per cycle) and (f) long cycle periods (2 h per cycle) with ambient air.

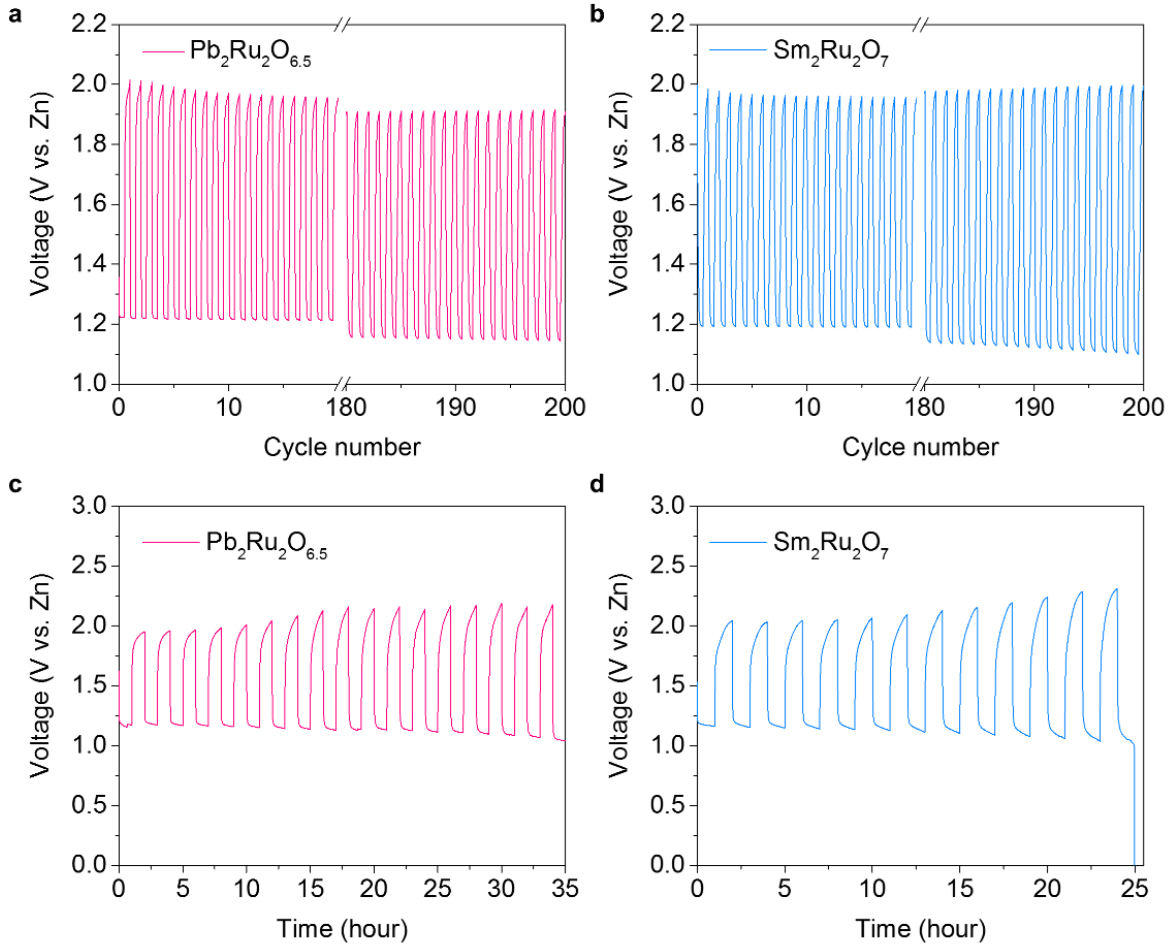

Figure 35. Discharge and charge cycling curves of rechargeable Zn–air batteries at the current density of 10 mA cm^{-2} in short cycle periods (600 sec per cycle) with ambient air based on (a) $Pb_2Ru_2O_{6.5}$ and (b) $Sm_2Ru_2O_7$. Discharge and charge cycling curves of rechargeable Zn–air batteries at the current density of 10 mA cm^{-2} in long cycle periods (2 h per cycle) with ambient air based on (c) $Pb_2Ru_2O_{6.5}$ and (d) $Sm_2Ru_2O_7$.

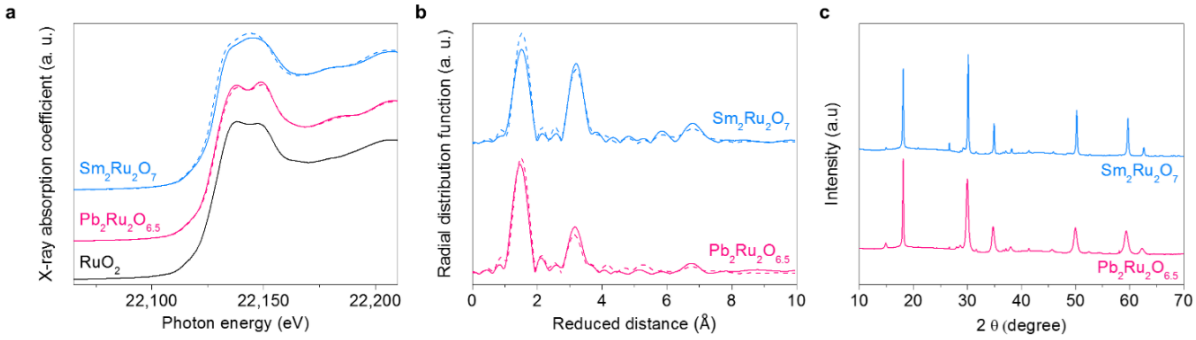

Figure 36. Durability tests of pyrochlore oxide catalysts. (a) Normalized ruthenium K-edge XANES for pristine (solid line) and 100th cycled (dashed line) pyrochlore catalysts. (b) Fourier-transformed radial distribution function of ruthenium K-edge EXAFS for pristine and 100th cycled pyrochlore catalysts. (c) XRD patterns for 100th cycled pyrochlore catalysts.

3.4 Summary

In this study, we have shown that highly efficient metallic pyrochlore oxide nanoparticles ($Pb_2Ru_2O_{6.5}$) exhibit outstanding activity as bi-functional electrocatalysts in aqueous Zn–air batteries for ORR and OER. Notably, the metallic $Pb_2Ru_2O_{6.5}$ demonstrated stronger covalency of ruthenium as compared to the insulating $Sm_2Ru_2O_7$, resulting in highly enhanced electrochemical performances for primary and rechargeable Zn-air batteries. Moreover, we provided experimental support for the structural stabilities of the pyrochlore oxides during ORR and OER by *in situ* XAS for the first time. The importance of the results reported herein is that the electrocatalytic activities of the pyrochlore oxides might be mainly attributed to the covalency of ruthenium, which explains the superior bi-functional activity of the metallic $Pb_2Ru_2O_{6.5}$.

Chapter 4

Unveiling the catalytic origin of nanocrystalline yttrium ruthenate pyrochlore as a bi-functional electrocatalyst for Zn−air batteries

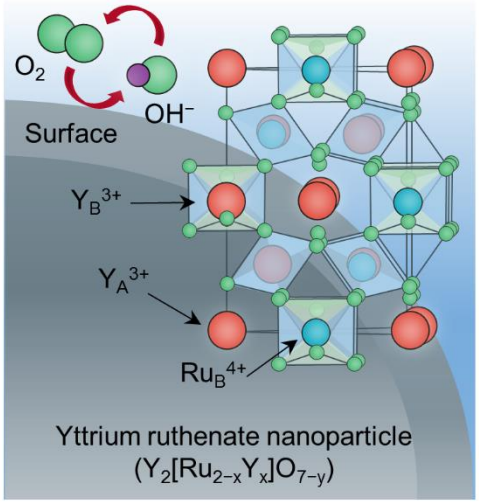

Zn–air batteries suffer from the slow kinetics of oxygen reduction reaction (ORR) and/or oxygen evolution reaction (OER). Thus, the bi-functional electrocatalysts are required for the practical application of rechargeable Zn–air batteries. In terms of the catalytic activity and structural stability, pyrochlore oxides ($A_2[B_{2-x}A_x]O_{7-y}$) have emerged as promising candidates. However, a limited use of A-site cations (e.g., lead or bismuth cations) of reported pyrochlore catalysts have hampered broad understanding of their catalytic effect and structure. More seriously, the catalytic origin of the pyrochlore structure was not clearly revealed yet. Here, we report the new nanocrystalline yttrium ruthenate ($Y_2[Ru_{2-x}Y_x]O_{7-y}$) with pyrochlore structure. The prepared pyrochlore oxide demonstrates comparable catalytic activities in both ORR and OER, compared to that of previously reported metal oxide-based catalysts such as perovskite oxides. Notably, we first find that the catalytic activity of the $Y_2[Ru_{2-x}Y_x]O_{7-y}$ is associated with the oxidations and corresponding changes of geometric local structures of yttrium and ruthenium ions during electrocatalysis, which were investigated by *in situ* X-ray absorption spectroscopy (XAS) in real-time. Zn–air batteries using the prepared pyrochlore oxide

achieve highly enhanced charge and discharge performance with a stable potential retention for 200 cycles.

This chapter has been published.

Park J., Park M., Nam G., Kim M. G.*, Cho J.* "Unveiling the catalytic origin of nanocrystalline yttrium ruthenate pyrochlore as a bi-functional electrocatalyst for Zn-air batteries", *Nano Lett.*, 17, 3974-3981 (2017).

4.1 Introduction

Zn–air batteries are receiving intense interest as the most promising electrical energy storage (EES) systems because of its high specific energy density (ca. 1,084 Wh kg^{-1}), high safety with aqueous electrolytes and low cost of zinc metal anode.[1, 5, 10, 152, 153] However, there are limitations arising from the slow kinetics of oxygen reduction reaction (ORR) and oxygen evolution reaction (OER).[12, 42] To date, a wide range of bi-functional electrocatalysts including metal oxide-,[64, 66, 131] metal alloy-,[154] non-precious metal-[155] and metal free-based materials[132] have been reported for rechargeable Zn–air batteries. In terms of the catalytic activity and structural stability, metal oxides have been considered as the most promising candidates, demonstrating comparable electrochemical performances with that of the state-of-the-art Pt/C and IrO_2 catalysts for ORR and OER, respectively.[120, 128]

To date, pyrochlore oxides ($A_2[B_{2-x}A_x]O_{7-y}$) have been intensively studied as bi-functional oxygen electrocatalysts among a variety of metal oxides for achieving both high ORR and OER activities.[141, 156] For example, $Pb_2[Ru_{2-x}Pb_x^{4+}]O_{6.5}$, $Pb_2[Ir_{2-x}Pb_x]O_{7-y}$ and $Bi_2[Ru_{2-x}Bi_x]O_{7-y}$ exhibited substantially enhanced electrochemical performance because of the high charge transfer through the oxygen vacancies.[80, 138] It is reasonable to expect that a higher concentration of oxygen defects could improve the ORR and OER activities.[73] However, the use of A-site cations of previous examples were still limited to divalent lead or trivalent bismuth ions, thus resulting in poor understanding of the pyrochlore structure.[140, 142] For broad applications, the new approach using other A-site cations should be studied to identify the catalytic origin of the pyrochlore structure. Accordingly, trivalent yttrium ions can be considered as A-site cations of the pyrochlore oxide because of the similar ionic radius with that of divalent lead or trivalent bismuth ions.[157] On the basis of the Mott-Hubbard mechanism, the electrical behavior of the pyrochlore oxide is determined by the Ru-O-Ru bond angle, which corresponds with the size of A-site cations.[158, 159] In this regard, the development of yttrium ruthenate ($Y_2[Ru_{2-x}Y_x]O_{7-y}$) as a new electrocatalyst is needed for an extensive understanding of pyrochlore structure.

More seriously, the catalytic origin of the pyrochlore structure was not clearly revealed yet. In terms of the charge transfer of electrocatalysts upon cycling, it is expected that it might be associated with redox reactions of the pyrochlore oxides. However, the limited *in situ* experimental measurement that combined structural and electrochemical analysis have hampered exploring the charge transfer reactions. Recently, *in situ* X-ray absorption spectroscopy (XAS) have been suggested to investigate the electron configurations and geometric local structures of the electrocatalysts in real-time.[151, 160] The reported *in situ* XAS can be classified into two types based on the measurement processes; that is, temperature-controlled synthesis or electrochemical analysis. Sa *et al.* carried out *in situ* XAS to confirm the formation of catalytic active sites of the Fe-N/C catalyst during annealing process.[161] They discovered that the higher density of $Fe\text{-}N_x$ sites could improve that of ORR activity. Moreover, Gorlin *et al.*

investigated the redox reactions of the MnO_x catalyst during electrocatalysis by *in situ* XAS.[162] However, the fundamental studies of highly improved ORR and OER activities for the metal oxides (e.g., perovskite, pyrochlore oxides) have been rarely reported, thus leading poor understanding of the catalytic reactions of the cubic oxide structures.

Herein, we report the yttrium ruthenate nanoparticles ($Y_2[Ru_{2-x}Y_x]O_{7-y}$) with pyrochlore structure as bi-functional oxygen electrocatalysts for Zn–air batteries. The $Y_2[Ru_{2-x}Y_x]O_{7-y}$, hereafter referred to as a YRO, has never been studied as an electrocatalyst for ORR and/or OER. The prepared YRO exhibited comparable catalytic activities in both ORR and OER, compared to that of previously reported metal oxide-based catalysts such as perovskite oxides. To reveal the mechanism for improved YRO catalytic activity, we carefully investigated the electron configurations and geometric local structures of yttrium and ruthenium ions during electrocatalysis by *in situ* XAS. Interestingly, the oxidation states of both of these cations were apparently increased, which could easily transfer charges by donating electrons. Moreover, primary and rechargeable Zn–air batteries by using the YRO demonstrated high capacity and stable potential retention during battery cycling, which could be ascribed to the significantly enhanced electrochemical performance.

4.2 Experimental detail

Preparation of yttrium ruthenate with pyrochlore structure: To prepare the YRO catalyst, a buffer solution was required. The buffer solution, NH_4–EDTA, was made with a mixture of 10 g anhydrous ethylenediaminetetraacetic acid (≥ 99% titration, Sigma-Aldrich), 1 M ammonia solution (28.0–30.0%, Samchun chemical) and 1.5 mL nitric acid (HNO_3, ACS regent 70%, Sigma-Aldrich) at a solution pH of 7. To prepare the YRO, 8.22×10^{-4} mol yttrium (III) acetate hydrate (99.9% metals basis, Sigma-Aldrich), 8.22×10^{-4} mol ruthenium (III) nitrosyl nitrate solution (1.5 wt% Ru, Sigma-Aldrich) and 10 g anhydrous citric acid (99%, Sigma-Aldrich) were dissolved and stirred with the buffer solution for 24 h at 150 °C. At this point, gelation was observed. The gelled solution was transferred to an oven at 200 °C for 6 h drying. The prepared powder was calcined in air at 1,050 °C for 5 h.

Preparation of the catalyst inks and working electrode: The catalyst inks were prepared with mixture of 16 mg of the YRO catalyst powder, 4 mg of ketjenblack carbon (EC 600JD), 200 μL of the 5wt% of Nafion in mixture of lower aliphatic alcohols and H_2O (Sigma-Aldrich) and 800 μL of ethanol. Briefly, the catalyst inks were prepared by ultrasonically mixing in distilled water for 1 h to make homogeneous mixture. The portion of 5 μL of inks were loaded on the glassy carbon of rotation ring disk electrode (RRDE) as the working electrode. The area of RRDE was 0.1256 cm^2. As a result, the loading level of the YRO was 0.637 mg_{cat} cm^{-2}. For the loading level of 79.6 μg_{pt} cm^{-2} benchmarking catalyst, 10 mg of Pt/C on Vulcan XC 72 (20wt%, Premetek Co.) was dispersed in 200 μL of the 0.05% titrated Nafion solution and 800 μL of ethanol. After that, this catalyst ink was prepared by ultrasonically mixing in distilled water for at least 1 h to make homogeneous ink. Then, 5 μL of ink was loaded on the glassy carbon of working electrode that the loading level of 20% Pt/C and the pure Pt were 0.398 $mg_{(20\% Pt/C)}$ cm^{-2} and 79.6 μg_{Pt} cm^{-2}, respectively.

Electrochemical measurements: A three-electrode cell was used to measure the electrocatalytic activities of the YRO catalyst. The rotating ring disk electrode (RRDE) (ALS Co., Ltd) test was carried out based on the YRO catalyst film (loaded on the glassy carbon of RRDE) for the working electrode in O_2-saturated 0.1 M KOH alkaline electrolyte. Platinum wire and Hg/HgO were used as the counter and reference electrodes, respectively. Electrochemical characterizations were conducted using a bipotentiostat (IviumStat). The scan rate of 10 mV s^{-1} was swept from 1.13 V to 0.26 V (vs. RHE) for oxygen reduction reaction (ORR) and from 1.23 to 1.82 V (vs. RHE) for oxygen evolution reaction (OER). The ORR capacitance were corrected by averaging current of cyclic voltammetry plots (CVs) in O_2- and Ar-saturated electrolytes. The OER CVs were capacitive-corrected by averaging current of the forward and backward sweeps. The capacitive-corrected ORR and OER currents were ohmically corrected with the measured ionic resistance (≈45 Ω).

In addition, a ring potential of 0.4 V (vs. Hg/HgO) was applied to oxidize peroxide during ORR. The collection efficiency (N) was determined under Ar atmosphere using 10 mM $K_3[Fe(CN)_6]$, which is around 0.41. This value is similar to the theoretical value of 0.42. The peroxide yield (H_2O^-) and the number of transferred electrons (n) were calculated from the below equations.

$$H_2O^-(\%) = 100\frac{2I_r/N}{I_d+I_r/N} \quad (1)$$

$$\mathrm{n} = 4\frac{I_d}{I_d+I_r/N} \quad (2)$$

Primary Zn–air batteries tests: For primary Zn–air batteries tests based on the YRO, 0.75 g of zinc granular is used as an anode and 200 μL of 6 M KOH was used as an electrolyte. A nylon membrane was used as a separator. The air-electrode which is a cathode was prepared by uniformly loaded gas diffusion layer (GDL) (the catalyst ink formulation: 16 mg of catalyst, 4 mg of ketjenblack, 200 μL of the 5wt% of the Nafion solution and 800 μL of ethanol on nickel mesh. Thickness of the electrode is around 500 μm. The assembled primary Zn-air batteries were tested at the discharge current densities of 20 mA cm^{-2}. The GDL was prepared from a mixture of activated charcoal (Darco G-60A, Sigma-Aldrich) and PTFE binder (60 wt% PTFE emulsion in water, Sigma-Aldrich) at a weight ratio of 7:3 with about 450 μm of thickness to ensure proper gas distribution and sufficient current collection. This prepared GDL was used as the reference for comparison to confirm enhanced performance of air-electrode based on catalysts in polarization curves of the Zn-air batteries.

Rechargeable Zn–air batteries tests: For rechargeable Zn–air batteries tests based on the YRO, 0.5 g of zinc plate is used as an anode and 2 mL of 6 M KOH with 0.2 M ZnO as an electrolyte. Preparation method of air-electrode with the catalysts is same as primary Zn–air batteries except nickel mesh. Thickness of the electrode is around 950 μm. In this case, nickel foam is used for air-electrode instead of mesh. The assembled rechargeable Zn–air batteries were tested at the discharge/charge current densities of 10 mA cm^{-2}.

Materials characterizations: The material morphologies were examined using SEM (VERIOS 460, FEI), high-resolution transmission electron microscopy (HR-TEM) (JEM-2100F, JEOL) operating at 200 kV. Powder analysis was performed using an X-ray diffractometer (XRD) (D/Max2000, Rigaku). X-ray absorption near edge structure (XANES) and extended X-ray absorption fine structure (EXAFS) were collected on BL10C beam line at the Pohang light source (PLS-II) with top-up mode operation under a ring current of 200 mA at 3.0 GeV.

4.3 Results and discussion

Figure 37a presents the synthetic procedure for the nanocrystalline pyrochlore oxide of YRO. The YRO was synthesized by a sol-gel method to uniformly crosslink the trivalent yttrium and tetravalent ruthenium ions. Accordingly, citric acid ($C_6H_8O_7$) was selected as a chelating agent and added into the precursor solution. Then, these well-crosslinked precursor particles were crystallized at an elevated temperature of 1,050 °C for obtaining single crystalline YRO nanoparticles. The cubic phase of the pyrochlore structure was clearly identified by X-ray diffraction (XRD) with space group of Fd-3m symmetry (**Figure 37**b). Notably, there were distinct peaks of the pyrochlore oxide for various planes without any shoulder peaks, resulting in highly pure and crystalline structure of the YRO. To verify the morphology of the YRO, the nanoparticles were subjected to scanning electron microscopy (SEM). Figure 1c shows the aggregated YRO secondary particles consisting of angular shaped primary particles. The average sizes of primary particles were around 200 nm (inset of **Figure 37**c).

To further clarify the structural integrity of the pyrochlore structure, the YRO nanoparticles were subjected to focused-ion beam (FIB) milling. The cross-sections of the particles were investigated by high-angle annular dark field scanning TEM (STEM-HAADF) and energy-dispersive X-ray spectroscopy (EDS), respectively (**Figure 37**d; **Figures 38, 39** and **Table 13**). These results imply that the YRO nanoparticles were successfully synthesized based upon homogenous distribution and stoichiometric ratio of trivalent yttrium and tetravalent ruthenium ions. The cubic phase of the YRO nanoparticles were further characterized by high resolution transmission electron microscopy (HR-TEM) and the corresponding fast Fourier transform (FFT) image, as shown in **Figure 37**e,f. The FFT pattern along the [110] main zone axis agreed perfectly with cubic phases of pyrochlore structure in accord with the unit spots of (–11–1) and (–111) with an axial angle of 70.53° (inset of **Figure 37**f). Moreover, the corresponding STEM-HAADF images clearly show that the lattice fringes with d-spacing values of 0.30 nm and 0.51 nm correspond to (111) and (002) crystal planes, respectively (**Figure 37**g,h). These results suggest that the YRO exhibited highly pure and crystalline nanoparticles with pyrochlore oxide structure.

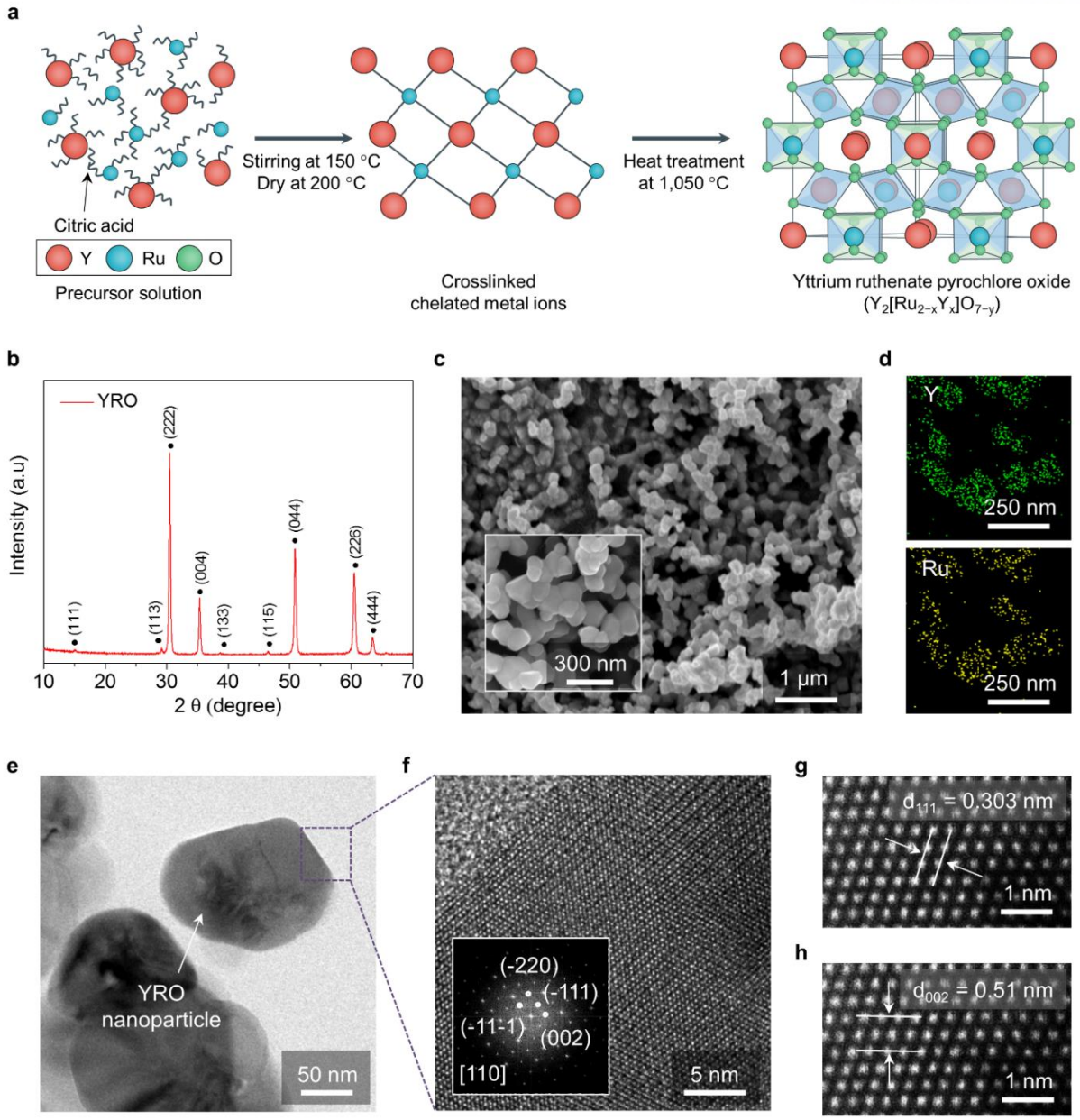

Figure 37. Preparation, morphology and structural characterization of nanocrystalline pyrochlore oxides ($A_2[B_{2-x}A_x]O_{7-y}$). (a) Schematic of the synthesis process of yttrium ruthenate nanoparticles ($Y_2[Ru_{2-x}Y_x]O_{7-y}$), hereafter referred to as a YRO, with pyrochlore structure by sol-gel method. They consist of trivalent yttrium (red sphere), tetravalent ruthenium (blue sphere), and divalent oxygen ions (green sphere) that bonds them together. (b) Powder XRD patterns of YRO nanoparticles. (c) SEM image of YRO, and inset showing the magnified image. (d) STEM-HAADF-EDS images of the YRO with elemental maps of yttrium and ruthenium. (e,f) The HR-TEM images of the YRO nanoparticles at (e) low and (f) high magnifications. The inset of (f) indicates the FFT pattern of HR-TEM for YRO along the [110] main zone axis. The indexed spots refer to the lattice planes of (–111), (–11–1), (002)

and (–220) in the pyrochlore structure. (g,h) The corresponding STEM-HAADF images of YRO with d-spacing values of (g) 0.30 nm and (h) 0.51 nm correspond to (111) and (002) crystal planes, respectively.

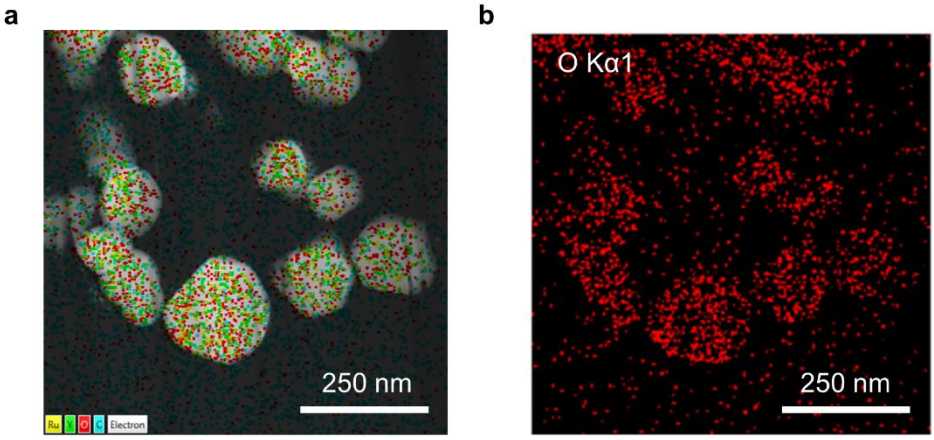

Figure 38. (a) STEM-HAADF-EDS images of the YRO and (b) elemental maps of oxygen.

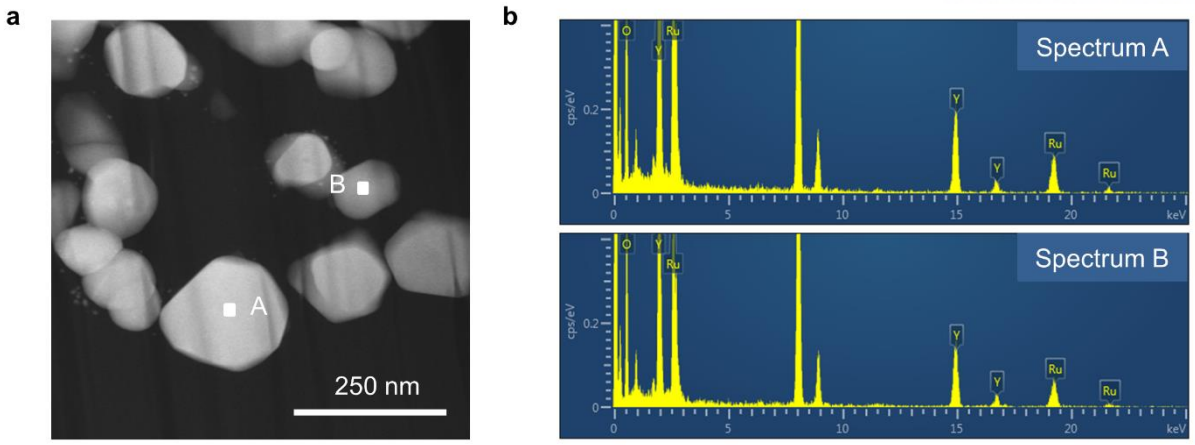

Figure 39. STEM-EDS of the YRO at different point.

Table 13. Percent composition and atomic ratios of yttrium and ruthenium in the YRO at different points (**Figure 39**).

Electrocatalysts	Sites	Y (wt%)	Ru (wt%)	Y/Ru (At. %)
YRO	A	35.53	41.16	0.98
	B	35.41	39.59	1.01

To investigate the electrocatalytic activity of the YRO, we performed the rotation ring disk electrode (RRDE) method. **Figure 40**a demonstrates the ohmic- and capacitive-corrected linear scan voltammogram (LSV) curves of the YRO and Pt/C for ORR activities. We observed that the value of onset potential in the YRO was ≈0.85 V vs. RHE at a current density of –0.15 mA cm_{disk}^{-2}, and Pt/C showed the onset potential of ≈1.06 V. The limiting current densities near 0.2 V were comparable between the YRO (–4.93 mA cm_{disk}^{-2}) and Pt/C (–5.03 mA cm_{disk}^{-2}). In terms of calculated number of transferred electrons, the YRO showed a value of ≈3.8, which is similar to that of Pt/C (≈4), and agrees well with the four-electron pathway for ORR (inset of **Figure 40**a; **Figure 41**). These values are comparable to those of the previously reported metal oxide-based bi-functional catalysts such as perovskite oxides, which could be ascribed to the significantly enhanced ORR activity of the YRO. In order to investigate the real catalytic activity of the YRO, the corresponding LSV curve was normalized by Brunauer-Emmett-Teller (BET) surface area (**Figure 42 and 43**). Moreover, the mass transfer-corrected Tafel plots indicated the kinetic reactions of the YRO and Pt/C for ORR (**Figure 44**). The average Tafel slope of the YRO was ≈59 mV dec^{-1} at low overpotential region similar to that of Pt/C (≈60 mV dec^{-1}); this implies that the formation of superoxide by a one electron transfer reaction ($O_{2[ads.]} + e^- \rightarrow O_{2[ads.]}^-$) is the rate determining step (RDS) in ORR.[116]

In addition, we intensively investigated the OER activities of the YRO, compared to IrO_2 as a reference sample (**Figure 40**b). The YRO showed lower overpotential (≈1.45 V) and higher current density (8.05 mA cm_{disk}^{-2} @ 1.7 V) than that of IrO_2, implying superior OER activity resulted in the significant improvement of bi-functional catalytic activities (inset of Figure 2b). The prepared YRO also exhibited comparable catalytic activities in OER, compared to that of state-of-the art reference of RuO_2 (**Figure 45**). In this regard, we calculated the turnover frequency (TOF), implying the number of evolved oxygen molecules from the metal site of the YRO per second. The YRO showed high TOF of 2.23×10^{-2} s^{-1} for yttrium and ruthenium ions at 1.7 V, respectively. Moreover, the normalized LSV curve of the YRO based upon the real surface area was measured for practical catalytic activity (**Figure 46**). With respect to the kinetic reactions, mass-corrected Tafel plots for OER were measured for the YRO and IrO_2 (**Figure 47**). The YRO exhibited a low Tafel slope of ≈112.4 mV dec^{-1} similar to that of IrO_2 (≈126.3 mV dec^{-1}), suggesting that the fundamental reaction mechanism for RDS in OER is the deprotonation of the oxyhydroxide group to form peroxide ions.[64, 66]

Furthermore, we carried out primary and rechargeable Zn–air batteries tests. **Figure 40**c shows discharge polarization curves of the YRO and Pt/C as increasing the current density to 300 mA cm^{-2}. Upon discharging, we observed that the value of operating potential of the YRO was ≈1.17 V, and Pt/C demonstrated the operating potential of ≈1.23 V at a current density of 25 mA cm^{-2}. In addition, the maximum peak power density of the YRO was ≈145 mW cm^{-2} at a current density of 200 mA cm^{-2}, and

Pt/C showed ≈188 mW cm^{-2} at a current density of 300 mA cm^{-2} (**Figure 48**). To demonstrate the practical applications of the Zn–air batteries, the primary Zn–air batteries containing the YRO and Pt/C were subjected to the discharge tests at a current density of 20 mA cm^{-2} (**Figure 40**d). Compared with the operating potential of Pt/C (≈1.19 V), the YRO represented similar value of ≈1.09 V after 50 min. Moreover, the discharge durations were comparable between the YRO (≈236 min) and Pt/C (≈275 min).

With respect to the bi-functional catalytic activities of the YRO, the rechargeable Zn–air batteries were subjected to the charge and discharge tests by increasing the current densities to 80 and 160 mA cm^{-2}, respectively (**Figure 40**e). The charge capacity of Zn–air batteries is different from that of discharging process because carbon is oxidized at the anodic potential, resulting in substantial degradation of the air-electrode.[163] Upon discharging, the YRO showed low potential difference between the cathodic current density of 0 and 50 mA cm^{-2} (≈0.22 V) comparable to that of the mixture of Pt/C and IrO_2 (≈0.2 V). Moreover, the potential difference during charging process was on average lower in the YRO compared to the mixture of Pt/C and IrO_2. Furthermore, we performed the charge and discharge cycling tests of Zn–air batteries to investigate the structural stability of the YRO. **Figure 40**f shows the cycling curves of rechargeable Zn–air batteries with short period (10 min per cycle) at a current density of 10 mA cm^{-2}. The corresponding depth of discharge (DOD) was ≈1%. Notably, the YRO showed lower value of the potential difference between charging and discharging processes after 200 cycles ($\Delta\eta_{200}$ ≈0.84 V) than that of the mixture of Pt/C and IrO_2 (≈0.97 V). Accordingly, the YRO achieved better potential retention for 200 cycles ($|\Delta\eta_{200} - \Delta\eta_{initial}|$ ≈0.1 V), which highly enhanced the structural stability comparable to those of the previously reported Zn–air batteries using metal oxides such as the perovskite oxide of $La_{0.7}$-BSCF5582. Moreover, the DOD was increased to ≈7.5% for practical rechargeability of Zn–air batteries (**Figure 49**). The corresponding potential difference of the YRO after 35 cycles ($\Delta\eta_{35}$ ≈1.19 V) was substantially lower than that of the mixture of Pt/C and IrO_2 (≈1.42 V), which was consistent with the results obtained from short period.

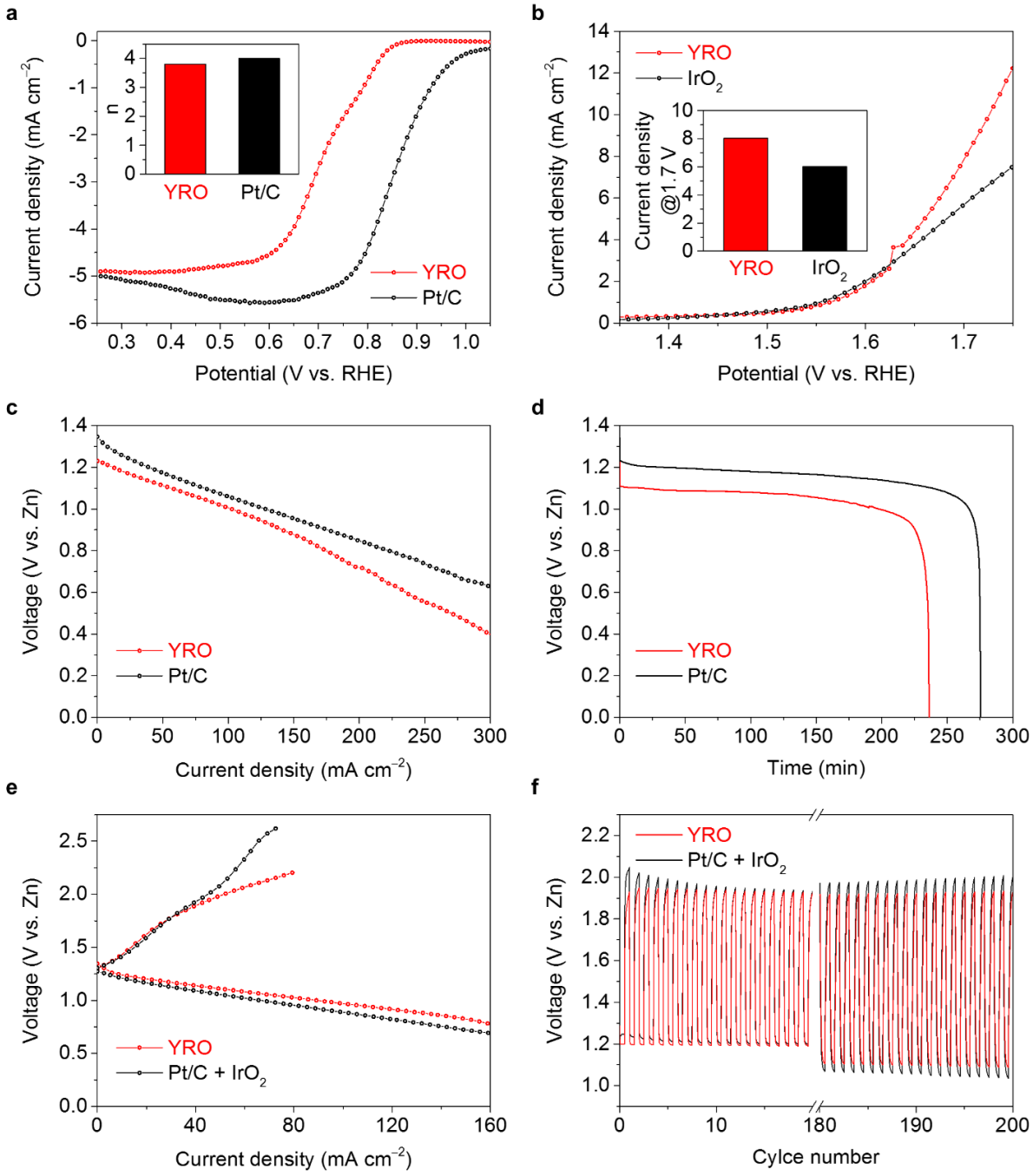

Figure 40. Electrocatalytic activities of the nanocrystalline YRO with pyrochlore structure. (a) Linear scan voltammogram (LSV) curves of the YRO and Pt/C during ORR, and inset showing the number of transferred electrons of the YRO and Pt/C. The electrochemical characterizations were performed using a rotation ring-disk electrode (RRDE) in O_2-saturated 0.1 M KOH at a rotation speed of 1600 rpm and scan rate of 10 mV s^{-1}. The ORR potential ranged from 1.13 to 0.26 V vs. RHE. (b) LSV curves of the YRO and IrO_2 during OER, and inset indicates the current density of the YRO and IrO_2 at a potential

of 1.7 V. The OER potential ranged from 1.23 to 1.82 V. (c) The current density–voltage curves and (d) discharge curves at a current density of 20 mA cm^{-2} of the primary Zn–air batteries using the YRO and Pt/C. (e) Anodic and cathodic polarization curves of the rechargeable Zn–air batteries using the YRO and the mixture of Pt/C and IrO_2. (f) The battery cycling curves of the rechargeable Zn–air batteries using the YRO and the mixture of Pt/C and IrO_2 during charging and discharging processes at a current density of 10 mA cm^{-2} in short cycle periods (10 min per cycle) with ambient air.

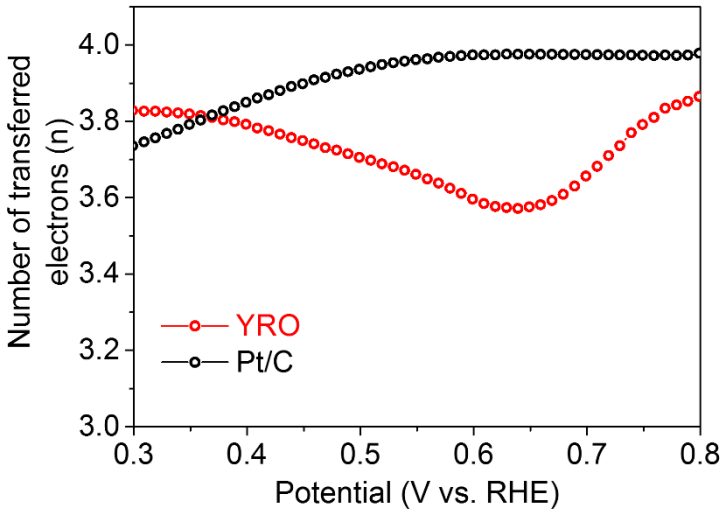

Figure 41. The number of transferred electrons (n) of the YRO and Pt/C during ORR.

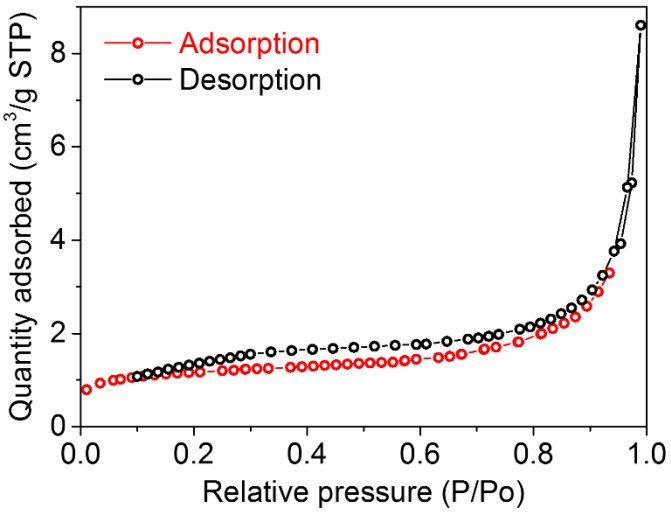

Figure 42. The nitrogen adsorption-desorption isotherm. The YRO showed a BET surface area of 4.2634 $m^2\ g^{-1}$.

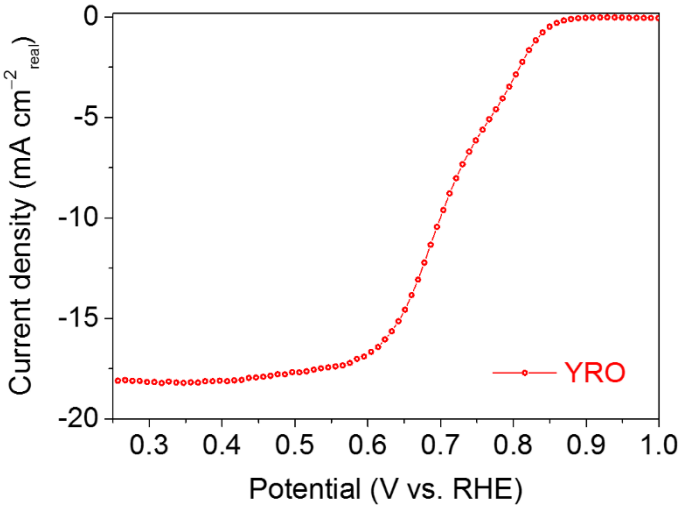

Figure 43. The normalized LSV curve of the YRO during ORR based upon the real surface area.

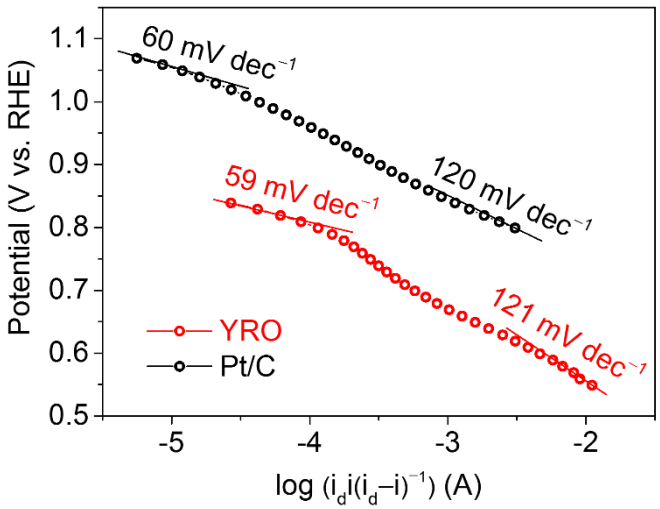

Figure 44. Tafel plots of log I_k (A) vs. E (V vs. RHE) for the YRO and Pt/C.

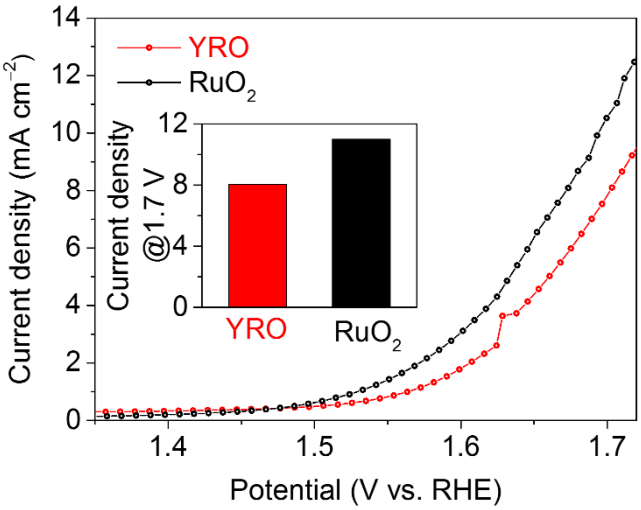

Figure 45. The LSV curves of the YRO and RuO_2 during OER.

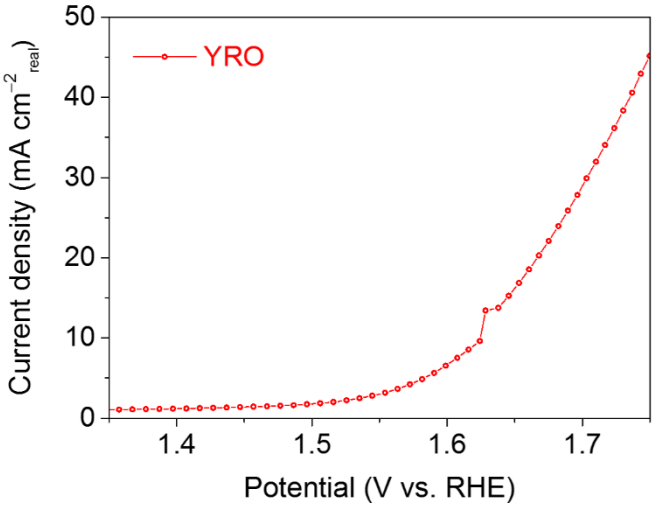

Figure 46. The normalized LSV curve of the YRO during OER based upon the real surface area.

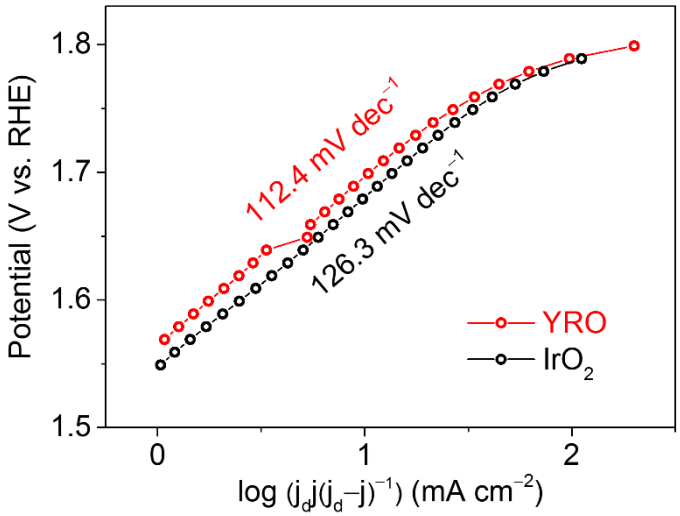

Figure 47. Tafel plots of log J_k (mA cm^{-2}) vs. E (V vs. RHE) for the YRO and IrO_2.

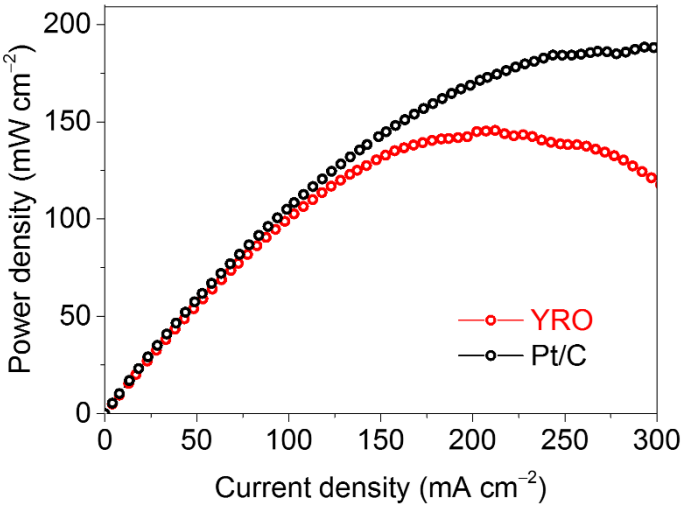

Figure 48. Power–current density of the primary Zn–air batteries using the YRO and Pt/C.

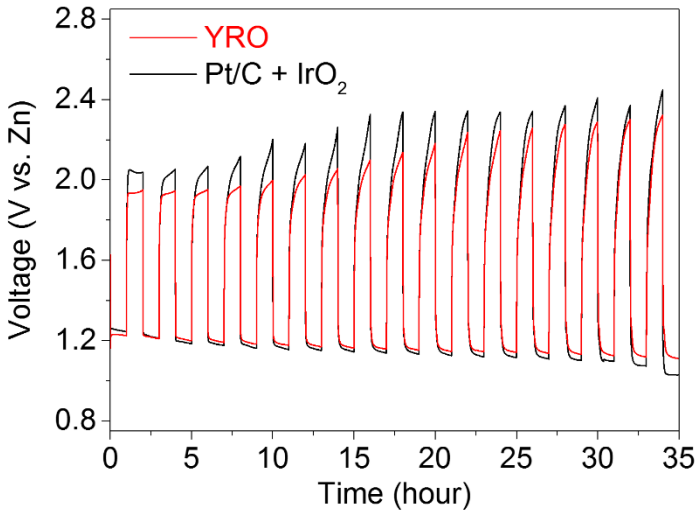

Figure 49. The battery cycling curves of the rechargeable Zn–air batteries using the YRO and the mixture of Pt/C and IrO_2 during charging and discharging processes at a current density of 10 mA cm^{-2} in long cycle periods (2 h per cycle) with ambient air.

In terms of the charge transfer of electrocatalysts upon battery cycling, the possible origin of the highly enhanced catalytic activities of the pyrochlore oxides is expected that it might be related to the redox reactions of A- and B-site cations during ORR and OER. To investigate the electron configurations and geometric local structures of yttrium and ruthenium ions of the YRO in real-time, we carried out *in situ* XAS. The *in situ* XAS electrochemical cell consists of three-electrode electrochemical cell and XAS instrument (**Figure 51**). The air electrode containing the YRO was subjected to the cyclic voltammetry (CV) test for yttrium and ruthenium ions with XAS measurements (**Figure 50**a). The CV during the ORR and OER was recorded between 0.23 and 1.43 V. **Figure 50**b,c show the normalized K-edge X-ray absorption near edge structure (XANES) spectra for ruthenium and yttrium ions of the YRO during electrocatalysis. We observed two overlapped-peaks of the ruthenium K-edge spectra at photon energies of 22,135 and 22,145 eV, implying the dipole-allowed transition from ruthenium 1s to 5p states with bound and continuum, respectively.[144, 145] Interestingly, these peaks were on average shifted to the higher values of the photon energy, indicating that the oxidation states of the ruthenium ions increased during ORR and OER (inset of **Figure 50**b,c). Moreover, the highest peak of the yttrium K-edge spectra was observed at a photon energy of 17,053 eV, which was assigned to the dipole-allowed transition from yttrium 1s to 5p states (**Figure 50**d,e).[164] Notably, the peak was apparently changed during ORR and OER, showing positive shift of the photon energy (inset of **Figure 50**d,e). This result suggests that the yttrium ions were generally oxidized during electrocatalysis, which was consistent with the ruthenium ions.

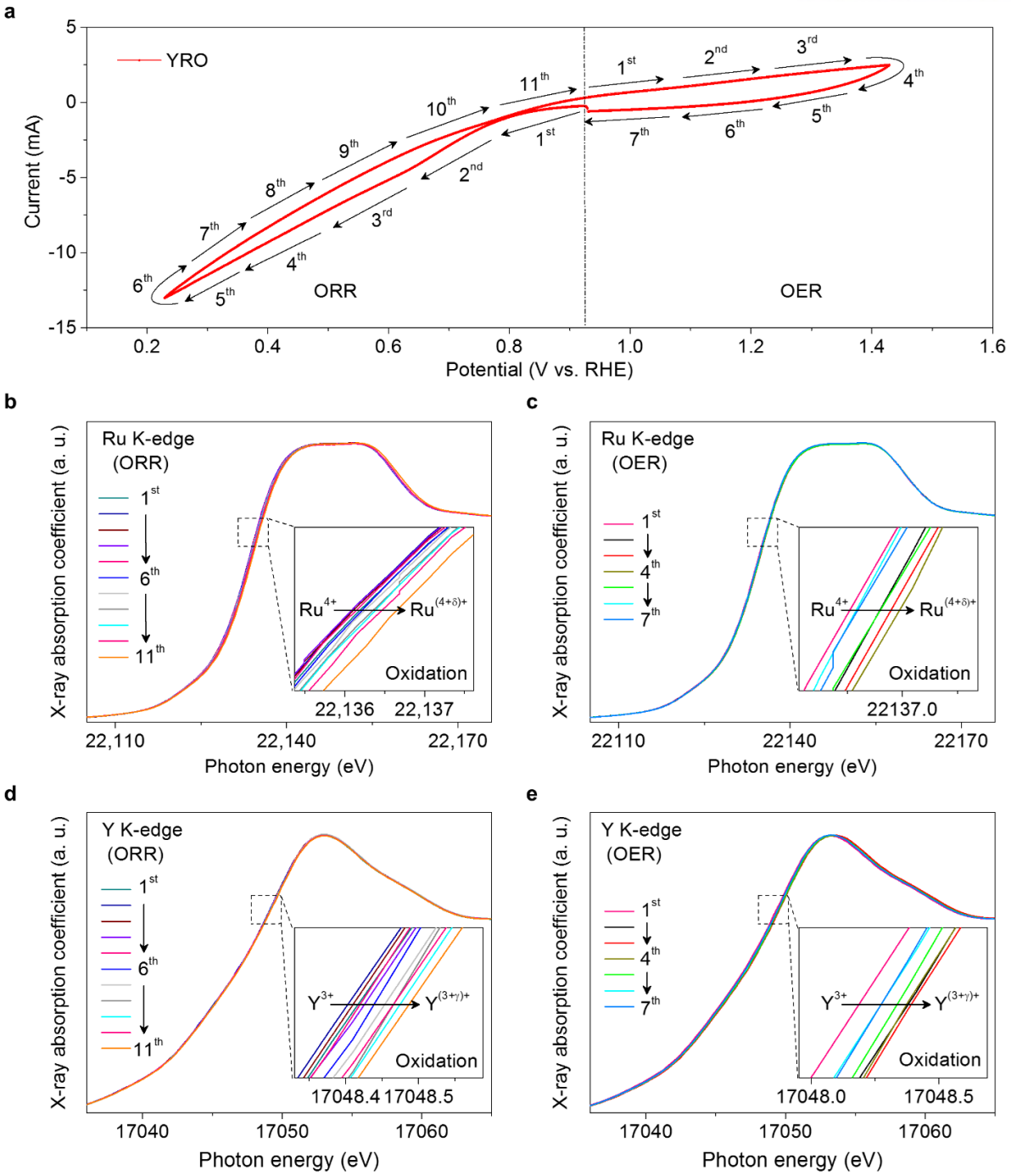

Figure 50. The X-ray absorption near edge structure (XANES) spectra of the nanocrystalline YRO with pyrochlore structure by *in situ* XAS analysis. (a) Cyclic voltammogram of the air electrode containing the YRO simultaneously with XAS analysis for yttrium and ruthenium cations. The scan rate of CV was 0.085 mV s^{-1}. The CV during the ORR and OER was recorded between 0.23 and 1.43 V vs. RHE. The corresponding ORR and OER potentials ranged from 0.93 to 0.23 and 1.43 V, respectively. The scan number of XAS analysis for ORR ranged from 1st to 11th, and OER ranged from 1st to 7th. (b,c)

Normalized ruthenium K-edge XANES spectra of the YRO simultaneously with CV test during (b) ORR and (c) OER, and insets showing the magnified data. (d,e) Normalized yttrium K-edge XANES spectra of the YRO during (d) ORR and (e) OER, and the insets indicate the magnified data.

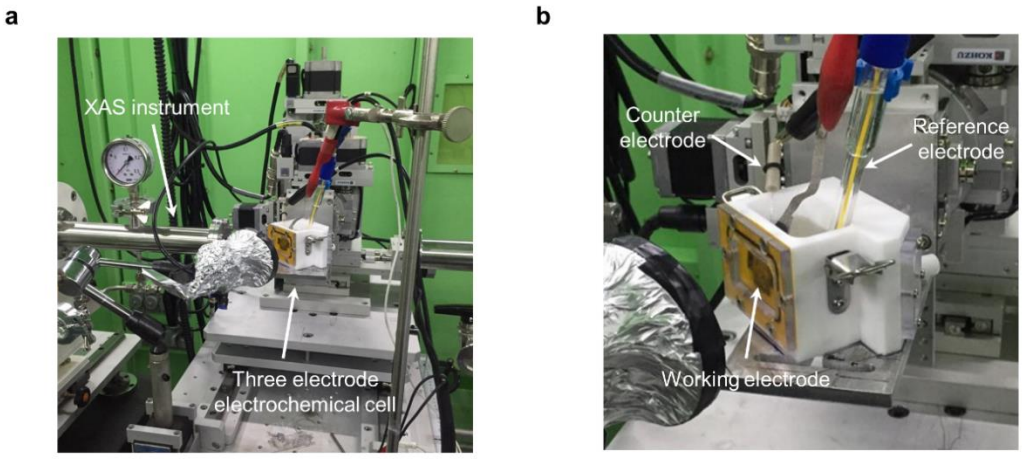

Figure 51. (a) Photograph of *in situ* XAS electrochemical cell consisting of three-electrode electrochemical cell and XAS instrument. (b) Photograph of the three-electrode electrochemical cell consisting of working electrode (air electrode), reference electrode (Hg/HgO electrode) and counter electrode (Pt wire).

To provide further insight into the effect of the geometric local structures on the catalytic activities of the YRO, we performed the extended X-ray absorption fine structure (EXAFS) analysis for both of these cations during ORR and OER. The EXAFS spectra were calculated by the general equation, which could be considered a variety of factors regarding the neighboring atoms.[165] As shown in **Figure 52**a,b, the corresponding radial distribution function (RDF) of Fourier-transformed k^3-weighted EXAFS spectra for ruthenium ions demonstrated the highest peak at reduced distances of around 1.6 Å, indicating Ru-O bonds at B-sites of the pyrochlore structure.[166] Notably, the reduced distances of Ru-O bonds remained constant (≈1.6 Å) upon cycling, whereas that of XANES spectra were changed, as discussed previously (insets of **Figure 52**a,b). This result could be explained by the high structural stability of the rigid RuO_6 structure in the pyrochlore oxide. Further, the EXAFS spectra for yttrium ions showed two distinct-peaks at reduced distances of around 2.0 and 1.6 Å, indicating Y-O bonds at A- and B-sites of the YRO, respectively (**Figure 52**c,d). These peaks confirmed that the chemical composition of the yttrium ruthenate nanoparticles were $Y_2[Ru_{2-x}Y_x]O_{7-y}$, resulting from the yttrium ions doping into B-sites of the YRO. The reduced distances of Y-O bonds at B-site were not changed (≈1.6 Å) during ORR and OER, which is consistent with that of Ru-O bonds (inset of **Figure 52**c,d). In contrast, the reduced distances of Y-O bonds at A-site were shifted negatively. This indicates that the oxidation states of yttrium ions were increased upon cycling, which agrees well with the XANES results.

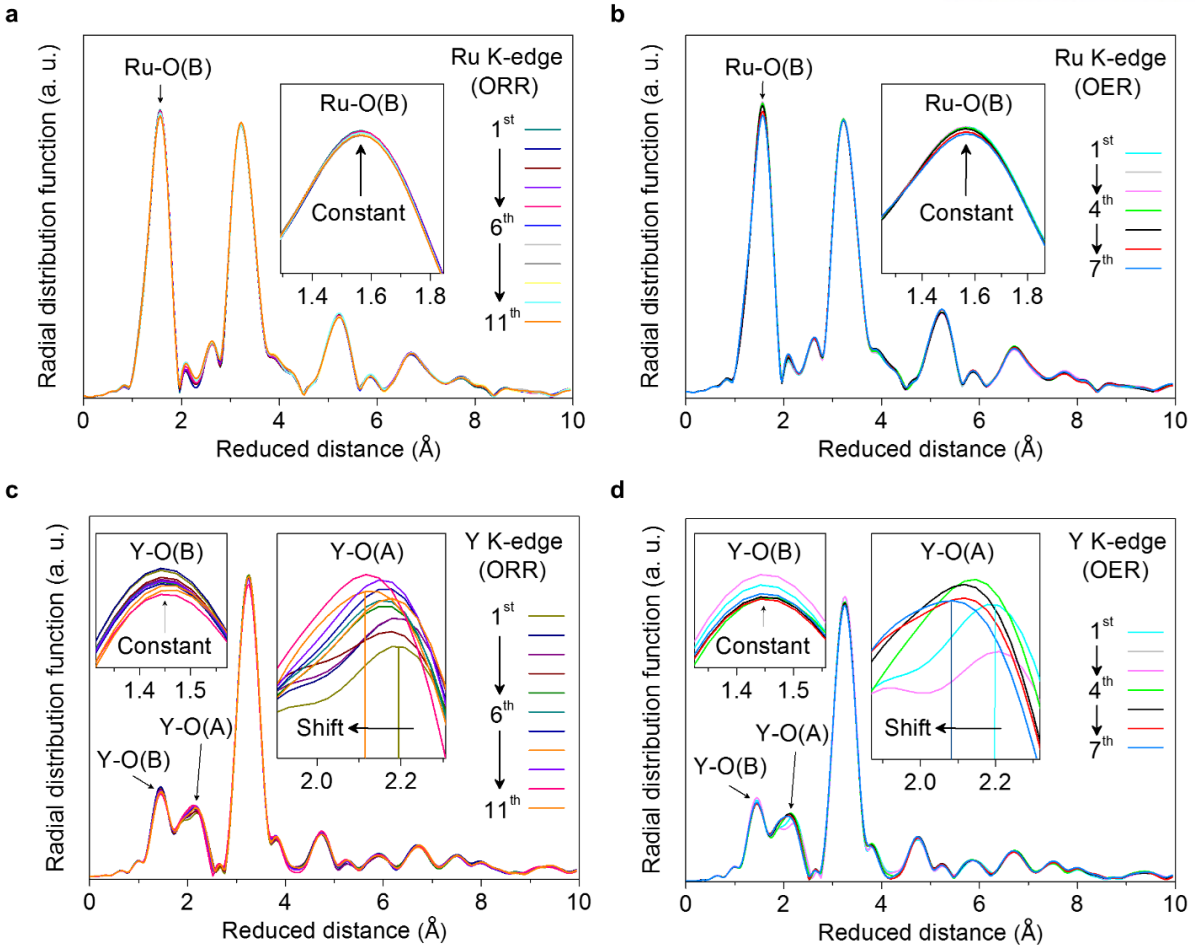

Figure 52. The extended X-ray absorption fine structure (EXAFS) spectra of the nanocrystalline YRO with pyrochlore structure by *in situ* XAS analysis. (a,b) Normalized radial distribution function (RDF) of Fourier-transformed k^3-weighted EXAFS spectra for ruthenium ions of the YRO during (a) ORR and (b) OER, and insets showing the magnified data. The ORR and OER potentials ranged from 0.93 to 0.23 and 1.43 V vs. RHE, respectively. The scan number of XAS analysis for ORR ranged from 1st to 11th, and OER ranged from 1st to 7th. (c,d) Normalized RDF of Fourier-transformed k^3-weighted EXAFS spectra for yttrium ions of the YRO during (c) ORR and (d) OER, and insets indicate the magnified data.

Furthermore, we explored the origin of the catalytic activity and structural stability of the YRO during electrochemical tests, and summarized the effect of the corresponding changes of the oxidation states. **Figure 53**a shows the schematic representations of the *in situ* XAS results for the YRO. In general, the ORR and OER occurs at the surface of the electrocatalyst particles.[167] On the other hand, the *in situ* XAS analysis investigates the electronic and geometric structures of bulk particles including surface and inner layers.[168] Accordingly, we suggest that the slight variations of the XANES and EXAFS spectra could be attributed to the substantial changes of yttrium and ruthenium ions at the YRO surface. In terms of reaction sequence, the cations were initially oxidized and donated electrons simultaneously with electrocatalysis. Further, the donated electrons could be continuously migrated into surface and inner layers providing the pathway of electrons during ORR and OER, respectively.

Figure 53b,c presents the oxidation state–scan number curves for A- and B-site cations of the YRO. The relative oxidation states corresponded to the photon energies at the highest peaks of XANES spectra. The scan number of XAS analysis for ORR ranged from 1st to 11th, and OER ranged from 1st to 7th (**Figure 50**a). Interestingly, the degrees of oxidation of yttrium and ruthenium ions were on average lower during CV in cathodic direction, compared to that of anodic direction. This result implies that the corresponding cathodic and anodic redox reactions in the YRO decreased and increased the degrees of oxidation of the cations simultaneously with CV test, respectively. Moreover, the oxidation states of these cations were slightly decreased after 3rd scan of XAS during OER, implying partially recovered catalytic active sites of the YRO. On this basis, the obtained curves indicated that the oxidation states of yttrium and ruthenium ions were on average increased during ORR and OER. These results suggest that both of these cations could easily transfer electrons by significant oxidations in the pyrochlore structure during electrocatalysis, resulting in the highly improved bi-functional catalytic activities of the YRO. This behavior was consistent with the experimental results of the electrochemical performance of the YRO, as shown in **Figure 40**.

Although the yttrium and ruthenium ions at B-sites were successfully oxidized as increasing the number of scan, the corresponding reduced distances between B-site cations and oxygen including Y-O and Ru-O bonds obtained by EXAFS spectra were constant (**Figure 53**d,e). It might be caused by the variable geometric local structure of Y-O bonds at A-sites instead of that of bonds between B-site cations and oxygen. These results imply that the pyrochlore structure could be maintained by the rigid RuO_6 structure upon battery cycling, resulting in highly enhanced charge and discharge performance of Zn–air batteries containing the YRO with a stable potential retention for 200 cycles, as shown in **Figure 40**f.

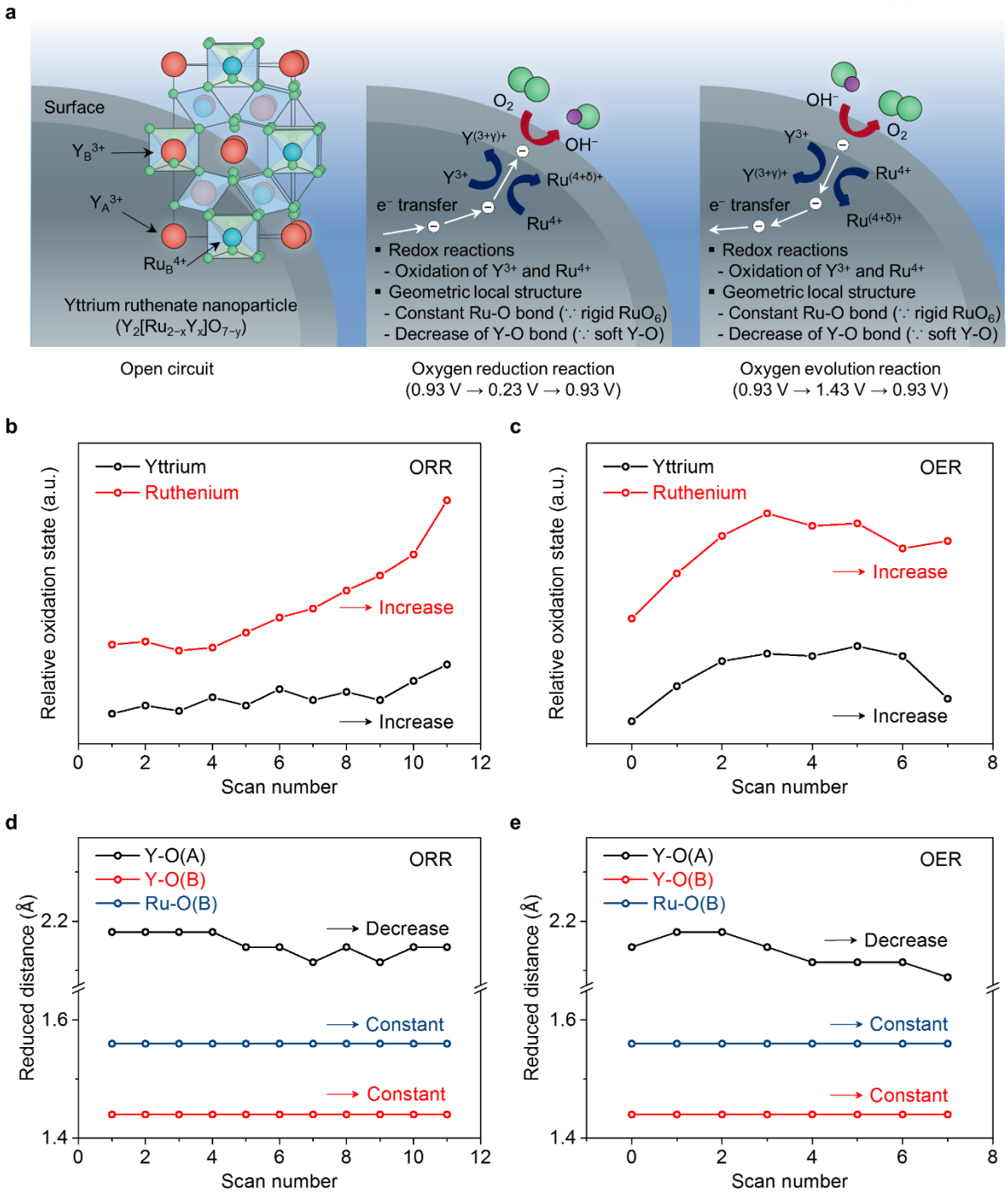

Figure 53. The catalytic origin of the nanocrystalline YRO with pyrochlore structure during electrocatalysis. (a) Schematic representations of the *in situ* XAS results for the YRO, showing the oxidations of yttrium and ruthenium ions and highly stable RuO_6 structure during ORR and OER. (b,c) The oxidation states of ruthenium and yttrium ions of the YRO during (b) ORR and (c) OER upon CV test simultaneously with XAS analysis. The relative oxidation states correspond to the photon energies

at the highest peaks of XANES spectra. The CV during the ORR and OER was recorded between 0.23 and 1.43 V vs. RHE. The corresponding ORR and OER potentials ranged from 0.93 to 0.23 and 1.43 V, respectively. The scan number of XAS analysis for ORR ranged from 1st to 11th, and OER ranged from 1st to 7th. (d,e) The reduced distances of Y-O bonds at A-sites, B-sites, and Ru-O bonds at B-sites of the YRO during (d) ORR and (e) OER upon CV test simultaneously with XAS analysis. The reduced distances were obtained by the experimental EXAFS spectra.

4.4 Summary

In conclusion, we first developed the yttrium ruthenate ($Y_2[Ru_{2-x}Y_x]O_{7-y}$) with pyrochlore structure as a bi-functional electrocatalyst for Zn–air batteries. The prepared YRO demonstrated low overpotential and high current density during ORR and OER, suggesting significantly enhanced catalytic activities. To reveal the catalytic origin of the pyrochlore oxide, we performed *in situ* XAS for real-time investigation of the electron configurations and geometric local structures during electrocatalysis. In particular, the oxidations of yttrium and ruthenium ions were successfully confirmed by XANES spectra, showing positive shift of the photon energy. Moreover, the high structural stability of the YRO was observed by the constant corresponding EXAFS spectra, which could ascribed to rigid RuO_6 structure. On this basis, we propose that both of these cations serve as electron pathway and can have a significant effect on the surface structural stability of the YRO. As a result, by using the YRO, we have successfully achieved the highly improved electrochemical performance of rechargeable Zn–air batteries with stable potential retention. We believe that this work will provide new insight into the highly reactive pyrochlore oxides for electrochemical applications.

Chapter 5

Polyhedral bismuth ruthenate pyrochlore as a bi-functional oxygen electrocatalyst for Zn−air flow batteries

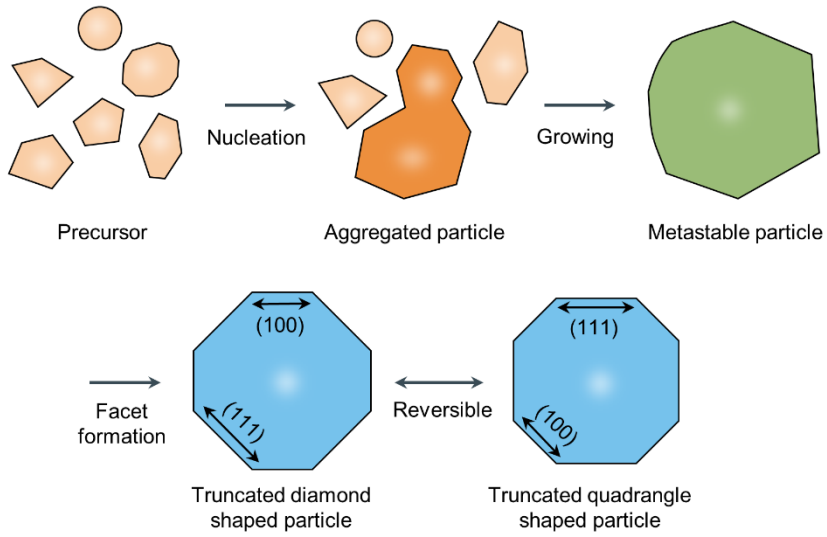

We report on the polyhedral-shaped pyrochlore oxides ($Bi_2Ru_2O_7$) as efficient bi-functional electrocatalysts, based upon the low-index facets including (100), (110) and (111). Notably, we first observed the facets development of the polyhedral-shaped pyrochlore oxides in real-time by *in situ* environmental transmission electron microscopy (TEM) spontaneously with heat treatment. Accordingly, a determination process of structural morphology for the low-index group consists of Ostwald ripening- and facets evolution-stages. Moreover, the prepared pyrochlore oxide demonstrates low overpotentials for ORR and OER, resulting in the significantly improved electrochemical performances for primary and rechargeable Zn–air flow batteries.

This chapter has not been published.

5.1 Introduction

The growing environmental deterioration and rapid depletion of fossil fuels, such as coal, oil and natural gas, have led to urgent needs of the electrochemical energy devices. With demand for alternatives to petroleum fuels, metal-air batteries have been considered promising electrical energy storage (EES) systems due to their environmental benignity and high specific energy densities. Among them, Zn–air batteries are the most promising candidate for practical application because of high energy density, high safety and low cost of zinc metal.[1, 5, 10, 152, 153] However, stack-type Zn–air batteries are limited to demonstrate highly stable potential retention, resulting from the saturation of zincate ion ($Zn(OH)_4^{2-}$) on discharging. In order to increase the zinc utilization, flow-type Zn–air batteries should be emerged as promising candidates. In this regard, Zn–air flow batteries are limited originated from the slow kinetics of oxygen reduction reaction (ORR) and oxygen evolution reaction (OER) as well as that of stack-type.[12, 42]

To date, pyrochlore oxides ($A_2[B_{2-x}A_x]O_{7-y}$) have been intensively studied as bi-functional oxygen electrocatalysts among a variety of metal oxides for achieving both high ORR and OER activities.[141, 156] For example, $Pb_2[Ru_{2-x}Pb_x^{4+}]O_{6.5}$, $Pb_2[Ir_{2-x}Pb_x]O_{7-y}$ and $Bi_2[Ru_{2-x}Bi_x]O_{7-y}$ exhibited substantially enhanced electrochemical performance because of the high charge transfer through the oxygen vacancies.[80, 138] However, the morphology control of the previous examples were still limited to inhomogeneous nanoparticles, thus resulting in poor understanding of morphology determination of the pyrochlore structure.

Herein, we report on the polyhedral-shaped pyrochlore oxides ($Bi_2Ru_2O_7$) as efficient bi-functional electrocatalysts, based upon the low-index facets including (100), (110) and (111). Notably, we first observed the facets development of the polyhedral-shaped pyrochlore oxides in real-time by *in situ* environmental transmission electron microscopy (TEM) spontaneously with heat treatment. Accordingly, a determination process of structural morphology for the low-index group consists of Ostwald ripening- and facets evolution-stages. Moreover, the prepared pyrochlore oxide demonstrates low overpotentials for ORR and OER, resulting in the significantly improved electrochemical performances for primary and rechargeable Zn–air flow batteries.

5.2 Experimental detail

Preparation of polyhedral bismuth ruthenate pyrochlore oxide: To prepare the polyhedral bismuth ruthenate pyrochlore oxide, a buffer solution was required. The buffer solution, NH_4–EDTA, was made with a mixture of 10 g anhydrous ethylenediaminetetraacetic acid (≥ 99% titration, Sigma-Aldrich), 1 M ammonia solution (28.0–30.0%, Samchun chemical), and 1.5 mL nitric acid (HNO_3, ACS regent 70%, Sigma-Aldrich) at a solution pH of 7. To prepare $Bi_2Ru_2O_7$, 8.22×10^{-4} mol bismuth (III) nitrate pentahydrate (reagent grade 98%, Sigma-Aldrich), 8.22×10^{-4} mol ruthenium (III) nitrosyl nitrate solution (1.5 wt% Ru, Sigma-Aldrich), and 10 g anhydrous citric acid (99%, Sigma-Aldrich) were dissolved and stirred with the buffer solution for 24 h at 150 °C. At this point, gelation was observed. The gelled solution was transferred to an oven at 200 °C for 6 h drying. The prepared powder was calcined in air at 1,050 °C for 5 h.

Preparation of the catalyst inks and working electrode: The catalyst inks were prepared with mixture of 16 mg of the polyhedral bismuth ruthenate pyrochlore oxide powder, 4 mg of ketjenblack carbon (EC 600JD), 200 μL of the 5wt% of Nafion in mixture of lower aliphatic alcohols and H_2O (Sigma-Aldrich), and 800 μL of ethanol. Briefly, the catalyst inks were prepared by ultrasonically mixing in distilled water for 1 h to make homogeneous mixture. The portion of 5 μL of inks were loaded on the glassy carbon of rotation ring disk electrode (RRDE) as the working electrode. The area of RRDE was 0.1256 cm^2. As a result, the loading level of the prepared pyrochlore oxide was 0.637 mg_{cat} cm^{-2}. For the loading level of 79.6 μg_{pt} cm^{-2} benchmarking catalyst, 10 mg of Pt/C on Vulcan XC 72 (20wt%, Premetek Co.) was dispersed in 200 μL of the 0.05% titrated Nafion solution and 800 μL of ethanol. After that, this catalyst ink was prepared by ultrasonically mixing in distilled water for at least 1 h to make homogeneous ink. Then, 5 μL of ink was loaded on the glassy carbon of working electrode that the loading level of 20% Pt/C and the pure Pt were 0.398 $mg_{(20\%\ Pt/C)}$ cm^{-2} and 79.6 μg_{Pt} cm^{-2}, respectively.

Electrochemical measurements: A three-electrode cell was used to measure the electrocatalytic activities of the polyhedral bismuth ruthenate pyrochlore oxide. The rotating ring disk electrode (RRDE) (ALS Co., Ltd) test was carried out based on the polyhedral-shaped pyrochlore catalysts film (loaded on the glassy carbon of RRDE) for the working electrode in O_2-saturated 0.1 M KOH alkaline electrolyte. Platinum wire and Hg/HgO were used as the counter and reference electrodes, respectively. Electrochemical characterizations were conducted using a bipotentiostat (IviumStat). The scan rate of 10 mV s^{-1} was swept from 1.13 V to 0.26 V (vs. RHE) for oxygen reduction reaction (ORR) and from 1.23 to 1.82 V (vs. RHE) for oxygen evolution reaction (OER). The ORR capacitance were corrected by averaging current of cyclic voltammetry plots (CVs) in O_2- and Ar-saturated electrolytes. The OER

CVs were capacitive-corrected by averaging current of the forward and backward sweeps. The capacitive-corrected ORR and OER currents were ohmically corrected with the measured ionic resistance (≈45 Ω). In addition, a ring potential of 0.4 V (vs. Hg/HgO) was applied to oxidize peroxide during ORR. The collection efficiency (N) was determined under Ar atmosphere using 10 mM $K_3[Fe(CN)_6]$, which is around 0.41. This value is similar to the theoretical value of 0.42. The peroxide yield (H_2O^-) and the number of transferred electrons (n) were calculated from the below equations.

$$H_2O^-(\%) = 100\frac{2I_r/N}{I_d+I_r/N} \quad (1)$$

$$\mathrm{n} = 4\frac{I_d}{I_d+I_r/N} \quad (2)$$

Primary Zn-air batteries tests: For primary Zn-air batteries tests based on the polyhedral bismuth ruthenate pyrochlore oxide, 0.75 g of zinc granular is used as an anode and 200 μL of 6 M KOH was used as an electrolyte. A nylon membrane was used as a separator. The air electrode which is a cathode was prepared by uniformly loaded gas diffusion layer (GDL) (the catalyst ink formulation: 16 mg of catalyst, 4 mg of ketjenblack, 200 μL of the 5wt% of the Nafion solution and 800 μL of ethanol on nickel mesh. Thickness of the electrode is around 500 μm. The assembled primary Zn-air batteries were tested at the discharge current densities of 20 mA cm^{-2}. The GDL was prepared from a mixture of activated charcoal (Darco G-60A, Sigma-Aldrich) and PTFE binder (60 wt% PTFE emulsion in water, Sigma-Aldrich) at a weight ratio of 7:3 with about 450 μm of thickness to ensure proper gas distribution and sufficient current collection. This prepared GDL was used as the reference for comparison to confirm enhanced performance of air electrode based on catalysts in polarization curves of the Zn-air batteries.

Rechargeable Zn-air flow batteries tests: For primary Zn-air batteries tests based on the polyhedral bismuth ruthenate pyrochlore oxide, 0.5 g of zinc plate is used as an anode and 2 mL of 6 M KOH with 0.2 M ZnO as an electrolyte. Preparation method of air electrode with the catalysts is same as primary Zn-air batteries except nickel mesh. Thickness of the electrode is around 950 μm. In this case, nickel foam is used for air electrode instead of mesh. The assembled rechargeable Zn-air batteries were tested at the discharge/charge current densities of 10 mA cm^{-2}.

Materials characterizations: The material morphologies were examined using SEM (VERIOS 460, FEI), high-resolution transmission electron microscopy (HR-TEM) (JEM-2100F, JEOL) operating at 200 kV. Powder analysis was performed using an X-ray diffractometer (XRD) (D/Max2000, Rigaku).

5.3 Results and discussion

Figure 50a presents the synthetic procedure of the polyhedral bismuth ruthenate pyrochlore oxide ($Bi_2Ru_2O_7$). Briefly, the pyrochlore oxide, hereafter referred to as a BRO, was synthesized by the sol-gel method using a citric acid as chelating agent for crosslinking the A- and B-site cations of trivalent bismuth and tetravalent ruthenium ions, respectively. The BRO was crystallized at an elevated temperature of 1,050 °C. The cubic phase of the pyrochlore oxide structure was successfully confirmed by X-ray diffraction (XRD) as shown in **Figure 50**b. The space groups of the pyrochlore oxides are Fd-3m symmetry without any defects at oxygen site, based upon the balanced stoichiometry. In order to investigate the facets difference of the pyrochlore oxides, we carried out the scanning electron microscopy (SEM) in **Figure 50**c. The BRO microparticles consist of (100), (110) and (111) facets with particle sizes of ≤ 1 μm.

To further clarify the structural integrity of the pyrochlore structure, the BRO microparticles were subjected to focused-ion beam (FIB) milling. The cross-sections of the particles were investigated by high-angle annular dark field scanning TEM (STEM-HAADF) and energy-dispersive X-ray spectroscopy (EDS), respectively **(Figure 50**d,e). These results imply that the BRO was successfully synthesized based upon homogenous distribution and stoichiometric ratio of trivalent bismuth and tetravalent ruthenium ions. Moreover, we demonstrated fast Fourier transform (FFT) image of the BRO originated from high resolution TEM (HR-TEM), as shown in **Figure 50**f,g. The FFT analysis of the pyrochlore oxides was performed in the main zone axis of [100] direction, implying cubic phases of pyrochlore structure based on the unit spots of (–11–1) and (–111) with an axial angle of 70.53°. Moreover, the corresponding STEM-HAADF images clearly show that the lattice fringes with d-spacing values of 0.30 nm and 0.51 nm correspond to (111) and (002) crystal planes, respectively (**Figure 50**h). These results suggest that the BRO exhibited highly pure and crystalline microparticles with pyrochlore oxide structure.

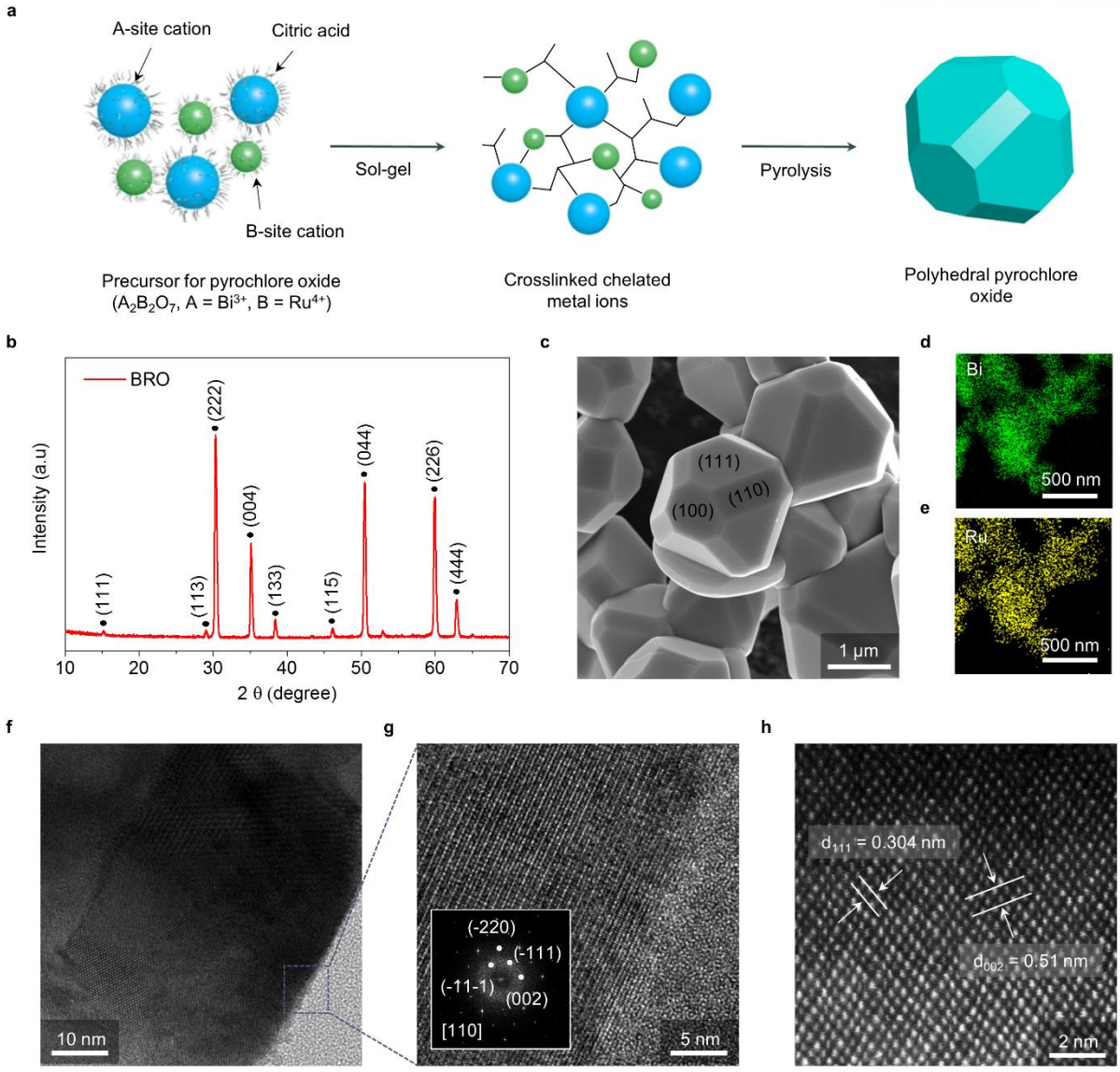

Figure 54. Preparation, morphology and structural characterization of polyhedral pyrochlore oxides ($A_2B_2O_7$). (a) Schematic of the synthesis process of polyhedral bismuth ruthenate pyrochlore ($Bi_2Ru_2O_7$), hereafter referred to as a BRO, with pyrochlore structure by sol-gel method. They consist of trivalent bismuth (blue sphere), tetravalent ruthenium (green sphere), and divalent oxygen ions that bonds them together. (b) Powder XRD patterns of BRO nanoparticles. (c) SEM image of BRO. (d,e) STEM-HAADF-EDS images of the BRO with elemental maps of (d) bismuth and (e) ruthenium. (f,g) The HR-TEM images of the BRO at (f) low and (g) high magnifications. The inset of (g) indicates the FFT pattern of HR-TEM for BRO along the [110] main zone axis. The indexed spots refer to the lattice planes of (–111), (–11–1), (002) and (–220) in the pyrochlore structure. (h) The corresponding STEM-HAADF images of BRO with d-spacing values of 0.30 nm and 0.51 nm correspond to (111) and (002) crystal planes, respectively.

In order to investigate the facets evolution of the polyhedral-shaped pyrochlore oxides during pyrolysis in real-time, we carried out *in situ* TEM analysis. The *in situ* TEM set-up is based on previous studies. Notably, a specimen chamber is separately equipped to provide catalytically essential temperatures and gas environments. The specialized heating holder for the environmental TEM consists of spiral-shaped tungsten wire and gas injection nozzle for controlling the temperature and atmosphere, respectively. The precursor particles of the pyrochlore oxides were loaded on the heating element near the entrance of the gas injection nozzle. The particles were pyrolyzed from room temperature to 1,050 °C simultaneously with blowing air. We followed the structural changes of the pyrochlore oxides as increasing the temperature in real-time.

Figure 55 show time-lapse sequence of the schematic representations and STEM images for the pyrochlore oxides during crystallization at an elevated temperature of 1,050 °C. At the initial stage; ranged from 0 to 120 secs, we observed the nucleation of the precursor to a partially aggregated particle. Then, the larger nucleus was grown to the metastable nanoparticle (≤ 20 nm) by absorbing the dissolved smaller particles (≤ 3 nm) at 160 secs to reduce the overall interfacial energy in the system, indicating thermodynamically-driven spontaneous process of Ostwald ripening (**Figure 55**a). The metastable nanoparticle was transformed into the low-index facets dominant polyhedral-shaped structure by development of various facets as (100), (110) and (111) at the second stage; ranged from 200 to 330 secs (**Figure 55**b). Notably, the polyhedral-shaped structure was reversibly transformed from a truncated diamond-shaped into quadrangle-shaped structures in a two dimensional repetitively, showing a rapid replacement of (100) with (111). In this regard, we summarized the *in situ* TEM results, showing structural determination processes including Ostwald ripening- and facets evolution-stages, as shown in **Figure 55**c. Furthermore, after a determination process of structural morphology for the BRO, the stabilized facets were obviously obtained. The corresponding FFT image of a pyrochlore oxide was in good agreement with the cubic phases along the [110] main zone axis based upon the unit spots of (–11–1) and (–111) with 70.53° axial angle.

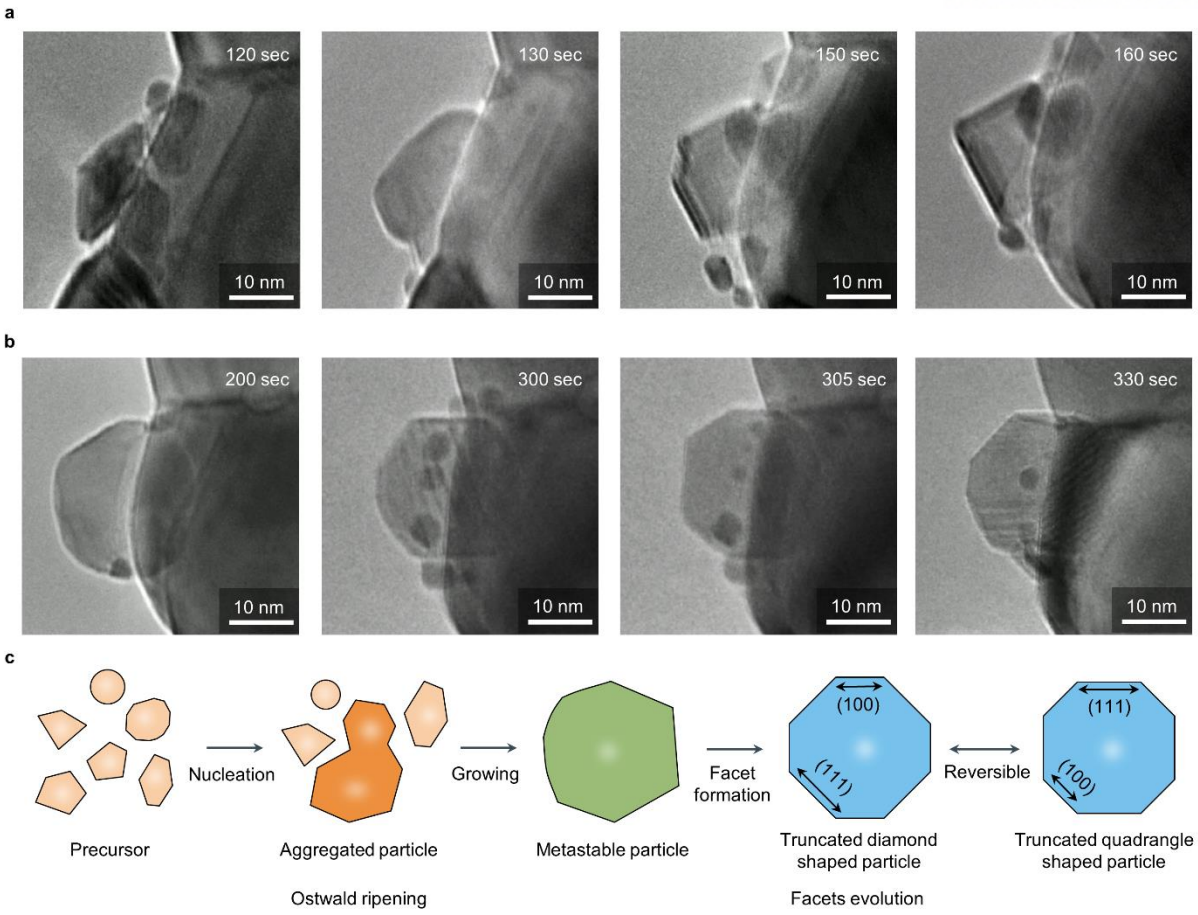

Figure 55. *In situ* TEM analysis. (a,b) Time-lapse sequence of STEM images for the polyhedral bismuth ruthenate pyrochlore oxide during crystallization at an elevated temperature of 1,050 °C, showing structural determination processes including (a) Ostwald ripening- and (b) facets evolution-stages. (c) Time-lapse sequence of the schematic representation of the structural determination processes.

To ascertain whether the various facets observed in the polyhedral bismuth ruthenate pyrochlore oxide during synthesis directly affects the electrocatalytic behaviors, we performed the rotation ring disk electrode (RRDE) method. **Figure 56**a shows the ohmic- and capacitive-corrected linear scan voltammogram (LSV) curves for ORR activities of the BRO and Pt/C. The onset potential of the state-of-the-art Pt/C as a reference sample showed the lower value of 1.05 V vs. RHE than that of the BRO (≈0.88 V). However, the limiting current density of the BRO (–5.17 mA cm^{-2}) showed a very similar value of Pt/C (–5.06 mA cm^{-2}) near 0.23 V. Additionally, the BRO showed the lowest onset potential and the highest current density (≈8.17 mA cm^{-1} @ 1.7 V) during OER (**Figure 56**b). These results could be ascribed to substantial improvement of bi-functional catalytic activities of the BRO.

In order to examine the bi-functional catalytic activities of the BRO in energy storage system, we carried out primary and rechargeable Zn–air flow batteries. Zn–air flow batteries consists of zinc metal anode, catalyst containing air electrode, 6 M KOH electrolyte and pump for flowing the electrolyte. The detailed fabrication is in the Methods. The significance of the system is that the circulation of electrolyte effectively removes ZnO particles on the surface of air electrode, resulting from the saturation of $Zn(OH)_4^{2-}$ on discharging. Also evident in **Figure 56**c is a strong dependence of the circulation by a direct comparison of the electrochemical performances for the stack- and flow-type Zn–air batteries using a pristine air electrode. On discharging, the operating voltage and duration of the flow-type represented improvements of approximately ≈2% and ≈50% compared to that of the stack-type at a current density of 25 mA cm^{-2}, respectively. These results could be ascribed to a highly increased zinc utilization of the Zn–air flow batteries.

To demonstrate the practical applications of the flow-type Zn–air batteries, the primary batteries containing the BRO and Pt/C were subjected to the discharge tests at a current density of 25 mA cm^{-2} (**Figure 56**d). The discharge duration of Pt/C was almost two times higher than that of the pristine air electrode. Notably, the discharge capacity of the BRO showed a significantly increased value comparable to that of Pt/C. In addition, these samples showed the highly improved specific energy densities (≤ 970 Wh kg^{-1}) comparable to the theoretical value of the Zn–air batteries (1,084 Wh kg^{-1}), which were consistent with the order of discharge capacity from the primary Zn–air batteries tests (**Figure 56**e). These results suggest that the BRO could demonstrate low overpotential which was in good agreement with the calculated values for ORR, thus resulting in the substantially improved electrochemical performance on discharging.

To explore the bi-functional catalytic activities of the BRO, the rechargeable Zn–air batteries were subjected to short cycle period tests (600 secs per cycle) at a current density of 10 mA cm^{-2} (**Figure 56**f), corresponding to a depth of discharge (DOD) of ~1%. Although the initial differences of operating voltage between charge and discharge processes ($\Delta\eta_{initial}$) were similar with the BRO (≈0.73 V) and the

mixture of Pt/C and IrO_2 (≈0.74 V), a large difference was observed after 100 cycles ($\Delta\eta_{100}$). The BRO showed highly stable potential retention for 100 cycles ($|\Delta\eta_{100} - \Delta\eta_{initial}|$ = 0.02 V). However, as the number of cycles increased, the operating voltage of the Pt/C gradually increased from 1.94 V to 1.98 V on charging. This implied that the rechargeability of the BRO was considerably enhanced than that of Pt/C, which may have been caused by the stable structure and low overpotential of the pyrochlore oxide during OER.

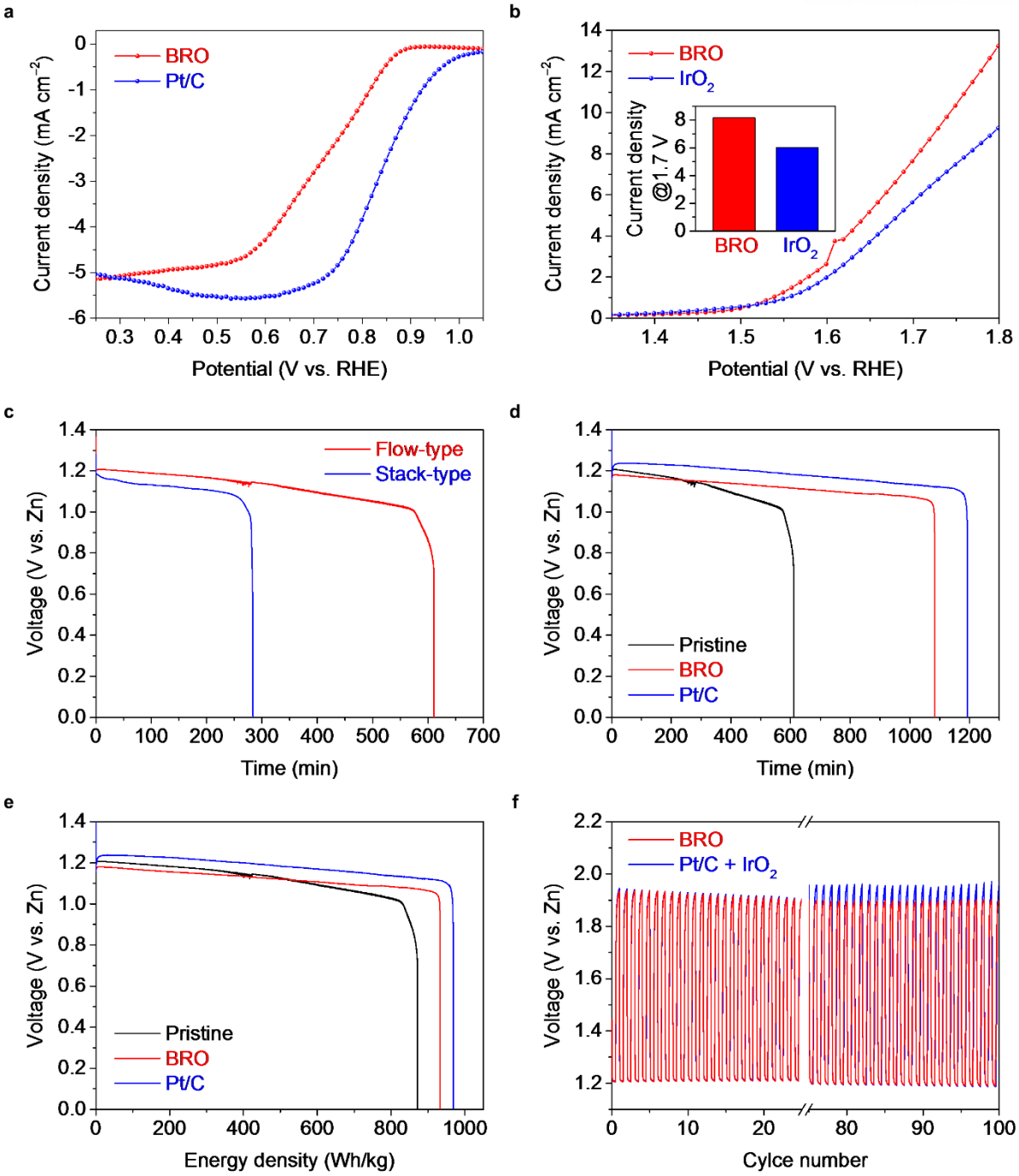

Figure 56. Electrocatalytic activities of the polyhedral BRO with pyrochlore structure. (a) Linear scan voltammogram (LSV) curves of the BRO and Pt/C during ORR. The electrochemical characterization were performed using a rotation ring-disk electrode (RRDE) in O_2-saturated 0.1 M KOH at a rotation speed of 1600 rpm and scan rate of 10 mV s^{-1}. The ORR potential ranged from 1.13 to 0.26 V vs. RHE. (b) LSV curves of the BRO and IrO_2 during OER, and inset indicates the current density of the BRO and IrO_2 at a potential of 1.7 V. The OER potential ranged from 1.23 to 1.82 V. (c) Discharge curves of

stack- and flow-type Zn–air batteries at a current density of 20 mA cm^{-2}. (d,e) Discharge curves of the flow-type Zn–air batteries using the BRO and Pt/C at a current density of 20 mA cm^{-2}. (f) The battery cycling curves of the rechargeable Zn–air flow batteries using the BRO and the mixture of Pt/C and IrO_2 during charging and discharging processes at a current density of 10 mA cm^{-2} in short cycle periods (10 min per cycle) with ambient air.

5.4 Summary

In conclusion, we first developed the bismuth ruthenate pyrochlore with polyhedral structure ($Bi_2Ru_2O_7$) as a bi-functional electrocatalyst for Zn–air flow batteries. The prepared bismuth ruthenate pyrochlore oxide consists of the low-index facets including (100), (110) and (111). In order to investigate the facets development of the polyhedral-shaped pyrochlore oxide in real-time, we carried out *in situ* environmental transmission electron microscopy (TEM) spontaneously with heat treatment. Notably, we observed the determination processes of structural morphology for the low-index facets of polyhedral structure including Ostwald ripening- and facets evolution-stages. Moreover, the prepared pyrochlore oxide demonstrates low overpotentials for ORR and OER, resulting in the significantly improved electrochemical performances for primary and rechargeable Zn–air flow batteries.

References

1. Armand M., Tarascon J. M. Building better batteries. *Nature,* **451**, 652-657 (2008).

2. Kang K., Meng Y. S., Bréger J., Grey C. P., Ceder G. Electrodes with High Power and High Capacity for Rechargeable Lithium Batteries. *Science,* **311**, 977-980 (2006).

3. Xiao J., Kuang Q., Yang S., Xiao F., Wang S., Guo L. Surface Structure Dependent Electrocatalytic Activity of Co_3O_4 Anchored on Graphene Sheets toward Oxygen Reduction Reaction. *Sci. Rep.,* **3**, 2300 (2013).

4. Lee J.-S., Kim S. T., Cao R., Choi N.-S., Liu M., Lee K. T.*, et al.* Metal–Air Batteries with High Energy Density: Li–Air versus Zn–Air. *Adv. Energy Mater.,* **1**, 34-50 (2011).

5. McLarnon F. R., Cairns E. J. The Secondary Alkaline Zinc Electrode. *J. Electrochem. Soc.,* **138**, 645-656 (1991).

6. Arora P., Zhang Z. Battery Separators. *Chem. Rev.,* **104**, 4419-4462 (2004).

7. Zhang. Zinc-air technology. *Int. Zn. Assoc.,* (2005).

8. Kim H., Jeong G., Kim Y.-U., Kim J.-H., Park C.-M., Sohn H.-J. Metallic anodes for next generation secondary batteries. *Chem. Soc. Rev.,* **42**, 9011-9034 (2013).

9. Sapkota P., Kim H. Zinc–air fuel cell, a potential candidate for alternative energy. *J. Ind. Eng. Chem.,* **15**, 445-450 (2009).

10. Li Y., Dai H. Recent advances in zinc-air batteries. *Chem. Soc. Rev.,* **43**, 5257-5275 (2014).

11. Gewirth A. A., Thorum M. S. Electroreduction of Dioxygen for Fuel-Cell Applications: Materials and Challenges. *Inorg. Chem.,* **49**, 3557-3566 (2010).

12. Debe M. K. Electrocatalyst approaches and challenges for automotive fuel cells. *Nature,* **486**, 43-51 (2012).

13. Linden D., Reddy T. B. Handbooks of Batteries. *McGraw-Hill,* (2001).

14. Oyama A., Odahara T., Fuchino S., Shinoda M., Shimomura H. *US Pat.*, 6746509 (2004).

15. Ma H., Li C., Su Y., Chen J. Studies on the vapour-transport synthesis and electrochemical properties

of zinc micro-, meso- and nanoscale structures. *J. Mater. Chem.,* **17**, 684-691 (2007).

16. Yang C.-C., Lin S.-J. Improvement of high-rate capability of alkaline Zn–MnO_2 battery. *J. Power Sources,* **112**, 174-183 (2002).

17. Zhang X. G. Fibrous zinc anodes for high power batteries. *J. Power Sources,* **163**, 591-597 (2006).

18. Drillet J.-F., Adam M., Barg S., Herter A., Koch D., Schmidt V.*, et al.* Development of a Novel Zinc/Air Fuel Cell with a Zn Foam Anode, a PVA/KOH Membrane and a MnO_2/SiOC-Based Air Cathode. *ECS Trans.,* **28**, 13-24 (2010).

19. Lee C. W., Sathiyanarayanan K., Eom S. W., Yun M. S. Novel alloys to improve the electrochemical behavior of zinc anodes for zinc/air battery. *J. Power Sources,* **160**, 1436-1441 (2006).

20. Suresh Kannan A. R., Muralidharan S., Sarangapani K. B., Balaramachandran V., Kapali V. Corrosion and anodic behaviour of zinc and its ternary alloys in alkaline battery electrolytes. *J. Power Sources,* **57**, 93-98 (1995).

21. Ein-Eli Y., Auinat M., Starosvetsky D. Electrochemical and surface studies of zinc in alkaline solutions containing organic corrosion inhibitors. *J. Power Sources,* **114**, 330-337 (2003).

22. Vatsalarani J., Geetha S., Trivedi D. C., Warrier P. C. Stabilization of zinc electrodes with a conducting polymer. *J. Power Sources,* **158**, 1484-1489 (2006).

23. Cho Y.-D., Fey G. T.-K. Surface treatment of zinc anodes to improve discharge capacity and suppress hydrogen gas evolution. *J. Power Sources,* **184**, 610-616 (2008).

24. Lee S.-M., Kim Y.-J., Eom S.-W., Choi N.-S., Kim K.-W., Cho S.-B. Improvement in self-discharge of Zn anode by applying surface modification for Zn–air batteries with high energy density. *J. Power Sources,* **227**, 177-184 (2013).

25. Maiche L. *French Pat.*, 127069 (1878).

26. Heise G. W. *US Pat.*, 1899615 (1933).

27. Bidault F., Brett D. J. L., Middleton P. H., Brandon N. P. Review of gas diffusion cathodes for alkaline fuel cells. *J. Power Sources,* **187**, 39-48 (2009).

28. Kordesch K., Jahangir S., Schautz M. Engineering concepts and technical performance of oxygen-

reducing electrodes for batteries and electrochemical processes. *Electrochim. Acta,* **29**, 1589-1596 (1984).

29. Maja M., Orecchia C., Strano M., Tosco P., Vanni M. Effect of structure of the electrical performance of gas diffusion electrodes for metal air batteries. *Electrochim. Acta,* **46**, 423-432 (2000).

30. See D. M., White R. E. Temperature and Concentration Dependence of the Specific Conductivity of Concentrated Solutions of Potassium Hydroxide. *J. Chem. Eng. Data,* **42**, 1266-1268 (1997).

31. Othman R., Basirun W. J., Yahaya A. H., Arof A. K. Hydroponics gel as a new electrolyte gelling agent for alkaline zinc–air cells. *J. Power Sources,* **103**, 34-41 (2001).

32. Yang C.-C., Lin S.-J. Alkaline composite PEO–PVA–glass-fibre-mat polymer electrolyte for Zn–air battery. *J. Power Sources,* **112**, 497-503 (2002).

33. Simons T. J., Torriero A. A. J., Howlett P. C., MacFarlane D. R., Forsyth M. High current density, efficient cycling of Zn^{2+} in 1-ethyl-3-methylimidazolium dicyanamide ionic liquid: The effect of Zn^{2+} salt and water concentration. *Electrochem. Commun.,* **18**, 119-122 (2012).

34. Harting K., Kunz U., Turek T. Zinc-air Batteries: Prospects and Challenges for Future Improvement. *Z. Physiol. Chem.,* **226**, 151 (2012).

35. Kritzer P., Cook J. A. Nonwovens as Separators for Alkaline Batteries: An Overview. *J. Electrochem. Soc.,* **154**, A481-A494 (2007).

36. Wu G. M., Lin S. J., Yang C. C. Preparation and characterization of high ionic conducting alkaline non-woven membranes by sulfonation. *J. Membr. Sci.,* **284**, 120-127 (2006).

37. Wu G. M., Lin S. J., You J. H., Yang C. C. Study of high-anionic conducting sulfonated microporous membranes for zinc-air electrochemical cells. *Mater. Chem. Phys.,* **112**, 798-804 (2008).

38. Saputra H., Othman R., Sutjipto A. G. E., Muhida R. MCM-41 as a new separator material for electrochemical cell: Application in zinc–air system. *J. Membr. Sci.,* **367**, 152-157 (2011).

39. Dewi E. L., Oyaizu K., Nishide H., Tsuchida E. Cationic polysulfonium membrane as separator in zinc–air cell. *J. Power Sources,* **115**, 149-152 (2003).

40. Wang Y.-J., Qiao J., Baker R., Zhang J. Alkaline polymer electrolyte membranes for fuel cell

applications. *Chem. Soc. Rev.,* **42**, 5768-5787 (2013).

41. Cheng F., Chen J. Metal-air batteries: from oxygen reduction electrochemistry to cathode catalysts. *Chem. Soc. Rev.,* **41**, 2172-2192 (2012).

42. Wang Z.-L., Xu D., Xu J.-J., Zhang X.-B. Oxygen electrocatalysts in metal-air batteries: from aqueous to nonaqueous electrolytes. *Chem. Soc. Rev.,* **43**, 7746-7786 (2014).

43. Yeager E. Electrocatalysts for O_2 reduction. *Electrochim. Acta,* **29**, 1527-1537 (1984).

44. Sidik R. A., Anderson A. B., Subramanian N. P., Kumaraguru S. P., Popov B. N. O_2 Reduction on Graphite and Nitrogen-Doped Graphite: Experiment and Theory. *J. Phys. Chem. B,* **110**, 1787-1793 (2006).

45. Maldonado S., Stevenson K. J. Influence of nitrogen doping on oxygen reduction electrocatalysis at carbon nanofiber electrodes. *J. Phys. Chem. B,* **109**, 4707-4716 (2005).

46. Zheng Y., Jiao Y., Jaroniec M., Jin Y., Qiao S. Z. Nanostructured Metal-Free Electrochemical Catalysts for Highly Efficient Oxygen Reduction. *Small,* **8**, 3550-3566 (2012).

47. Gong K., Du F., Xia Z., Durstock M., Dai L. Nitrogen-Doped Carbon Nanotube Arrays with High Electrocatalytic Activity for Oxygen Reduction. *Science,* **323**, 760-764 (2009).

48. Liu R., Wu D., Feng X., Müllen K. Nitrogen-Doped Ordered Mesoporous Graphitic Arrays with High Electrocatalytic Activity for Oxygen Reduction. *Angew. Chem. Int. Ed.,* **49**, 2565-2569 (2010).

49. Yang W., Fellinger T.-P., Antonietti M. Efficient Metal-Free Oxygen Reduction in Alkaline Medium on High-Surface-Area Mesoporous Nitrogen-Doped Carbons Made from Ionic Liquids and Nucleobases. *J. Am. Chem. Soc.,* **133**, 206-209 (2011).

50. Morcos I., Yeager E. Kinetic studies of the oxygen—peroxide couple on pyrolytic graphite. *Electrochim. Acta,* **15**, 953-975 (1970).

51. Qu D. Investigation of oxygen reduction on activated carbon electrodes in alkaline solution. *Carbon,* **45**, 1296-1301 (2007).

52. Lefevre M., Proietti E., Jaouen F., Dodelet J. P. Iron-based catalysts with improved oxygen reduction activity in polymer electrolyte fuel cells. *Science,* **324**, 71-4 (2009).

53. Wu Z.-S., Chen L., Liu J., Parvez K., Liang H., Shu J.*, et al.* High-Performance Electrocatalysts for Oxygen Reduction Derived from Cobalt Porphyrin-Based Conjugated Mesoporous Polymers. *Adv. Mater.*, 1450-1455 (2014).

54. Li Y., Zhou W., Wang H., Xie L., Liang Y., Wei F.*, et al.* An oxygen reduction electrocatalyst based on carbon nanotube-graphene complexes. *Nat. Nanotechnol.,* **7**, 394-400 (2012).

55. Scherson D. A., Yao S. B., Yeager E. B., Eldridge J., Kordesch M. E., Hoffman R. W. In situ and ex situ Moessbauer spectroscopy studies of iron phthalocyanine adsorbed on high surface area carbon. *J. Phys. Chem.,* **87**, 932-943 (1983).

56. Lefèvre M., Dodelet J. P., Bertrand P. Molecular Oxygen Reduction in PEM Fuel Cells: Evidence for the Simultaneous Presence of Two Active Sites in Fe-Based Catalysts. *J. Phys. Chem. B,* **106**, 8705-8713 (2002).

57. Ferrandon M., Kropf A. J., Myers D. J., Artyushkova K., Kramm U., Bogdanoff P.*, et al.* Multitechnique Characterization of a Polyaniline–Iron–Carbon Oxygen Reduction Catalyst. *J. Phys. Chem. C,* **116**, 16001-16013 (2012).

58. Li Zhu A., Wang H., Qu W., Li X., Jong Z., Li H. Low temperature pyrolyzed cobalt tetramethoxy phenylporphyrin catalyst and its applications as an improved catalyst for metal air batteries. *J. Power Sources,* **195**, 5587-5595 (2010).

59. Cheng F., Zhang T., Zhang Y., Du J., Han X., Chen J. Enhancing Electrocatalytic Oxygen Reduction on MnO_2 with Vacancies. *Angew. Chem. Int. Ed.,* **52**, 2474-2477 (2013).

60. Liang Y., Li Y., Wang H., Zhou J., Wang J., Regier T.*, et al.* Co_3O_4 nanocrystals on graphene as a synergistic catalyst for oxygen reduction reaction. *Nat. Mater.,* **10**, 780-786 (2011).

61. Cheng F., Shen J., Peng B., Pan Y., Tao Z., Chen J. Rapid room-temperature synthesis of nanocrystalline spinels as oxygen reduction and evolution electrocatalysts. *Nat. Chem.,* **3**, 79-84 (2011).

62. Lee J. S., Lee T., Song H. K., Cho J., Kim B. S. Ionic liquid modified graphene nanosheets anchoring manganese oxide nanoparticles as efficient electrocatalysts for Zn-air batteries. *Energy Environ. Sci.,* **4**, 4148-4154 (2011).

63. Jung J.-I., Jeong H. Y., Lee J.-S., Kim M. G., Cho J. A Bifunctional Perovskite Catalyst for Oxygen Reduction and Evolution. *Angew. Chem. Int. Ed.,* **53**, 4582-4586 (2014).

64. Suntivich J., May K. J., Gasteiger H. A., Goodenough J. B., Shao-Horn Y. A Perovskite Oxide Optimized for Oxygen Evolution Catalysis from Molecular Orbital Principles. *Science,* **334**, 1383-1385 (2011).

65. Jung J.-I., Risch M., Park S., Kim M. G., Nam G., Jeong H.-Y*., et al.* Optimizing nanoparticle perovskite for bifunctional oxygen electrocatalysis. *Energy Environ. Sci.,* **9**, 176-183 (2016).

66. Suntivich J., Gasteiger H. A., Yabuuchi N., Nakanishi H., Goodenough J. B., Shao-Horn Y. Design principles for oxygen-reduction activity on perovskite oxide catalysts for fuel cells and metal–air batteries. *Nat. Chem.,* **3**, 546-550 (2011).

67. Tanaka H., Misono M. Advances in designing perovskite catalysts. *Current Opinion in Solid State and Materials Science,* **5**, 381-387 (2001).

68. Brik M. G., Srivastava A. M., Tanaka I. Pyrochlore Structural Chemistry: Predicting the Lattice Constant by the Ionic Radii and Electronegativities of the Constituting Ions. *J. Am. Ceram. Soc.,* **95**, 1454-1460 (2012).

69. Aleshin E., Roy R. Crystal Chemistry of Pyrochlore. *J. Am. Ceram. Soc.,* **45**, 18-25 (1962).

70. Prakash J., Tryk D., Aldred W., Yeager E. in Electrochemistry in Transition: From the 20th to the 21st Century (eds. Murphy, O.J., Srinivasan, S. & Conway, B.E.) 93-106 (Springer US, Boston, MA, 1992).

71. Michael W. G., Phillip T. B., Christina S. B., Lauren M. M., Efrain E. R., Galen D. S*., et al.* Structural disorder, magnetism, and electrical and thermoelectric properties of pyrochlore $Nd_2Ru_2O_7$. *J. Phys.: Condens. Matter,* **25**, 186004 (2013).

72. Prakash J., Tryk D. A., Aldred W., Yeager E. B. Investigations of ruthenium pyrochlores as bifunctional oxygen electrodes. *J. Appl. Electrochem.,* **29**, 1463-1469 (1999).

73. Fujii K., Sato Y., Takase S., Shimizu Y. Effects of Oxygen Vacancies and Reaction Conditions on Oxygen Reduction Reaction on Pyrochlore-Type Lead-Ruthenium Oxide. *J. Electrochem. Soc.,* **162**,

129-135 (2015).

74. Modeshia D. R., Walton R. I. Solvothermal synthesis of perovskites and pyrochlores: crystallisation of functional oxides under mild conditions. *Chem. Soc. Rev.,* **39**, 4303-4325 (2010).

75. Akazawa T., Inaguma Y., Katsumata T., Hiraki K., Takahashi T. Flux growth and physical properties of pyrochlore $Pb_2Ru_2O_{6.5}$ single crystals. *J. Cryst. Growth,* **271**, 445-449 (2004).

76. Sardar K., Ball S. C., Sharman J. D. B., Thompsett D., Fisher J. M., Smith R. A. P.*, et al.* Bismuth Iridium Oxide Oxygen Evolution Catalyst from Hydrothermal Synthesis. *Chem. Mater.,* **24**, 4192-4200 (2012).

77. Abate C., Esposito V., Duncan K., Nino J. C., Gattia D. M., Wachsman E. D.*, et al.* Novel $Y_{2-x}Pr_xRu_2O_7$ (x=0–2) Pyrochlore Oxides Prepared Using a Soft Chemistry Route and their Electrical Properties. *J. Am. Ceram. Soc.,* **93**, 1970-1977 (2010).

78. Oh S. H., Nazar L. F. Oxide Catalysts for Rechargeable High-Capacity Li–O_2 Batteries. *Adv. Energy Mater.,* **2**, 903-910 (2012).

79. Marković N. M., Ross P. N. A Study of Bismuth Ruthenate as an Electrocatalyst for Bifunctional Air Electrodes. *J. Electrochem. Soc.,* **141**, 2590-2597 (1994).

80. Goodenough J. B., Manoharan R., Paranthaman M. Surface protonation and electrochemical activity of oxides in aqueous solution. *J. Am. Chem. Soc.,* **112**, 2076-2082 (1990).

81. ten Kortenaar M. V., Vente J. F., Ijdo D. J. W., Müller S., Kötz R. Oxygen evolution and reduction on iridium oxide compounds. *J. Power Sources,* **56**, 51-60 (1995).

82. Shukla A. K., Kannan A. M., Hegde M. S., Gopalakrishnan J. Effect of counter cations on electrocatalytic activity of oxide pyrochlores towards oxygen reduction/evolution in alkaline medium: an electrochemical and spectroscopic study. *J. Power Sources,* **35**, 163-173 (1991).

83. Oh S. H., Black R., Pomerantseva E., Lee J. H., Nazar L. F. Synthesis of a metallic mesoporous pyrochlore as a catalyst for lithium-O_2 batteries. *Nat. Chem.,* **4**, 1004-10 (2012).

84. Nishide H., Oyaizu K. Toward Flexible Batteries. *Science,* **319**, 737-738 (2008).

85. Meng C., Liu C., Chen L., Hu C., Fan S. Highly Flexible and All-Solid-State Paperlike Polymer

Supercapacitors. *Nano Lett.,* **10**, 4025-4031 (2010).

86. Lee S.-Y., Choi K.-H., Choi W.-S., Kwon Y. H., Jung H.-R., Shin H.-C.*, et al.* Progress in flexible energy storage and conversion systems, with a focus on cable-type lithium-ion batteries. *Energy Environ. Sci.,* **6**, 2414-2423 (2013).

87. Hiralal P., Imaizumi S., Unalan H. E., Matsumoto H., Minagawa M., Rouvala M.*, et al.* Nanomaterial-Enhanced All-Solid Flexible Zinc−Carbon Batteries. *ACS nano,* **4**, 2730-2734 (2010).

88. Koo M., Park K.-I., Lee S. H., Suh M., Jeon D. Y., Choi J. W.*, et al.* Bendable Inorganic Thin-Film Battery for Fully Flexible Electronic Systems. *Nano Lett.,* **12**, 4810-4816 (2012).

89. Kwon Y. H., Woo S.-W., Jung H.-R., Yu H. K., Kim K., Oh B. H.*, et al.* Cable-Type Flexible Lithium Ion Battery Based on Hollow Multi-Helix Electrodes. *Adv. Mater.,* **24**, 5192-5197 (2012).

90. Zhou G., Li F., Cheng H.-M. Progress in flexible lithium batteries and future prospects. *Energy Environ. Sci.,* **7**, 1307-1338 (2014).

91. Ren J., Bai W., Guan G., Zhang Y., Peng H. Flexible and Weaveable Capacitor Wire Based on a Carbon Nanocomposite Fiber. *Adv. Mater.,* **25**, 5965-5970 (2013).

92. Sun H., You X., Yang Z., Deng J., Peng H. Winding ultrathin, transparent, and electrically conductive carbon nanotube sheets into high-performance fiber-shaped dye-sensitized solar cells. *J. Mater. Chem. A,* **1**, 12422-12425 (2013).

93. Yang Z., Deng J., Chen X., Ren J., Peng H. A Highly Stretchable, Fiber-Shaped Supercapacitor. *Angew. Chem. Int. Ed.,* **52**, 13453-13457 (2013).

94. Sun H., Li H., You X., Yang Z., Deng J., Qiu L.*, et al.* Quasi-solid-state, coaxial, fiber-shaped dye-sensitized solar cells. *J. Mater. Chem. A,* **2**, 345-349 (2014).

95. Zhang Z., Yang Z., Wu Z., Guan G., Pan S., Zhang Y.*, et al.* Weaving Efficient Polymer Solar Cell Wires into Flexible Power Textiles. *Adv. Energy Mater.,* **4**, 1301750 (2014).

96. Sun H., You X., Deng J., Chen X., Yang Z., Chen P.*, et al.* A Twisted Wire-Shaped Dual-Function Energy Device for Photoelectric Conversion and Electrochemical Storage. *Angew. Chem. Int. Ed.,* **53**, 6664-6668 (2014).

97. Weng W., Sun Q., Zhang Y., Lin H., Ren J., Lu X.*, et al.* Winding Aligned Carbon Nanotube Composite Yarns into Coaxial Fiber Full Batteries with High Performances. *Nano Lett.,* **14**, 3432-3438 (2014).

98. Read J., Mutolo K., Ervin M., Behl W., Wolfenstine J., Driedger A.*, et al.* Oxygen Transport Properties of Organic Electrolytes and Performance of Lithium/Oxygen Battery. *J. Electrochem. Soc.,* **150**, A1351-A1356 (2003).

99. Lewandowski A., Skorupska K., Malinska J. Novel poly(vinyl alcohol)–KOH–H_2O alkaline polymer electrolyte. *Solid State Ionics,* **133**, 265-271 (2000).

100. Mohamad A. A., Mohamed N. S., Alias Y., Arof A. K. Studies of alkaline solid polymer electrolyte and mechanically alloyed polycrystalline Mg_2Ni for use in nickel metal hydride batteries. *J. Alloys Compd.,* **337**, 208-213 (2002).

101. Yang C.-C. Polymer Ni–MH battery based on PEO–PVA–KOH polymer electrolyte. *J. Power Sources,* **109**, 22-31 (2002).

102. Vassal N., Salmon E., Fauvarque J. F. Electrochemical properties of an alkaline solid polymer electrolyte based on P(ECH-co-EO). *Electrochim. Acta,* **45**, 1527-1532 (2000).

103. Fauvarque J. F., Guinot S., Bouzir N., Salmon E., Penneau J. F. Alkaline poly(ethylene oxide) solid polymer electrolytes. Application to nickel secondary batteries. *Electrochim. Acta,* **40**, 2449-2453 (1995).

104. Hatta F. F., Yahya M. Z. A., Ali A. M. M., Subban R. H. Y., Harun M. K., Mohamad A. A. Electrical conductivity studies on PVA/PVP-KOH alkaline solid polymer blend electrolyte. *Ionics,* **11**, 418-422 (2005).

105. Guo S., Zhang S., Sun S. Tuning nanoparticle catalysis for the oxygen reduction reaction. *Angew. Chem. Int. Ed.,* **52**, 8526-44 (2013).

106. Xu J.-J., Wang Z.-L., Xu D., Zhang L.-L., Zhang X.-B. Tailoring deposition and morphology of discharge products towards high-rate and long-life lithium-oxygen batteries. *Nat. Commun.,* **4**, 2438 (2013).

107. Xu J.-J., Xu D., Wang Z.-L., Wang H.-G., Zhang L.-L., Zhang X.-B. Synthesis of Perovskite-Based Porous $La_{0.75}Sr_{0.25}MnO_3$ Nanotubes as a Highly Efficient Electrocatalyst for Rechargeable Lithium–Oxygen Batteries. *Angew. Chem. Int. Ed.,* **52**, 3887-3890 (2013).

108. Wang Z.-L., Xu D., Xu J.-J., Zhang L.-L., Zhang X.-B. Graphene Oxide Gel-Derived, Free-Standing, Hierarchically Porous Carbon for High-Capacity and High-Rate Rechargeable Li-O_2 Batteries. *Adv. Funct. Mater.,* **22**, 3699-3705 (2012).

109. Choudhury N. A., Sampath S., Shukla A. K. Gelatin Hydrogel Electrolytes and Their Application to Electrochemical Supercapacitors. *J. Electrochem. Soc.,* **155**, A74-A81 (2008).

110. Vieira D. F., Avellaneda C. O., Pawlicka A. Conductivity study of a gelatin-based polymer electrolyte. *Electrochim. Acta,* **53**, 1404-1408 (2007).

111. Nam G., Park J., Kim S. T., Shin D.-b., Park N., Kim Y.*, et al.* Metal-Free Ketjenblack Incorporated Nitrogen-Doped Carbon Sheets Derived from Gelatin as Oxygen Reduction Catalysts. *Nano Lett.,* **14**, 1870-1876 (2014).

112. Harrington W. F., Rao N. V. Collagen structure in solution. I. Kinetics of helix regeneration in single-chain gelatins. *Biochem.,* **9**, 3714-3724 (1970).

113. Bello J., Bello H. R., Vinograd J. R. The mechanism of gelation of gelatin the influence of pH, concentration, time and dilute electrolyte on the gelation of gelatin and modified gelatins. *Biochim. Biophys. Acta,* **57**, 214-221 (1962).

114. Hakimi O., Knight D. P., Vollrath F., Vadgama P. Spider and mulberry silkworm silks as compatible biomaterials. *Composites Part B,* **38**, 324-337 (2007).

115. Lee J.-S., Park G. S., Kim S. T., Liu M., Cho J. A Highly Efficient Electrocatalyst for the Oxygen Reduction Reaction: N-Doped Ketjenblack Incorporated into Fe/Fe_3C-Functionalized Melamine Foam. *Angew. Chem. Int. Ed.,* **52**, 1026-1030 (2013).

116. Damjanovic A., Sepa D. B., Vojnovic M. V. New evidence supports the proposed mechanism for O_2 reduction at oxide free platinum electrodes. *Electrochim. Acta,* **24**, 887-889 (1979).

117. Bruce P. G., Freunberger S. A., Hardwick L. J., Tarascon J.-M. Li-O_2 and Li-S batteries with high

energy storage. *Nat. Mater.,* **11**, 19-29 (2012).

118. Pei P., Wang K., Ma Z. Technologies for extending zinc–air battery's cyclelife: A review. *Appl. Energy,* **128**, 315-324 (2014).

119. Park J., Park M., Nam G., Lee J. s., Cho J. All-Solid-State Cable-Type Flexible Zinc–Air Battery. *Adv. Mater.*, 1396-1401 (2014).

120. Wu G., More K. L., Johnston C. M., Zelenay P. High-Performance Electrocatalysts for Oxygen Reduction Derived from Polyaniline, Iron, and Cobalt. *Science,* **332**, 443-447 (2011).

121. Li Y., Gong M., Liang Y., Feng J., Kim J.-E., Wang H*., et al.* Advanced zinc-air batteries based on high-performance hybrid electrocatalysts. *Nat. Commun.,* **4**, 1805 (2013).

122. Bashyam R., Zelenay P. A class of non-precious metal composite catalysts for fuel cells. *Nature,* **443**, 63-66 (2006).

123. Cao R., Thapa R., Kim H., Xu X., Gyu Kim M., Li Q*., et al.* Promotion of oxygen reduction by a bio-inspired tethered iron phthalocyanine carbon nanotube-based catalyst. *Nat. Commun.,* **4**, 2076 (2013).

124. Meng F., Zhong H., Bao D., Yan J., Zhang X. In Situ Coupling of Strung Co_4N and Intertwined N–C Fibers toward Free-Standing Bifunctional Cathode for Robust, Efficient, and Flexible Zn–Air Batteries. *J. Am. Chem. Soc.,* **138**, 10226-10231 (2016).

125. Nam G., Park J., Choi M., Oh P., Park S., Kim M. G*., et al.* Carbon-Coated Core–Shell Fe–Cu Nanoparticles as Highly Active and Durable Electrocatalysts for a Zn–Air Battery. *ACS nano*, 6493-6501 (2015).

126. Yang S., Feng X., Wang X., Müllen K. Graphene-Based Carbon Nitride Nanosheets as Efficient Metal-Free Electrocatalysts for Oxygen Reduction Reactions. *Angew. Chem. Int. Ed.,* **50**, 5339-5343 (2011).

127. Zheng Y., Jiao Y., Chen J., Liu J., Liang J., Du A*., et al.* Nanoporous Graphitic-C_3N_4@Carbon Metal-Free Electrocatalysts for Highly Efficient Oxygen Reduction. *J. Am. Chem. Soc.,* **133**, 20116-20119 (2011).

128. Liang Y., Li Y., Wang H., Dai H. Strongly Coupled Inorganic/Nanocarbon Hybrid Materials for Advanced Electrocatalysis. *J. Am. Chem. Soc.,* **135**, 2013-2036 (2013).

129. Lee D. U., Choi J.-Y., Feng K., Park H. W., Chen Z. Advanced Extremely Durable 3D Bifunctional Air Electrodes for Rechargeable Zinc-Air Batteries. *Adv. Energy Mater.,* **4**, 1301389 (2014).

130. Chen D., Chen C., Baiyee Z. M., Shao Z., Ciucci F. Nonstoichiometric Oxides as Low-Cost and Highly-Efficient Oxygen Reduction/Evolution Catalysts for Low-Temperature Electrochemical Devices. *Chem. Rev.,* **115**, 9869-921 (2015).

131. Jung J.-I., Jeong H. Y., Kim M. G., Nam G., Park J., Cho J. Fabrication of $Ba_{0.5}Sr_{0.5}Co_{0.8}Fe_{0.2}O_{3-\delta}$ Catalysts with Enhanced Electrochemical Performance by Removing an Inherent Heterogeneous Surface Film Layer. *Adv. Mater.,* **27**, 266-271 (2015).

132. Zhang J., Zhao Z., Xia Z., Dai L. A metal-free bifunctional electrocatalyst for oxygen reduction and oxygen evolution reactions. *Nat. Nanotechnol.,* **10**, 444-452 (2015).

133. Xia B. Y., Yan Y., Li N., Wu H. B., Lou X. W., Wang X. A metal–organic framework-derived bifunctional oxygen electrocatalyst. *Nat. Energy,* **1**, 15006 (2016).

134. Maiyalagan T., Jarvis K. A., Therese S., Ferreira P. J., Manthiram A. Spinel-type lithium cobalt oxide as a bifunctional electrocatalyst for the oxygen evolution and oxygen reduction reactions. *Nat. Commun.,* **5**, 3949 (2014).

135. Liu X., Park M., Kim M. G., Gupta S., Wu G., Cho J. Integrating NiCo Alloys with Their Oxides as Efficient Bifunctional Cathode Catalysts for Rechargeable Zinc–Air Batteries. *Angew. Chem. Int. Ed.,* **54**, 9654-9658 (2015).

136. Xu J.-J., Wang Z.-L., Xu D., Meng F.-Z., Zhang X.-B. 3D ordered macroporous $LaFeO_3$ as efficient electrocatalyst for Li-O_2 batteries with enhanced rate capability and cyclic performance. *Energy Environ. Sci.,* **7**, 2213-2219 (2014).

137. Jiang S. P., Love J. G. Origin of the initial polarization behavior of Sr-doped $LaMnO_3$ for O_2 reduction in solid oxide fuel cells. *Solid State Ionics,* **138**, 183-190 (2001).

138. Horowitz H. S., Longo J. M., Horowitz H. H. Oxygen Electrocatalysis on Some Oxide Pyrochlores.

J. Electrochem. Soc., **130**, 1851-1859 (1983).

139. Eun-Ok Chi Y.-U. K., Sun-il Mho. Oxygen Evolution Reaction at Electrode of Single Phase Ruthenium Oxides with Perovskite and Pyrochlore Structures. *Bull. Korean Chem. Soc.,* **18**, 972-976 (1997).

140. Prakash J., Tryk D. A., Yeager E. B. Kinetic Investigations of Oxygen Reduction and Evolution Reactions on Lead Ruthenate Catalysts. *J. Electrochem. Soc.,* **146**, 4145-4151 (1999).

141. Parrondo J., George M., Capuano C., Ayers K. E., Ramani V. Pyrochlore electrocatalysts for efficient alkaline water electrolysis. *J. Mater. Chem. A,* **3**, 10819-10828 (2015).

142. Lee K. T., Lee B. W., Camaratta M. A., Wachsman E. D. Enhanced oxygen reduction reaction with nano-scale pyrochlore bismuth ruthenate via cost-effective wet-chemical synthesis. *RSC Adv.,* **3**, 19866-19871 (2013).

143. Holewinski A., Linic S. Elementary Mechanisms in Electrocatalysis: Revisiting the ORR Tafel Slope. *J. Electrochem. Soc.,* **159**, H864-H870 (2012).

144. Choy J.-H., Hwang S.-H., Demazeau G., Jung D.-Y. X-Ray Diffraction and X-Ray Absorption Spectrocopic Analyses for the Ruthenium Perovskites. *J. Phys. IV,* **7**, 763-764 (1997).

145. Kim J. S., Kim B. H., Kim D. C., Lee H. J., Kim M. G., Maignan A.*, et al.* Valence State of Ru at the Mn Sites in $Pr_{0.5}Sr_{0.5}MnO_3$: Thermoelectric Power and X-Ray Absorption Near-Edge Structure Spectroscopy. *J. Supercond.,* **17**, 183-186 (2004).

146. Park J., Kim K. H., Noh H.-J., Oh S. J., Park J. H., Lin H.-J.*, et al.* Photoemission and x-ray absorption spectroscopy studies on cubic pyrochlore ruthenates $Bi_{2-x}Y_xRu_2O_7$. *Phys. Rev. B,* **69**, 165120 (2004).

147. Braun A., Erat S., Ariffin A. K., Manzke R., Wadati H., Graule T.*, et al.* High temperature oxygen near edge x-ray absorption fine structure valence band spectra and conductivity of $LaFe_{3/4}Ni_{1/4}O_3$ from 300 to 773 K. *Appl. Phys. Lett.,* **99**, 202112 (2011).

148. Lee J. S., Lee Y. S., Noh T. W., Char K., Park J., Oh S. J.*, et al.* Optical investigation of the electronic structures of $Y_2Ru_2O_7$, $CaRuO_3$, $SrRuO_3$, and $Bi_2Ru_2O_7$. *Phys. Rev. B,* **64**, 245107 (2001).

149. Egdell R. G., Goodenough J. B., Hamnett A., Naish C. C. Electrochemistry of ruthenates. Part 1.-Oxygen reduction on pyrochlore ruthenates. *J. Chem. Soc., Faraday,* **79**, 893-912 (1983).

150. Tachibana M., Kohama Y., Shimoyama T., Harada A., Taniyama T., Itoh M.*, et al.* Electronic properties of the metallic pyrochlore ruthenates $Pb_2Ru_2O_{6.5}$ and $Bi_2Ru_2O_7$. *Phys. Rev. B,* **73**, 193107 (2006).

151. Suntivich J., Hong W. T., Lee Y.-L., Rondinelli J. M., Yang W., Goodenough J. B.*, et al.* Estimating Hybridization of Transition Metal and Oxygen States in Perovskites from O K-edge X-ray Absorption Spectroscopy. *J. Phys. Chem. C,* **118**, 1856-1863 (2014).

152. Lee J.-S., Kim S. T., Cao R., Choi N.-S., Liu M., Lee K. T.*, et al.* Metal-Air Batteries with High Energy Density: Li-Air versus Zn-Air. *Adv. Energy Mater.,* **1**, 34-50 (2011).

153. Pei P., Ma Z., Wang K., Wang X., Song M., Xu H. High performance zinc air fuel cell stack. *J. Power Sources,* **249**, 13-20 (2014).

154. Lu Y.-C., Xu Z., Gasteiger H. A., Chen S., Hamad-Schifferli K., Shao-Horn Y. Platinum−Gold Nanoparticles: A Highly Active Bifunctional Electrocatalyst for Rechargeable Lithium−Air Batteries. *J. Am. Chem. Soc.,* **132**, 12170-12171 (2010).

155. Zhang Z., Wang X., Cui G., Zhang A., Zhou X., Xu H.*, et al.* $NiCo_2S_4$ sub-micron spheres: an efficient non-precious metal bifunctional electrocatalyst. *Nanoscale,* **6**, 3540-3544 (2014).

156. Park J., Risch M., Nam G., Park M., Shin T. J., Park S.*, et al.* Single crystalline pyrochlore nanoparticles with metallic conduction as efficient bi-functional oxygen electrocatalysts for Zn-air batteries. *Energy Environ. Sci.,* **10**, 129-136 (2017).

157. Shannon R. Revised effective ionic radii and systematic studies of interatomic distances in halides and chalcogenides. *Acta Crystallogr., Sect. A: Found. Crystallogr.,* **32**, 751-767 (1976).

158. Abate C., Duncan K., Esposito V., Traversa E., Wachsman E. D. Synthesis and Characterization of $Y_2Ru_2O_7$ and $Y_{2-x}Pr_xRu_2O_7$ for Cathode Application in Intermediate Temperature Solid Oxide Fuel Cells. *ECS Trans.,* **1**, 255-261 (2006).

159. Kanno R., Takeda Y., Yamamoto T., Kawamoto Y., Yamamoto O. Crystal Structure and Electrical

Properties of the Pyrochlore Ruthenate $Bi_{2-x}Y_xRu_2O_7$. *J. Solid State Chem.,* **102**, 106-114 (1993).

160. Seo B., Sa Y. J., Woo J., Kwon K., Park J., Shin T. J., *et al.* Size-Dependent Activity Trends Combined with in Situ X-ray Absorption Spectroscopy Reveal Insights into Cobalt Oxide/Carbon Nanotube-Catalyzed Bifunctional Oxygen Electrocatalysis. *ACS Catal.,* **6**, 4347-4355 (2016).

161. Sa Y. J., Seo D.-J., Woo J., Lim J. T., Cheon J. Y., Yang S. Y., *et al.* A General Approach to Preferential Formation of Active Fe–N_x Sites in Fe–N/C Electrocatalysts for Efficient Oxygen Reduction Reaction. *J. Am. Chem. Soc.,* **138**, 15046-15056 (2016).

162. Gorlin Y., Lassalle-Kaiser B., Benck J. D., Gul S., Webb S. M., Yachandra V. K., *et al.* In Situ X-ray Absorption Spectroscopy Investigation of a Bifunctional Manganese Oxide Catalyst with High Activity for Electrochemical Water Oxidation and Oxygen Reduction. *J. Am. Chem. Soc.,* **135**, 8525-8534 (2013).

163. Wang X., Li W., Chen Z., Waje M., Yan Y. Durability investigation of carbon nanotube as catalyst support for proton exchange membrane fuel cell. *J. Power Sources,* **158**, 154-159 (2006).

164. Wang C. M., Cargill G. S., Chan H. M., Harmer M. P. X-ray Absorption Near-Edge Structure of Grain-Boundary-Segregated Y and Zr in Creep-Resistant Alumina. *J. Am. Ceram. Soc.,* **85**, 2492-2498 (2002).

165. Koningsberger D. C., Prins R. X-ray absorption: principles, applications, techniques of EXAFS, SEXAFS, and XANES (John Wiley and Sons,New York, NY; None, 1988).

166. Chen S.-W., Fu S.-W., Pao C.-W., Lee J.-M., Chen S.-A., Haw S.-C., *et al.* Low temperature structural anomalies arising from competing exchange interactions in pyrochlore $Nd_2Ru_2O_7$ probed by XRD and EXAFS. *Phys. Chem. Chem. Phys.,* **17**, 23667-23673 (2015).

167. Stamenkovic V. R., Fowler B., Mun B. S., Wang G., Ross P. N., Lucas C. A., *et al.* Improved Oxygen Reduction Activity on $Pt_3Ni(111)$ via Increased Surface Site Availability. *Science,* **315**, 493-497 (2007).

168. Yano J., Yachandra V. K. X-ray absorption spectroscopy. *Photosynth. Res.,* **102**, 241 (2009).

Acknowledgements

지난 2009년 3월, 설레는 마음을 안고 UNIST 1기로 입학하여 대학생활을 시작한지가 엊그제 같은데, 어느새 학부 및 대학원 과정을 마무리하고 박사학위를 받게 되니 감회가 새롭습니다. 먼저, 학부생이었던 제가 이차전지에 관한 연구를 하고자 찾아 뵈었을 때, 흔쾌히 받아주신 조재필 교수님께 깊은 감사의 말씀을 드립니다. 항상 저의 위치에서 무엇이 중요한지, 어떠한 것에 집중을 해야 하는지 말씀하시며 스스로 연구할 수 있도록 지도해주신 덕분에 많은 것들을 배울 수 있었습니다. 아직 부족한 점이 많지만 학위과정동안 해주신 말씀들을 바탕으로 연구에 더욱 매진하겠습니다. 또한 박사학위 논문 심사를 맡아주신 김영식 교수님, 홍성유 교수님, 강석주 교수님, 그리고 이현욱 교수님께도 감사의 말씀을 전합니다. 교수님들께서 해주신 조언들 덕분에 앞으로 저의 연구방향을 설정하는데 큰 도움이 되었습니다.

다음으로 연구실 생활을 함께한 랩원들께 감사인사를 드립니다. 먼저, 처음 아연공기전지를 연구할 때, 많은 도움을 주신 이장수 형님과 Cao 박사님께 감사드립니다. 박사님들 덕분에 처음 접한 연구분야에 잘 적응할 수 있었습니다. 그리고 직속 선배님이 아니었음에도 불구하고 진행중인 연구에 대해 함께 토의해주시고 챙겨주신 박민준 형님께 대단히 감사드립니다. 형님께서 주신 가르침 덕분에 여러 성과를 낼 수 있었습니다. 또한 대학원 생활 중 가장 많은 시간을 함께하고 힘이 되어준 후배이자 친구인 류재찬에게 고맙다는 말을 전합니다. 이 밖의 많은 연구실 선배님들, 동기님들, 그리고 후배님들께도 감사드립니다. 함께 대학원 생활을 할 수 있어서 영광이었습니다.

마지막으로 저를 항상 응원해주시고 큰 힘이 되어주시는 사랑하는 부모님께 감사한 마음을 전합니다. 어릴 때부터 박사학위를 받기까지 오랜 기간을 공부해오면서 항상 저를 믿어주시고 인생에 대한 조언을 아낌없이 해주셔서 대단히 감사합니다. 앞으로 부모님께 자랑스러운 아들이 되도록 노력하겠습니다. 사랑합니다.